Indian Institute of Technology Guwahati

Doctoral Thesis

Development of grating array based zonal wavefront sensor for in-situ surface profiling during the growth of the thin film in a deposition system

Nagendra Kumar

Roll No: 156121024

Thesis submitted in partial fulfilment of the requirements for the degree of Doctor of Philosophy of the Indian Institute of Technology Guwahati.

Supervisor: Prof. Bosanta R. Boruah
Prof. Alika Khare

Department of Physics
Indian Institute of Technology Guwahati
Guwahati (Assam), India, Pin- 781039

November 2021

Dedicated to my parents . . .

Declaration

Nagendra Kumar
Roll No: 156121024
Department of Physics
Indian Institute of Technology Guwahati
Guwahati (Assam), India, Pin- 781039
Email: nagendra.2015@iitg.ac.in

I hereby declare that the results embodied in this thesis is the result of theory and experiment carried out by me at the Department of Physics, Indian Institute of Technology Guwahati, Guwahati, India, under the supervision of **Prof. Bosanta R. Boruah** and **Prof. Alika Khare**. This thesis has not been submitted to any university/ institute or elsewhere for the award of any degree, diploma or associateship.

Nagendra Kumar
November 2021

भारतीय प्रौद्योगिकी संस्थान गुवाहाटी
Indian Institute of Technology Guwahati

Certificate

Prof. Bosanta R. Boruah **Prof. Alika Khare**
Department of Physics
Indian Institute of Technology Guwahati
Guwahati (Assam), India, Pin- 781039
Emails: brboruah@iitg.ac.in alika@iitg.ac.in

This is to certify that the work contained in the thesis entitled **‘Development of grating array based zonal wavefront sensor for in-situ surface profiling during the growth of the thin film in a deposition system ’** by **Nagendra Kumar** (Roll No. 156121024), a student of Department of Physics, Indian Institute of Technology Guwahati, for the award of degree of Doctor of Philosophy, has been carried out under our supervision.

The present thesis or any part thereof has not been submitted elsewhere for award of any other degree, diploma or associateship.

Prof. Bosanta R. Boruah Prof. Alika Khare
November 2021

Acknowledgements

First and foremost, I'm deeply indebted to my thesis supervisors Prof. Bosanta Ranjan Boruah and Prof. Alika Khare for providing me a painstaking guidance, endless discussion and discernment comments throughout my entire journey of PhD work. During my PhD journey, they contributed to a rewarding experience by providing me intellectual freedom in my work, supporting my attendance at various conferences, and engaging me in new ideas in all my endeavours. Most importantly, the exemplar advice of Prof. Boruah helps me a lot even after several failure attempts of theoretical coding and performing the experiments. I would like to extend my sincere thanks to my doctoral committee Prof. Pratima Agarwal, Dr. Gagan Kumar, and Prof. Shrikrishna N. Joshi for evaluating my research work and providing their valuable suggestions. I am also grateful to the former and present HoDs of Physics, Prof A. Perumal, Prof. Subhradip Ghosh, and Prof. P Poulose for providing me to access the resources, and instruments of the department. I also wish to thank to all the staff members of the Department of Physics for their support in all possible way. I would like to thanks Leoni Choudhury, Himanku Dutta, and Ambarish Biswas and for their cooperation in the paper work. I would like to thank all the people who contributed directly or indirectly to my thesis work. Few results described in this thesis was accomplished with the help and support of fellow labmates, and it had great pleasure of working in such a great environment. I would like to extend my sincere thanks to my past and present labmates Dr. Biswajit Pathak, Dr. Santanu Konwar, Dr. Ranjan Kalita, Dr. SS Goutam Buddha, Mr Karuna S Malik, Mr Akanshu Chauhan, Mr Nedup Sherpa, Mr Anupam Bhardwaj, Mr Pranjal Choudhury, Ms Shilpa Singh for their help to carried out the experiments, simulation and quality time that we have spent together. I would also like thank to Laser and Photonics lab members Dr. Partha P Dey, Dr. Gyan P Bharti, Dr. Rahul Kesaewani, Dr Eshita Mal, Dr. Gobinda Pradhan, Mrs Sasmita Behara, Mr Sumit Goswami, Mr Soodarshan L Hegde, Ms Pooja Kumari, Lwithwsa Swargiary, Ankan Pramanik for their help in operating the Pulsed laser deposition system. I would like to thank Mr Sumit Goswami for his help in pulsed laser deposition since without his efforts my job would have undoubtedly been more difficult. I cannot begin to express my thanks to SPIE IIT Guwahati student chapter and its members who kept me involved in organizing the various event in various schools, colleges, universities. I also wish to thank to OSAF and SPIE for providing the travel fund to attend the international conferences and school. It would be remiss if I did not acknowledge the financial support from the Ministry of Human Resource and Development (MHRD), Government of India during my PhD tenure as a PhD fellowship.

Many thanks to all my close friends Sunil Mohan, Ram Manohar, Manvendra, Pratap, Joy, Pulak, Sheel, Anurag at IIT Guwahati for the wonderful times, providing me cheers on, and also celebrated each accomplishment.

A special thanks to my mummy, papa Indravati and Doodh Nath for the continuous love, every possible support they have given me throughout my student life. Words cannot express how grateful I am to my brother Dr. Virendra Kumar for supporting me for everything, encouraging me and especially I can't thank him enough for taking care of my study expenditure from my school days. Finally, I would like to thank my elders Ravindra and Jitendra for their love and moral support.

Abstract

Thin films are important in a number of scientific and industrial applications. To ensure good quality thin films, it is important to monitor the growth of the film during deposition so as to take care of corrective measures in the case if the quality of the film deviates from that of the required one, apart from monitoring the surface profile and the thickness of the film. Most of the available in-situ techniques till date require the prior information on the properties of the thin film and the substrate on which it is deposited. In the present thesis, a novel grating array based wavefront sensing (GAWS) scheme is proposed and demonstrated experimentally which can be used to measure both the thickness and surface profiles of the thin films simultaneously as a function of time during the growth process of the film. This scheme does not require any prior information on the properties of the substrate and target material, provided both the substrate and film are reflecting. We use a grating array based wavefront sensor (GAWS) assembly, realised with a ferroelectric liquid crystal spatial light modulator, integrated to a pulsed laser deposition system in order to measure the thickness and surface profiles, simultaneously, of Cu thin films on a well-polished stainless-steel substrate, during deposition as a function of time. An appropriate algorithm is developed to obtain the thickness and surface profiles from the measured phase profiles of the GAWS. The post deposited thickness profile obtained from the GAWS is found to be in reasonable agreement with that of a commercial profilometer. Further, two novel schemes to enhance the sensitivity and dynamic range of the wavefront sensor are also proposed and demonstrated experimentally. We verify the accuracy of the scheme to enhance sensitivity by measuring known amount of holographically introduced aberrations. The scheme to enhance the dynamic range is tested on the transmitted wavefronts through convex and concave lenses. The radii of curvature of the transmitted spherical wavefronts measured by the proposed zonal wavefront sensing scheme and the corresponding estimated focal lengths of the lenses show agreement with the commercial data provided by the lens manufacturer. The detection path of the integrated system can be easily rearranged to activate the high sensitivity as well as the high dynamic range mode of the scheme to carry out in-situ measurements. With enhanced sensitivity, the integrated system can be implemented to monitor highly uniform thin films in-situ during deposition while with enhanced dynamic range it can assess the deposition of periodic and non-periodic curved as well as plane structures.

Table of contents


भारतीय प्रौद्योगिकी संस्थान गुवाहाटी
Indian Institute of Technology Guwahati

List of figures

List of tables

Acronyms and Abbreviation

Greek Symbols

π	$\simeq 3.14\ldots$
i	Unit Imaginary Number ($\sqrt{-1}$)
λ	Wavelength
ν	Frequency
k	Propagation constant
θ	Angle

Acronyms / Abbreviations

BS	Beam Splitter
CGH	Computer Generated Holography
CMOS	Complementary Metal Oxide Semiconductor
C_s	Calibration Constant
CVD	Chemical Vapor Deposition
DPSS	Diode-Pumped Solid State
Est.	Estimated
FLC	Ferroelectric Liquid Crystal
FLCSLM	Ferroelectric Liquid Crystal Spatial Light Modulator

FPS	Frames Per Second
FWHM	Full Width at Half Maximum
GAWS	Grating Array Based Zonal Wavefront Sensor
GS	Galvo Scan
GSM	Galvo Scan Mirror
HS	High Sensitivity
HWP	Half waveplate
ID	Iris Diaphragm
IR	Infrared
LC	Liquid Crystal
LCSLM	Liquid Crystal Spatial Light Modulator
LIR	Laser Reflectance Interferometry
LS	Low Sensitivity
NDF	Neutral Density Filter
NLCSLM	Nematic Liquid Crystal Spatial light modulator
PH	Pin Hole
PBS	Polarizing Beam Splitter
PC	Personal Computer
PLD	Pulsed Laser Deposition
PSF	Point Spread Function
PtV	Peak to valley
PVD	Physical Vapour Deposition
QCM	Quarts Crystal Microbalance
RMS	Root Mean Square

RMSE	Root Mean Square Error
SHWS	Shack Hartmann Wavefront Sensor
SEZWS	Sensitivity enhanced zonal wavefront sensor
SLM	Spatial Light Modulator
SXGA	Super Extended Graphics Array
WS	Wavefront Sensor


भारतीय प्रौद्योगिकी संस्थान गुवाहाटी
Indian Institute of Technology Guwahati

CHAPTER 1

General Introduction

1.1 Introduction

Many technological advancements of recent times are heavily backed by the appropriate thin films. Development in thin film technologies have played a significant role towards advancement in emerging areas of research in physical [1] and chemical sciences [2] apart from miniaturization of devices and other technological developments.

Thin film coatings have been used over a wide range of applications, for example in anti-reflective coatings to reduce the reflection of optical surfaces [3], in scratch-resistant coatings on eyeglass lenses as well as other applications [4, 5], in IR-reflective coatings to favorably transmit IR wavelengths [6], etc. Thin film technology is useful in other commercially important areas such as semiconductor industry to miniaturize the semiconductor-based devices [7], optoelectronics, microchip-based thin film batteries and capacitors[8] [9], data storage [10, 11], display applications that uses LCDs and CMOS sensors [12]. Thin film technology is also implemented in the fabrication of solar cells as well as to enhance the photo-thermal conversion efficiency [13, 14] for the clean energy.

In order to obtain a desired quality of thin film, selection of thin film deposition technique is very important. Based on the working principle, thin film deposition is broadly classified into two groups: physical vapour deposition (PVD) [13] and chemical deposition [2]. PVD is a vaporization based coating process in which material is released from a solid target source and gradually deposited onto a substrate through a electrochemical or thermodynamic process. [15]. While chemical deposition methods depend on the specific chemical reaction. There are various chemical methods to deposit thin films, for example spray pyrolysis technique [16], chemical vapour deposition (CVD) [17], sol-gel technique [18], screen painting [19] and many more [20].

The physical vapour deposition technique is divided into two subclasses, (a) thermal evaporation technique [15] and (b) sputtering technique. Thermal evaporation is a vapour based deposition technique in which source material is evaporated by heating the target material under vacuum. Examples of thermal evaporation techniques are electron beam evaporation [21], molecular beam epitaxy [22], pulsed laser deposition [23] etc. While sputtering is a plasma-based technique that creates a vapour from the source target through bombardment with accelerated gaseous ions [24, 25]. Direct current sputtering [26] , radio frequency sputtering [27] are some examples of the sputtering thin film deposition technique.

For any specific device application, apart from the material of the thin film and substrate on which it is deposited, its thickness and surface profile are also very important for the performance of the device. The growth process of the thin film during deposition eventually decides these properties of the final thin film. Therefore to ensure requisite quality of the film, it is desirable to implement an in-situ monitoring techniques for measurement of thickness and surface profile of the thin film during the deposition process. Such an in-situ technique for online monitoring of the thin film surface during deposition shouldn’t interfere with the deposition process. The online monitoring technique helps in unveiling the deposition dynamics and nucleation growth process of the thin film. It also plays a key role in identifying the faults in the film during growth process. Further a feedback control can be augmented with the thin film deposition system so as to control the growth process.

There have been several intrusive and non-intrusive in-situ surface profile and thickness measurement techniques. Here intrusive measurement techniques refer to those techniques where sensor is placed or mounted inside the deposition chamber, whereas non-intrusive techniques refer to those where sensors are placed outside the deposition chamber.

Quartz crystal microbalance (QCM) is an intrusive and ultrasensitive weighing device, used to determine the thickness of the material in real time during the deposition [28]. QCM has been conventionally implemented over a range of deposition systems. It is a piezoelectric based device and responds to the applied voltage linked to its natural oscillation frequency. The resonant frequency decreases whenever some material is deposited onto the quartz crystal. The resultant shift in the frequency is directly related to additional mass and hence the thickness of the thin film. However QCM is not a direct in-situ measurement technique as the deposition takes place onto the quartz crystal only and not on the actual substrate. Moreover, the crystal stops oscillating if a large amount of mass is deposited onto the quartz crystal. Additionally, quartz crystal is very sensitive to the temperature and stress change and it may not be able to provide the correct thickness as frequency also shifts due to temperature fluctuations [29] [30].

To overcome the limitations of QCM, another in-situ measurement scheme can be used that utilizes the ultrasonic lamb waves in silicon wafer [31]. This in-situ thickness measurement technique, measures the velocity of ultrasonic lamb waves which are propagating through the silicon wafer. The change in the velocity of ultrasonic lamb waves depends on the growth of the thin film on the wafer surface. However even this scheme is also temperature sensitive and requires the prior knowledge of properties of the sample under consideration.

Ellipsometer is another powerful and an in-situ technique to measure the thickness of the thin films [32, 33]. In this technique a light beam from a white light source is incident on the sample and reflected light is recorded as a function of angle of incidence and the wavelength for both p as well as s polarization. The change in the state of the polarization of the incident beam as well as reflected and transmitted intensity from the sample are very sensitive to the thickness and optical properties of the thin film as well as that of the substrate. Knowing the optical properties of the substrate and refractive index of the thin film, the thickness of the thin film can be assessed from the change in the polarization. Thus, ellipsometer for in-situ measurement seeks prior information of the properties of the material substrate and other parameters. In this technique, data analysis also play a vital role along with the measurement process. It require a proper physical model to calculate the thickness and other optical properties. Further, it is a point measurement technique and it cannot provide the entire surface information in a single measurement.

In order to measure the thickness of the thin film in real time, laser reflectance interferometry (LRI) is also viewed as a very useful technique [34]. It is a non-contact in-situ optical thickness measurement technique [35]. LRI records the intensity of a laser beam reflected from the substrate surface on which film is to be deposited and then from the deposited thin film. In this technique, an interference pattern is observed which is formed due to the superposition of the beams reflected from the top and the bottom surface of the film . The specular reflectivity oscillates due to the formation of the interference patterns with the increase in the thickness of the film during the deposition and thus providing the information on film thickness and hence growth rate [36, 37]. However, it requires presumption of the values on film refractive index in order to measure the thickness of the thin film. If its actual value differs from the assumed one, a significant error may occur in the measured value of the thickness.

Yet another in-situ thickness measurement technique is using the optical fibre-based sensor [38, 39]. A multimode optical fibre based sensor utilizes the surface plasmon resonance phenomenon to measure the thickness of the thin film. In this technique, cladding of the optical fibre is removed and deposition takes place on the uncladded region. As the deposition starts on the uncladded region of the fibre, the propagation of laser passing through the fibre, experiences enhanced absorption due to surface plasmon resonance (SPR). With the growth of the film on the fibre in the uncladded region, SPR signal changes the transmitted intensity through the fibre and can be detected by a power meter placed at the other end of the fibre. As the SPR is related to the thickness on the thin film hence the same can be estimated. Unfortunately, this is also an intrusive in-situ measurement technique. Besides, this technique responses only for the lower thickness levels and is insensitive to the higher thickness (above 100 nm) levels. Furthermore, this technique is again material dependent and is applicable only for those materials exhibiting a strong SPR sensitivity.

It is observed that the most of the techniques stated above seek a prior knowledge of the properties of the material and the substrate. Some of the techniques additionally require the information on the environment under which deposition is being performed (e.g gas pressure, temperature etc.) along with an appropriate physical model. Moreover, the above schemes either measure the surface profile or the thickness of the thin film and not both simultaneously. To the extent of our knowledge, there is no single available technique that can provide the complete information of both surface profile over the entire film surface and thickness of the thin film simultaneously in real-time during the growth process.

In the present thesis, a programmable grating array based zonal wavefront sensor (GAWS) [40] is developed and tested in-situ for the simultaneous measurement of both thickness and surface profile of thin film during growth process in a PLD system. The proposed measurement scheme overcomes some of the limitations of the existing in-situ techniques. It works for any reflecting substrate and any reflecting material without requiring any prior knowledge regarding their properties or require any physical model for the analysis. In the proposed technique, a collimated laser beam is incident onto the surface, the reflected beam from the sample surface is directed towards the grating array based zonal wavefront sensor. The reflected beam from the test sample (thin film in the present case) carries information about the sample and the wavefront sensor senses the change in the wavefront which is then converted into the thickness and surface profile information of the thin film.

When a plane wavefront reflects from a surface, the shape of the wavefront undergoes a change. Change in shape of the wavefront is also known as distortion. A measure of the distortion in the wavefront can provide information on the surface profile of the reflecting surface. The device that measures the distortion in the wavefront is known as the wavefront sensor. Wavefront sensors play a significant role in diverse areas such as in astronomy to build adaptive optics for astronomical telescopes [41, 42], ophthalmology for perfect correction of human vision [43], semiconductor industry to test the flatness of the surface [44, 45], free-space optical communication to transmit and receive the data accurately [46–48], etc. Based on the working principle, wavefront sensors are broadly classified into two types: zonal [49] and modal wavefront sensors [50]. In zonal wavefront sensor, the wavefront is dissected into a number of spatial zones termed as sampling zones. The wavefront slope is measured within these small individual zones. The integration of all these zone wise slope measurements provide complete shape of the wavefront. While in modal wavefront sensor, the wavefront is expressed in terms of a set of orthogonal aberration modes [51, 52]. Since the basis set for modal wavefront sensor is an orthogonal polynomial, the presence of each polynomial can be detected by intensity measurement when beam is incident on a modal wavefront sensor [53].

The Shack-Hartmann wavefront sensor (SHWS) [44, 54] is the most well known zonal type of wavefront sensors for measuring the shape of a wavefront. The SHWS consists of a two-dimensional array of micro lenses, known as lenslet array followed by an array detector. The detector is placed at the common focal plane of the lenslet array. The lenslet array dissects the incident wavefront into many small subapertures and an array of focal spot pattern is created in the detector plane . However, if the incident wavefront experiences any distortion, the focal spots will get displaced from their reference locations. The shifts in the focal spots can be employed to measure the local slopes of wavefront for each zone. From the local slopes one can then estimate the wavefront using an appropriate zonal or modal reconstruction algorithm [55, 56].

Despite its popularity, the conventional SHWS has several limitations that influence its performance. Firstly, the lenslet array has a fixed geometry and it cannot be reconfigured once it is fabricated. Consequently if the incident wavefront has a large distortion or a strong curvature, the focal spot from one zone may enter its neighbouring zones giving rise to crosstalk between the neighbouring sampling zones. As a result, it may not be possible to estimate the wavefront accurately. This reduces the effective dynamic range of the sensor. A movable mask can be placed in front of the lenslets array to increase the dynamic range by reducing the cross-talk between the detector sub-apertures. However in such a case, the focal spot does not carry the average slope of the entire zone and carries only information that passes through the mask. Additionally, in a conventional SHWS each lenslet has a fixed focal length and that cannot be modified, as a result the sensitivity of the sensor that is decided by the focal length is also fixed. However based on the applications, there may be a need to increase or decrease the sensitivity of the wavefront measurement. Further the fixed geometry of the lenslet array stipulates that a beam of a given size can be sampled by a certain maximum number of zones and a smaller beam unless optically magnified can not contain the same number of zones. Yet another limitation of the conventional SHWS is the need of a perfect reference beam, as the sensor does not have the capability to self correct an imperfect reference beam.

The above limitation of the SHWS are overcome to some extent in the grating array based zonal wavefront sensor designed and constructed in this thesis.

The grating array based zonal wavefront sensor consists of an array of plane diffraction gratings followed by a single focusing lens and a detector array. The GAWS can be implemented using a liquid crystal spatial light modulator (LCSLM) employing the principle of a computer generated holography (CGH) technique [57]. When a collimated laser beam is incident on the grating array, one of the diffracted orders, for instance, the +1 diffraction order can be focused on the detector array to form an array of focal spots. These focal spots get shifted from their reference position if the incident wavefront contains some distortion. Thus the unknown wavefront can be estimated using a procedure similar to the SHWS. However being implemented by a device like LCSLM, the grating array has the much needed reconfigurability in real time. Besides, each grating can in fact be a hologram capable of incorporating a correcting phase to the incident wavefront for each sampling zone. The GAWS thus has many exciting features such as flexible dynamic range and flexible spatial resolution without the use of any mask. The grating array can be reconfigured to have the same number of zones for beams of different sizes. The focal length of the lens following the grating array can be changed as per the requirement to adjust the sensitivity. Additionally if the reference beam is imperfect, the appropriate correction factors can be applied holographically to each grating so that reference focal spot pattern can be brought to near ideal positions. The spatial resolution of the GAWS can also be enhanced significantly without compromising the sensing frame rate [58].

Owing to the number of flexibilities offered by the GAWS it can be integrated easily with any thin film deposition system. Although there is some loss of light in the GAWS, yet the diffraction efficiency provided by the LCSLM is sufficient for the proposed scheme even using a relatively low power laser. In this thesis, a basic GAWS is assembled and tested for its working. After successfully testing for its functioning, the GAWS set-up is integrated with a pulsed laser deposition (PLD) unit and tested for its compatibility and suitability for the online monitoring of thickness and surface profile of the thin film during deposition.

In the present work, with the PLD, the sensor is kept running at regular intervals of time during the deposition process. The reconstruction algorithm is modified in order to enable the estimation of both, surface profile and thickness simultaneously as a function of time during deposition. This is achieved by making judicious use of the temporal surface profiles to obtain the corresponding thickness profiles. The measurements are compared with other technique offline, post deposition. It is observed that there is a reasonable agreement in the final result by two techniques. The sensing scheme is then further modified to enhance the sensitivity and dynamic range of the sensor. Though the implementation of the sensor is demonstrated on a PLD system but it is very general and can be implemented on any thin film deposition technique having the access of two suitable ports for launching the collimated laser beam onto the substrate on which thin film is to be deposited and for detecting the reflected beam from the film. The present scheme works for any reflecting substrate and any reflecting material layer without requiring any prior knowledge regarding their properties.

The overall thesis work is arranged in six chapters. Below a brief overview of each chapter is stated.

Chapter1 (General Introduction), begins with the brief description on importance and applications of thin films. Various tools to measure the surface profile and thickness in-situ are highlighted along with their salient features and limitations. There is a brief discussion on the wavefront sensors, especially the Shack Hartmann wavefront sensor (SHWS) and their applications. Then the function of grating array based wavefront sensor (GAWS) is described along with its relative advantages. The chapter ends with a short discussion on the implementation of GAWS to measure the surface profile and thickness of the thin film in-situ in a deposition system.

Chapter2 (Computer Generated Holography), describes the principle of computer generated holography and generation of user defined wavefront using binary holograms that can be realized with an LCSLM.

Chapter3 (Development of grating array based wavefront sensor using a liquid crystal spatial light modulator), discusses the design and development of the grating array based zonal wavefront sensor in detail. The primary features and basic advantages of the GAWS are explained. This chapter also discusses the use of the zonal reconstruction algorithms applied on the slope data. Finally, experimental implementation of GAWS is detailed.

Chapter4 (In-situ surface profiling and thickness measurement using the GAWS integrated with the pulsed laser deposition system), is on the the integration of the GAWS setup with the PLD system for in-situ surface profile and thickness measurement. This chapter begins with a brief description of the PLD system. It then presents an illustration of the optical arrangement of the entire system. This is followed by an explanation of the estimation process to obtain the thickness and surface profile information as a function of time, simultaneously. Finally, experimental results are presented to confirm that GAWS is an efficient in-situ measurement technique for thin film deposition systems for monitoring the online growth of the film during deposition as a function of time.

Chapter5 (Development of zonal wavefront sensors with enhanced dynamic range and enhanced sensitivity), starts with a modification in the proposed zonal wavefront sensing scheme that can provide higher wavefront measurement sensitivity applicable for thin films requiring high level of flatness. This is followed by another modification that can provide enhanced dynamic range useful for thin film specimens containing extremely high slopes. Working principle of both the schemes have also been experimentally demonstrated.

Chapter6 (Conclusion and Future Prospects), the last chapter, concludes the thesis and highlights the major achievements of the thesis work. Finally the future scope of the thesis is outlined.

CHAPTER 2

Computer Generated Holography

Introduction

This chapter discusses about the shaping the wavefront of a laser beam using computer generated holography technique. The chapter begins with a brief discussion on the working principle of classical holography. Later the same is utilized to elaborate the computer-generated holography technique and construction of binary holograms. The chapter ends with a brief discussion on how binary holograms can be realised in a ferroelectric liquid crystal spatial light modulator.

2.1 Classical holography

The concept of holography and hologram was invented in 1948 by Hungarian scientist **Dennis Gabor**, who has been awarded the Nobel Prize for his work in 1971. The term hologram is taken from the Greek words holos (whole) and gramma (message), which means storing the complete message of an object, say, in a photographic plate. The phenomenon of holography comprises two parts. In the first part, the interference between the reference beam and an object beam carrying the information of the object is recorded on a photographic plate. In the second part, the recorded interference pattern which is also called the hologram is used to reconstruct the object beam [59].

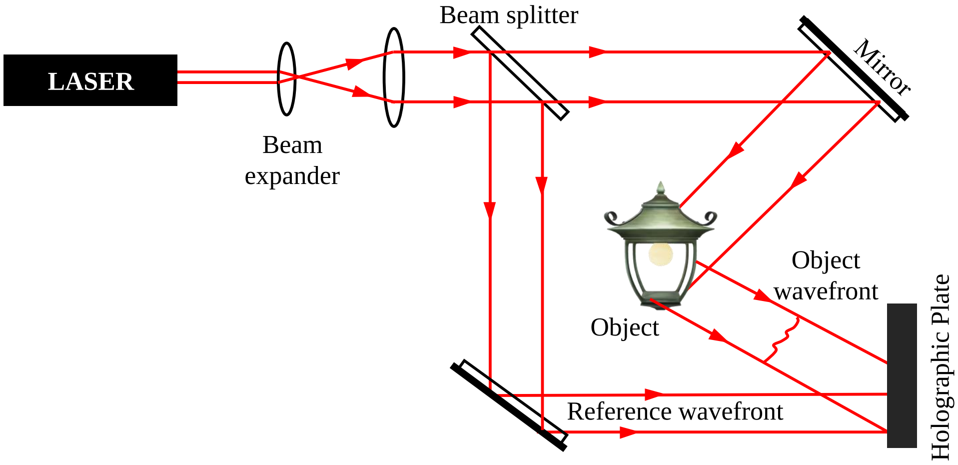

Fig. 2.1 Diagram showing the recording of the interference pattern between the reference beam and the object beam.

Figure 2.1 shows schematic of the process in the first part. A spatially coherent beam preferably a laser beam is expanded and collimated. This beam is then divided into two mutually coherent beams one of which is considered as a reference beam while the other is allowed to fall on the object. The light scattered by the object carries information about the shape of the object in its wavefront and is known as the object beam. The reference beam and the object beam are then allowed to overlap on a photographic plate. Since the two beams are mutually coherent they will produce a stable interference pattern which will be recorded on the photographic plate.

Let us consider that the complex amplitude of the reference beam and object beam are $R(x,y) = A_r e^{i\varphi(x,y)}$ and $O(x,y) = A_o e^{i\Phi(x,y)}$, where $\varphi(x,y)$ and $\Phi(x,y)$ are the phase profiles of the reference beam and the object beam, respectively. Therefore the interference pattern produced by the superposition of the two waves is given by,

$$I(x,y) = |R(x,y) + O(x,y)|^2 \tag{2.1}$$

$$I(x,y) = |R(x,y)|^2 + |O(x,y)|^2 + R(x,y)^* O(x,y) + R(x,y) O(x,y)^* \tag{2.2}$$

$$I(x,y) = A_r^2 + A_o^2 + 2 \cdot A_r \cdot A_o \cdot \cos[\Phi(x,y) - \varphi(x,y)] \tag{2.3}$$

where we have considered that the reference and the object beam have real and uniform amplitude profiles. Therefore, the photographic plate will record the interference pattern which will primarily contain the phase information of the object beam and the reference beam as given by Eq. 2.3. The photographic plate when developed will have a transmittance function proportional to $I(x,y)$. This recorded interference pattern as stated already is called the hologram of the given object beam. In the second part of the holography, the hologram is placed in a manner similar to the photographic plate during recording of the hologram. The reference beam illuminates the hologram at the same angle of incidence and gets diffracted by the hologram as shown in Fig. 2.2. To understand diffraction of light by the hologram theoretically we consider that the transmittance function of

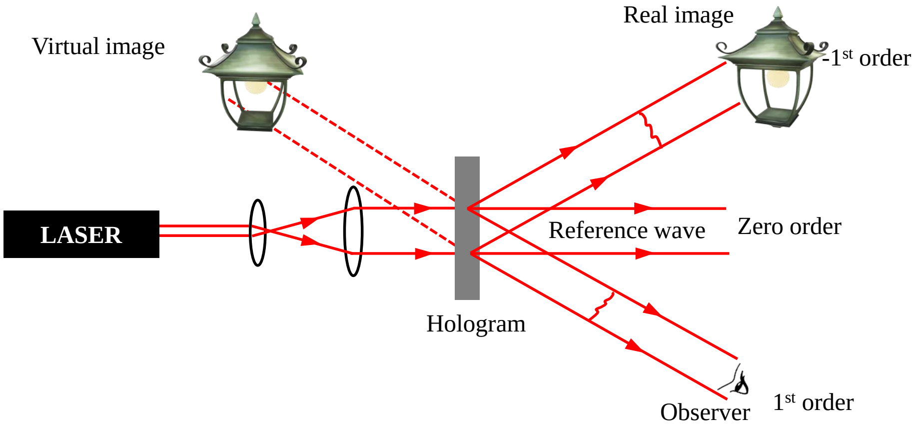

Fig. 2.2 Diagram showing the reconstruction of the object beam wavefront

the hologram is given as $t(x,y) = \alpha I(x,y)$ where α is a constant. Since the hologram is illuminated by the reference beam, the complex amplitude of the light just after the hologram is given as

$$H(x,y) = \alpha.A_r e^{i\varphi(x,y)}[A_r^2 + A_o^2 + A_r \cdot A_o e^{i(\Phi(x,y)-\varphi(x,y))} + A_r \cdot A_o e^{-i(\Phi(x,y)-\varphi(x,y))}] \quad (2.4)$$

Usually, the reference beam is considered as a plane wave. For such a reference beam we can consider $\varphi = 0$. Hence Eq. 2.4 becomes

$$H(x,y) = \alpha[A_r^3 + A_o^2 A_r + A_r^2.A_o e^{i\Phi(x,y)} + A_o.A_r^2 e^{-i\Phi(x,y)}] \quad (2.5)$$

Equation 2.5 indicates that the diffracted beam from the hologram comprises three beams, namely the undiffracted or the 0 order beam represented by the first and second terms on the right hand side, + 1 order diffracted beam given by the third term and -1 order diffracted beam given by the fourth term on the RHS. It is further noticed that the +1 order beam carries the same phase profile as the object beam while the -1 order beam carries the complex conjugate of the object beam phase profile. Hence, the +1 and -1 order beams constitute the object beam and the conjugate of the object beam respectively, as used during the recording of the hologram. As a result, if one looks through the hologram opposite to the direction of the object beam, one will see a virtual 3D image of the object at the same location as the object during recording. This is because the +1 order diffracted beam is the reconstructed object beam containing exactly the same phase profile as the object beam. The conjugate of the object beam on the other hand produces a real 3D image of the object.

2.2 Computer generated holography

We have seen in the above section that if we illuminate a recording of the interference pattern between the reference beam and the object beam, the object beam wavefront can be reconstructed. Therefore, if the interference pattern is known or if it can be computed then the same can be used to fabricate the hologram. Such a hologram which is constructed from the computed interference pattern between the reference beam and the object beam is called computer generated hologram. To compute the interference pattern one requires the numerical description of the reference beam and the object beam. Thus, if we have the mathematical description of both the beams we should be able to reconstruct the respective object beam even if there is no physical object to create such an object beam. The above property of the hologram can be used to generate an arbitrary wavefront whose numerical or mathematical description is known. In this work, we are going to use computer generated binary holograms to shape the wavefront of an incident laser beam.

2.2.1 Construction of binary hologram

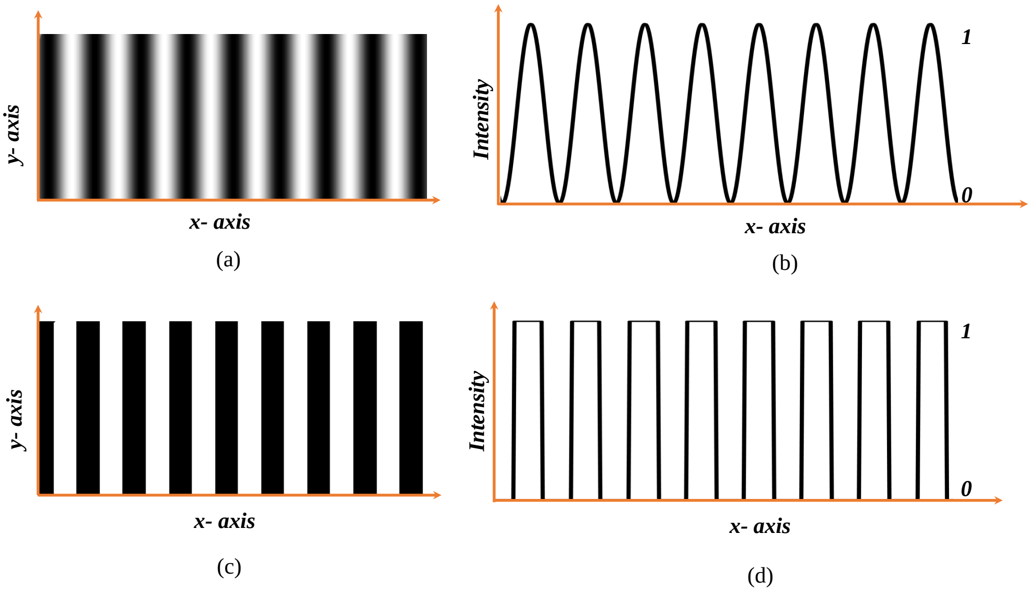

Fig. 2.3 (a) Interference fringes due to the superposition of the two plane waves, and (b) the corresponding line plot showing the sinusoidal intensity distribution. (c) and (d) show the binarised version of figures (a) and (b).

Computer generated binary holograms was demonstrated successfully by Lee et al. [60] several decades back. Figure 2.3 (a) shows the interference pattern between two plane waves which can be assumed to be describing the transmittance of a given hologram. A line plot of the interference pattern as seen in Fig. 2.3 (b), shows sinusoidal variation of the intensity with distance. If we apply a threshold to the interference pattern in Fig. 2.3 (a) it results in a thresholded or binarized pattern as seen in Fig. 2.3 (c) whose line plot is seen in Fig. 2.3 (d). Therefore, the binary hologram comprises two transmittance values which for simplicity can be considered as 0 and 1. Below we describe the algorithm to construct a binary amplitude hologram. Let us consider that $e^{i\Phi(x,y)}$ represents the complex amplitude of the object beam to be reconstructed. The hologram plane is described by the coordinate (x,y) where, x and y vary between -1 to +1. The transmittance function of the respective binary hologram as per the algorithm [57, 61] is given as

$$t(x,y) = \begin{cases} 1 & \text{for } \cos\Phi(x,y) \leq 0 \\ 0 & \text{for } \cos\Phi(x,y) > 0 \end{cases} \tag{2.6}$$

The algorithm represented by Eq. 2.6 can be used to construct the transmittance function of a binary hologram for the reconstruction of an object beam with wavefront $\Phi(x,y)$. Here we consider that both the reference and the object beam have unit amplitude. The binary hologram such as the above modulates the amplitude of the incident beam. However the same algorithm can be modified to construct binary phase hologram where only the phase part of incident beam is modulated. Since light beams associated with most of the optical systems have circular cross section, therefore we multiply the transmittance function of the binary hologram with a circ function $circ(x,y)$. Modified transmittance function of the binary hologram is given as

$$T(x,y) = t(x,y) * circ(x,y) \tag{2.7}$$

Generation of an arbitrary wavefront

The phase Φ of the object beam to be generated can comprise of two terms, namely x and y tilts and a pure phase term ϕ. Hence, $\Phi(x,y) = m_x x + m_y y + \phi(x,y)$ where,

$(m_x,\ m_y)$ describe tilts along x and y and $\phi(x,y)$ is the phase shift with respect to the plane perpendicular to the propagation direction of the object beam. When the reference beam is incident on the binary hologram, it gives rise to a number of diffracted beams. The origin of these diffraction orders can be understood by considering the Fourier series analysis of the plot of $t(x,y)$ against $\Phi(x,y)$. We see that as Φ changes from 0 to 2π, the plot of $t(x,y)$ describes a square wave. Hence, we can write the Fourier series expansion of $t(x,y)$ as

$$t(x,y) = \frac{1}{2} + \frac{1}{\pi}\left[e^{i\Phi} + e^{-i\Phi} + \frac{1}{3}(e^{3i\Phi} + e^{-3i\Phi}) + \frac{1}{5}(e^{5i\Phi} + e^{-5i\Phi}) + \ldots\right] \tag{2.8}$$

The right hand side of Eq. 2.8 contains all the diffraction orders that results in when the reference beam is incident on the binary hologram. The first term of the expression represents the zero order beam while the second and third terms represent the +1 and -1 order beams. There are higher order beam such as +3 and -3 order beams represented by the fourth and fifth terms in the expression. As we see that the +1 order beam has the complex amplitude $e^{i\Phi(x,y)}$ and contains net energy which is $\frac{1}{\pi^2} \times 100$ % of the net incident energy in the reference beam. The energy in the higher order diffracted beams are smaller by a proportional amount.

Therefore, when the binary hologram is placed at the front focal plane of a lens, its Fourier transform is obtained at the back focal plane. The diffraction pattern of the hologram at the back focal plane can thus be obtained numerically by taking Fourier transform of the transmittance function of the hologram.

We numerically construct two binary holograms using $\Phi(x,y) = 10\pi x$ and $\Phi(x,y) = 5\pi x + 5\pi y$. We then compute the respective Fourier transforms to obtain the resulting focal intensity distributions. Figures 2.4 (a) and (c) show the two binary holograms and Figs. 2.4 (b) and (d) show the respective Fourier transforms. It is seen that the position of the +1 order beam with respect to the 0 order beam is decided by values of m_x and m_y. If we consider that the binary hologram has a diameter d_{hol} and is illuminated by a beam of wavelength of λ the position of the +1 order focal spot with respect to the zero

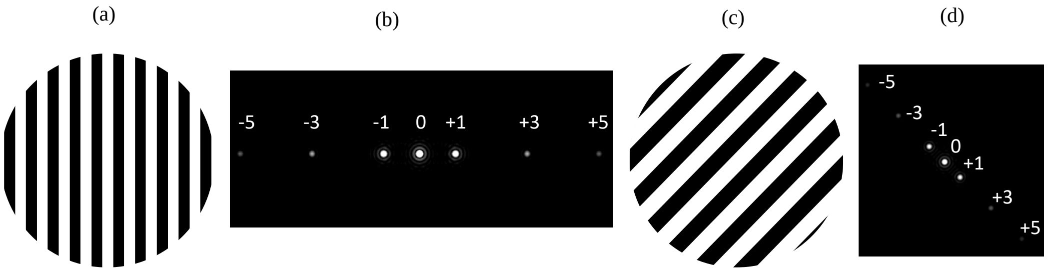

Fig. 2.4 Images of binary amplitude holograms using (a) $m_x = 10\pi$, $m_y = 0$ and (c) $m_x = 5\pi$, $m_y = 5\pi$. (b) and (d) are the numerically obtained focal intensity distribution in the Fourier plane of the binary holograms (a) and (c), respectively.

order is given as $(f\frac{m_x\lambda}{d_{hol}}, f\frac{m_y\lambda}{d_{hol}})$, where f is the focal length of the lens. In addition to incorporating the x and y tilt into the +1 order beam, we can incorporate phase distortion or aberrations through the pure phase term $\phi(x,y)$. Phase profile introduced into the +1 order beam in such a manner is referred to as holographically introduced phase or aberrations, thorough out this thesis.

Incorporation of Zernike mode aberrations

Zernike polynomials constitute a complete set of orthogonal basis functions which can be used to describe aberrations in light beams. In this work, we use single index Zernike polynomials as defined by Noll et al. [62]. The table seen in Fig. 2.5 shows the mathematical description of a few Zernike modes, $Z_4 \longrightarrow Z_{11}$, the color representation of the phases and the resulting point spread functions. Therefore, in order to holographically introduce a linear combination of Zernike modes we define $\phi = \Sigma a_i\, Z_i(x,y)$. Here, a_i represents the root mean square (RMS) amplitude of the i^{th} Zernike mode.

We again numerically construct binary holograms using $\Phi(x,y) = 10\pi x + 10\pi y + Z_9$ and $\Phi(x,y) = 10\pi x + 10\pi y + Z_7$ which are shown in Figs. 2.6 (i) and (iii). The numerically obtained intensity of the respective +1 order focal spots are seen in Figs. 2.6 (ii) and (iv).

i	**Z_i *(x, y)***	**Aberration Name**	**Phase**	**PSF**
4	$\sqrt{3}\,\{2(x^2+y^2)-1\}$	Defocus	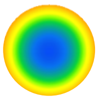	
5	$2\sqrt{6}\;xy$	Astigmatism – 45°	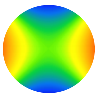	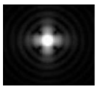
6	$\sqrt{6}\,(x^2-y^2)$	Astigmatism – 90°	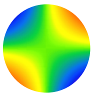	
7	$\sqrt{8}\,\{3(x^2+y^2)-2\}y$	Y – coma	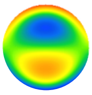	
8	$\sqrt{8}\,\{3(x^2+y^2)-2\}x$	X – coma	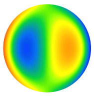	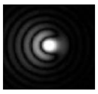
9	$\sqrt{8}\,\{3x^2y-y^3\}$	X- trefoil	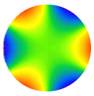	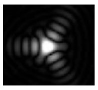
10	$\sqrt{8}\,\{x^3-3x^2y\}$	Y- trefoil	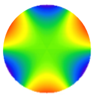	
11	$\sqrt{5}\,\{6(x^2+y^2)^2-6(x^2+y^2)+1\}$	spherical	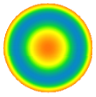	

Fig. 2.5 List of the mathematical form of a few Zernike mode aberrations, false color image of the respective phase profiles and resulting point spread functions.

2.3 Implementation of binary hologram using liquid cr-ystal spatial light modulator

In the above section we have discussed the numerical construction of binary holograms to realise arbitrary wavefront in the +1 order diffracted beam. However the computed binary hologram needs to be transformed into a physical hologram via some process. One convenient way to realise a binary hologram is by using computer controlled liquid crystal devices. Liquid crystal is a state of matter which lies intermediate between the

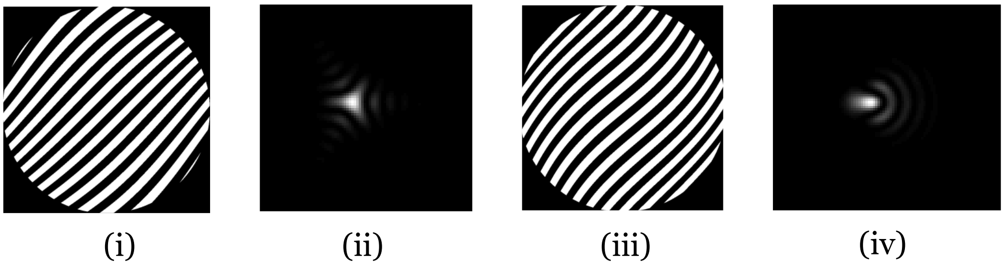

Fig. 2.6 Images of binary holograms (i) using $\Phi(x,y) = 10\pi x + 10\pi y + Z_9$ and (iii) using $\Phi(x,y) = 10\pi x + 10\pi y + Z_7$. (ii) and (iv) are the numerically obtained focal intensity distribution of the +1 order beam corresponding to the holograms (i) and (iii), respectively.

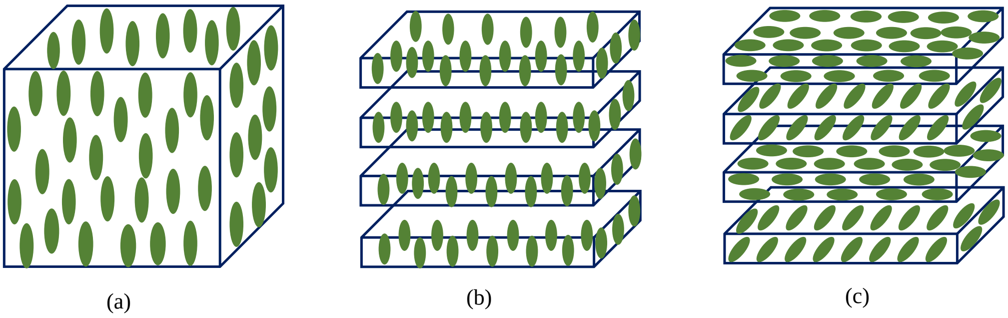

Fig. 2.7 Diagrams showing typical distribution of liquid crystal molecules in (a) nematic, (b) smectic and (c) cholestric phases.

solid and liquid states [63]. Liquid crystal molecules are of three major types, namely nematic, smectic and cholesteric [64]. In the nematic phase the molecules are distributed randomly but they tend to have a common orientation. The orientation of the molecules can be changed by applying an electric field across the liquid crystal volume [65]. In the smectic phase the molecules are arranged in layers with all the molecules in a given layer having a specific orientation. In the cholesteric phase again the liquid crystal molecules are arranged in layers however the orientation of the molecules changes from layer to layer in a helical fashion [66]. Figures 2.7 (a), (b) and (c) show the typical arrangements of molecules in the nematic, smectic and cholestric phases, respectively.

In this thesis, we use devices made of ferroelectric liquid crystal molecules which is a liquid crystal of smectic type C*. Ferroelectric liquid crystal molecules [67, 68]

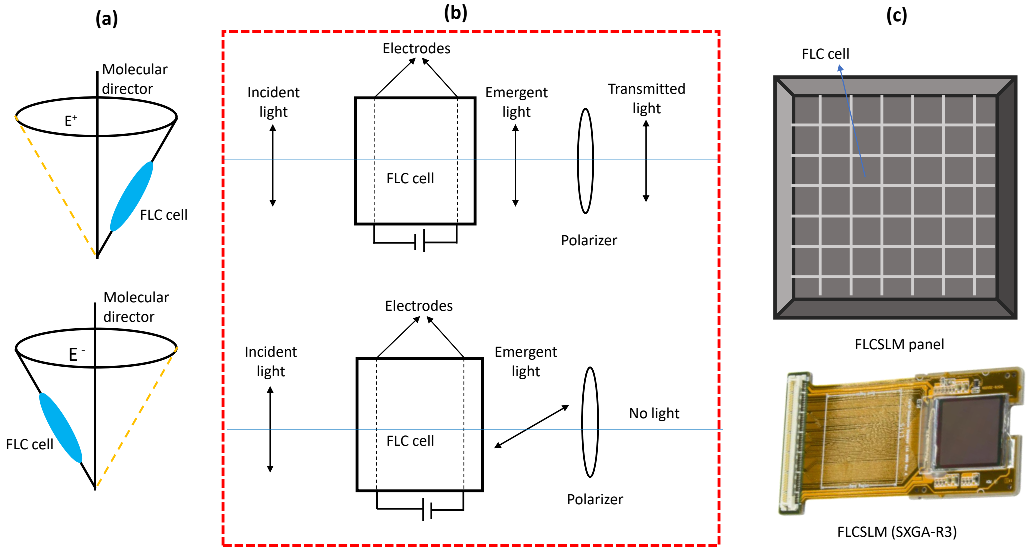

Fig. 2.8 (a) Bistability property of ferroelectric liquid crystal molecule in presence of electric field of opposite polarity, (b) polarization rotation of the incident light beam by an FLC cell as the polarity of the electric field changes, and (c) arrangement of FLC cells in the form of 2D array in the FLCSLM and a snap of the commercial SXGA-R3 display panel. In the figure the double arrows indicate the polarization directions.

are bistable in nature and they take an orientation based on the direction of the applied electric field. Therefore, the orientation of the molecules can be switched through a certain angle (say, 45^o) by altering the polarity of applied electric field as shown Fig. 2.8 (a). The liquid crystal molecules are put in a transparent cell with two electrodes on the two opposite sides of the cell. The thickness of the cell is so decided that a laser beam with appropriate polarization passing through the cell undergoes a polarization rotation similar to passing through a half waveplate. Therefore, a cell can be oriented in such a way that if a polarizer is used on the emergent side of the cell with its axis made parallel to the polarization axis of the beam then the polarizer will transmit or obstruct light based on the polarity of the applied electric field across the cell. The binary modulation of the intensity of the emergent beam by a ferroelectric liquid crystal cell is shown in Figs. 2.8 (b). Such liquid crystal cells can be arranged in a two dimensional array as shown in Figs. 2.8 (c). Such an arrangement of liquid crystal cells is known as liquid crystal spatial light modulator (LCSLM). We use commercially available ferroelectric liquid crystal spatial light modulator (FLCSLM) of Forth Dimension Display (model no. SXGA-R3). This FLCSLM is a reflective type and hence modulation takes place in the reflected beam. To implement the binary hologram we write the numerically obtained binary pattern onto the FLCSLM display via a computer interface. The light transmission property of the individual FLC cell gets modified in accordance with the pixel value in the binary pattern and the same can also be reconfigured in real time.

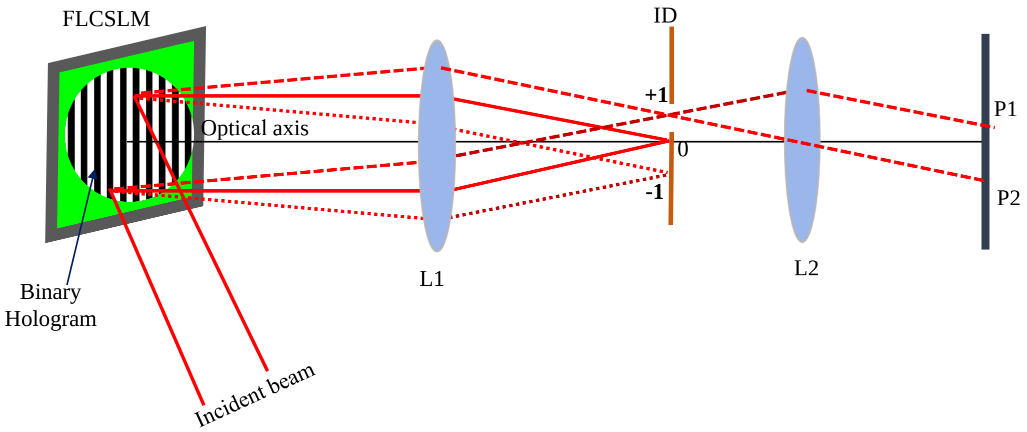

Fig. 2.9 Schematic of a basic setup using the FLCSLM acting as the binary hologram to realize a user defined wavefront.

Figures 2.9 shows a basic setup to generate a user defined object beam wavefront using a binary hologram displayed on an FLCSLM. The binary hologram to generate the user defined phase profile (Φ) is constructed digitally in a computer and the same is written on the FLCSLM panel. A collimated laser beam considered as the reference beam is incident the FLCSLM display acting as the binary hologram in the reflection mode. The emergent beam just after the hologram undergoes polarization modulation based on the pixel value of the binary hologram. Therefore, it leads to three prominent diffraction orders, namely 0, +1, and -1 order beams. The diffracted beams are collected by a lens L1 and are focused onto the iris diaphragm (ID). By choosing the appropriate values of $(m_x,\, m_y)$, the +1 order can be separated from the other orders and transmitted through ID. This beam can be recollimated using lens L2 to realize an exact replica of the phase profile (Φ) in the plane P1P2 which is arranged optically conjugate to the FLCSLM plane.

2.4 Conclusion

In this chapter we have described working principle of holography and elaborated how the principle of classical holography is utilized to construct the computer generated holograms. We have then discussed an algorithm to construct binary holograms which when illuminated with the reference beam gives rise to a user defined object beam wavefront. We have explained how binary hologram can be used to define the position of the +1 order beam with reference to the zero order beam and how the +1 order beam can be incorporated with a linear combination of aberration modes. We have ended the chapter with an illustration of the basic experimental arrangement using the FLCSLM to implement the binary holograms.

CHAPTER 3

Development of grating array based wavefront sensor using a liquid crystal spatial light modulator

3.1 Introduction

This chapter discusses the implementation of a grating array based zonal wavefront sensor of light beams which will be used later in the thesis. The chapter first elaborates the working principle of a Shack-Hartmann wavefront sensor. This is followed by a description on the geometry of the wavefront sensor and the phase reconstruction algorithms. The chapter highlights some important limitations of the Shack-Hartmann wavefront sensor. It then discusses the principle of the grating array based zonal wavefront sensor, which uses an array of binary diffraction gratings in conjunction with a focusing lens. An experimental arrangement to perform a proof of principle experiment is then elaborated. The chapter ends with the illustration of experimental results to validate the working of the grating array based zonal wavefront sensor.

3.2 Wavefront sensing and wavefront sensor

We know that a wavefront is an imaginary surface associated with a light beam that corresponds to points with constant phase or with equal optical path length from the source of light. Figure 3.1 shows two types of wavefronts, a spherical wavefront (W1) originating from the point source (S) kept before a lens later becomes a plane wavefront (W2) after the lens. In case of a spherical wavefront rays diverge in all the directions. While for the plane wavefront, the rays travel in one direction.

When a plane wave written as $E(x,y,z,t) = E_o e^{ikz} e^{-2\pi i \nu t}$ propagating along the z-axis is transmitted through a medium or reflected by a surface, the shape of the wavefront gets changed as depicted in Figs. 3.1 (i) and (ii), respectively. Such a wavefront (W3) is now said to be aberrated. The reflected or transmitted wavefront has an unknown phase profile φ so that the wave now is written as $E(x,y,z,t) = E e^{ikz} e^{-2\pi i \nu t} e^{i\varphi}$.

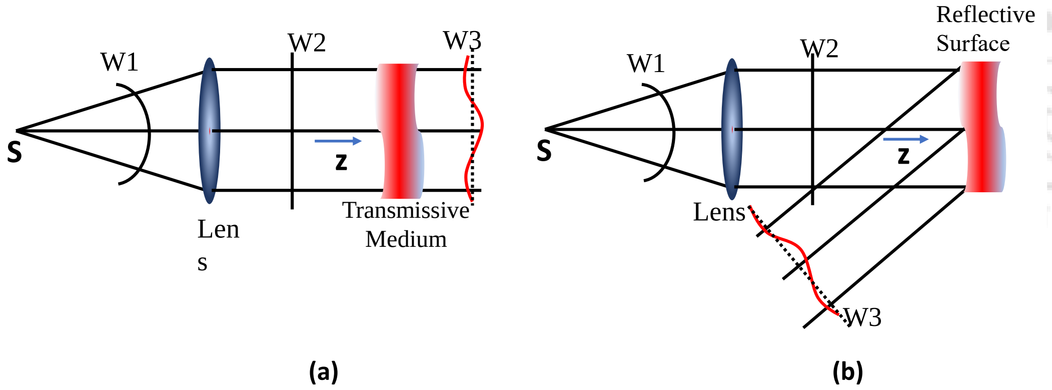

Fig. 3.1 A spherical wavefront is made planar by a lens and then gets aberatted on (a) transmission through a medium or (b) reflection from a surface.

The technique of measuring the unknown phase profile or the wavefront of the incident beam is known as wavefront sensing. As discussed previously, the wavefront sensors are classified into two groups, namely the zonal wavefront sensors (such as Shack-Hartmann wavefront sensor [69], pyramid sensor [70, 71], etc.) and modal wavefront sensors (such as curvature sensor [72, 73], bias beam based modal wavefront sensor [50], etc.). In the present thesis work, we consider the zonal type of wavefront sensor since it is more robust and suitable for measuring wavefronts of arbitrary shape. In a zonal wavefront sensor, the incident wavefront is initially divided into a number of constituent zones or sub-apertures and phase over each zone is estimated before reconstructing the resultant phase profile. The most well known and popular zonal wavefront sensor is the Shack-Hartmann wavefront sensor.

3.3 Shack-Hartmann wavefront sensor

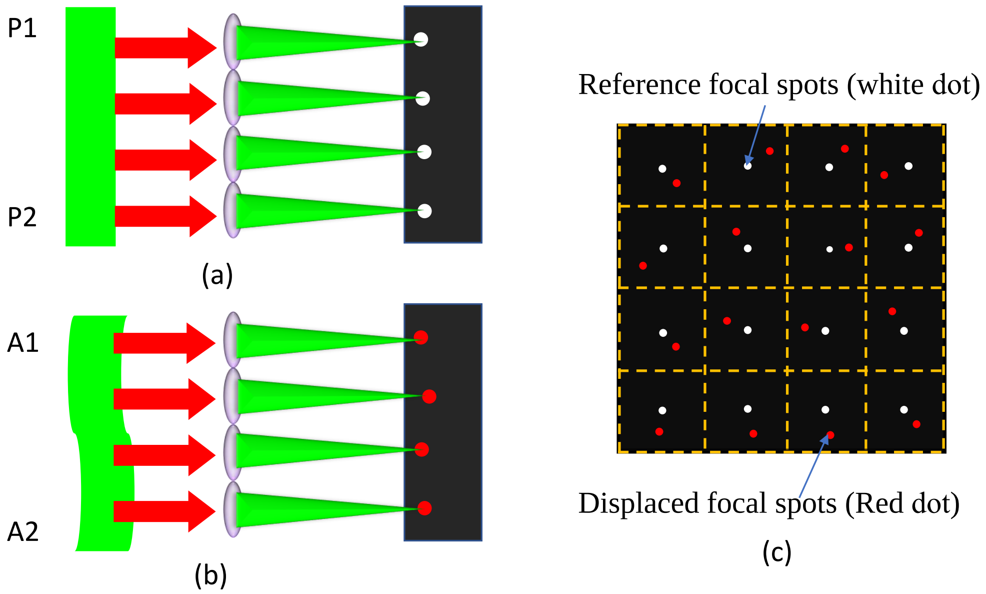

Fig. 3.2 Diagram of (a) a plane wavefront, and (b) a distorted wavefront incident on the lenslet array giving rise to reference and shifted focal spot array shown in (c).

A Shack-Hartmann wavefront sensor (SHWS) consists of a two-dimensional array of micro-lenses, called lenslets, followed by an array detector. When the incident wavefront passes through the lenslet array, it gets dissected by each lenslet and focused onto the detector array placed at the common focal length of the lenslet array. Figure 3.2 illustrates the working principle of the SHWS. When a plane wavefront denoted by P1P2 passes through the lenslet array, it forms a regular array of focal spots in the detector plane, shown as white dots in Fig. 3.2 (c). The regular array of focal spots are termed as reference focal spots. Each of these focal spots is located at the centre of the respective detector sub-aperture and on the optical axis of the respective lenslet. These focal spots are displaced from their reference positions when an aberrated wavefront (denoted by A1A2) is incident on the lenslets array. The displaced spots are shown as red dots in Fig. 3.2 (c). The amount of shifts in the focal spots are directly related to the local slopes of the wavefront. Knowing the local slopes of the incident wavefront, the unknown wavefront can be constructed by using a phase reconstruction algorithm [55, 74].

3.3.1 Measurement of local slopes

The first step of the wavefront estimation process in a Shack-Hartmann wavefront sensor is determining the focal spot locations. The focal spots are formed in an array detector. One simple way to locate the focal spot position is to find the location of the peak or the maximum in the irradiance distribution of each focal spot as obtained from the detector array output. The focal spot position say x_c and y_c can also considered as the centroid of the respective irradiance distribution. If we consider $I_{i,j}$ as the intensity of the (i,j)th pixel in the irradiance distribution then we can write

$$x_c = \frac{\sum\limits_{i,j \in AOI} x_{i,j}\, I_{i,j}}{\sum\limits_{i,j \in AOI} I_{i,j}} \quad \text{and} \quad y_c = \frac{\sum\limits_{i,j \in AOI} y_{i,j}\, I_{i,j}}{\sum\limits_{i,j \in AOI} I_{i,j}} \tag{3.1}$$

where $x(i,j)$ and $y(i,j)$ are the co-ordinates of the *(i,j)*th pixel. The summation is taken over all the pixels of the detector array within an area-of-interest (AOI) capturing a given focal spot.

Let us consider that for a given incident beam (x_r, y_r) are the reference focal spot positions and (x_s, y_s) are the shifted focal spot positions.

$$\begin{bmatrix} S^x(i,j) \\ S^y(i,j) \end{bmatrix} = \begin{bmatrix} \frac{\partial\phi(x,y)}{x} \\ \frac{\partial\phi(x,y)}{y} \end{bmatrix} = \frac{1}{d_x} \begin{bmatrix} x_s - x_r \\ y_s - y_r \end{bmatrix} \tag{3.2}$$

where $[S^x(i,j), S^y(i,j)]$ are the local slopes along the x and y directions, d_x is the distance between the lenslet array and the detector array, set as the common focal length f of the lenslet.

3.3.2 Reconstruction of wavefront

In contemporary texts, wavefront reconstruction refers to estimation of the wavefront profile from wavefront gradient data. Once the local wavefront slopes are obtained, the wavefront can be reconstructed employing either zonal [55, 74, 75] or modal [76] reconstruction algorithms. The present thesis work uses the zonal reconstruction algorithm due to its efficiency to estimate the incident wavefront of arbitrary shape.

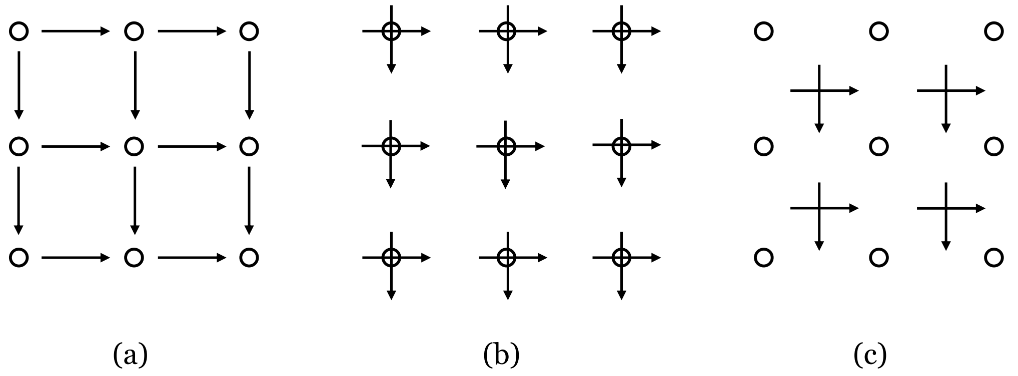
(a) (b) (c)

Fig. 3.3 Geometries for wavefront estimation, (a) Hudgin geometry (b) Southwell geometry (c) Fried geometry.

There are certain geometries relating the wavefront slopes S^x , S^y with the phase $\phi(x,y)$. Figure 3.3 depicts three such basic geometries, namely, Hudgin [77], Fried [78], and Southwell [55] geometries. In the figure, the small circles indicate the locations of phase estimation (also referred to as grid points) while the arrows represent the wavefront slopes in the x- and y-directions. In the Hudgin geometry as seen in Fig. 3.3 (a), the wavefront slope measurements are carried out at the midpoint between two neighbouring grid points for phase. In the Fried geometry as seen in Fig. 3.3 (c), both the x and y-slopes are measured at the center of four neighbouring grid points for phase. While in

Southwell geometry, as shown in Fig. 3.3 (b), the wavefront slopes are measured at the same point where the phase is to be estimated. Out of these three geometries, Southwell geometry showed its superiority as it estimates the wavefront of an incident beam more accurately [79]. Therefore in this thesis we consider two algorithms, i.e. Southwell and Pathak-Boruah, which are based on the Southwell geometry.

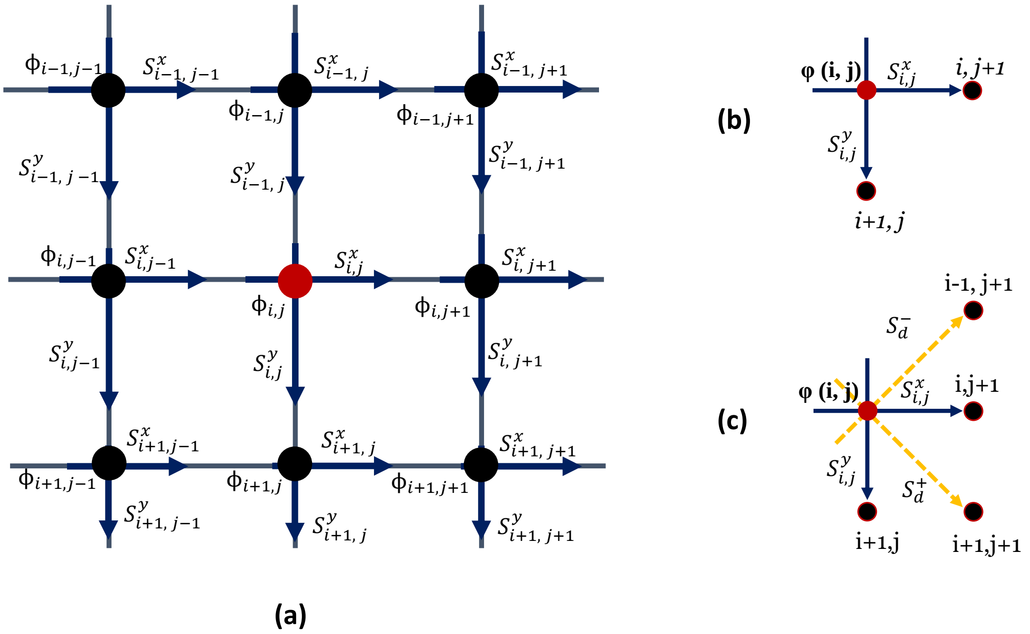

Fig. 3.4 (a) Phase and slopes at nine grid points (separated from each other by a distance of d along the horizontal and vertical direction). Relation between phase and slope in (b) the Southwell algorithm and in (c) the Pathak-Boruah algorithm. S^x, S^y, S^+, and S^-, vectors represent slopes along the horizontal, vertical, front diagonal and the back diagonal directions, respectively. The red dots represent the locations of the phase estimation points.

Fig. 3.4 (a) shows nine adjacent grid points in the Southwell geometry, represented by eight black dots and one red dot. The row indices vary from $(i\text{-}1)$ to $(i+1)$ and column indices vary from $(j\text{-}1)$ to $(j+1)$. In Southwell algorithm as shown in Fig. 3.4 (b), the mean of the slope values in the vertical or horizontal directions for two adjacent grid points is expressed in terms of the phase difference between the same two grid points. Therefore, if $\phi(i,j)$, $S^x(i,j)$ and $S^y(i,j)$ represent the phase, horizontal slope and the vertical slope, respectively, at the location *(i, j)*, then the relation between phase and slope values at the location of the red dot as in Fig. 3.4 (a) can be written as

$$\begin{aligned}\frac{S^x(i,j)+S^x(i,j+1)}{2} &= \frac{\phi(i,j+1)-\phi(i,j)}{d}\\ \frac{S^x(i,j)+S^x(i,j-1)}{2} &= \frac{\phi(i,j)-\phi(i,j-1)}{d}\\ \frac{S^y(i,j)+S^y(i+1,j)}{2} &= \frac{\phi(i+1,j)-\phi(i,j)}{d}\\ \frac{S^y(i,j)+S^y(i-1,j)}{2} &= \frac{\phi(i,j)-\phi(i-1,j)}{d}\end{aligned} \tag{3.3}$$

where d is the separation between two adjacent grid points in the vertical or horizontal direction. Now from equation 3.3

$$\begin{aligned}\phi(i,j) = {}& \frac{\phi(i,j+1)+\phi(i,j-1)+\phi(i+1,j)+\phi(i-1,j)}{4}\\ &+\frac{d}{8}[S^x(i,j-1)-S^x(i,j+1)+S^y(i-1,j)-S^y(i+1,j)]\end{aligned} \tag{3.4}$$

Equation 3.4 provides phase reconstruction expression at the central grid point according to the Southwell algorithm. However for the phase at edge or corner, the expression needs a small modification. The generalised expression for phase at any grid point, for a lenslet array of dimension $N \times N$, can be written as,

$$\begin{aligned}\phi(i,j) = {}& \frac{1}{g(i,j)}[\alpha(i,j+1)\phi(i,j+1)+\alpha(i,j-1)\phi(i,j-1)+\alpha(i+1,j)\phi(i+1,j)\\ &+\alpha(i-1,j)\phi(i-1,j)]+\frac{d}{8}[\alpha(i,j-1)S^x(i,j-1)-\alpha(i,j+1)S^x(i,j+1)\\ &+\alpha(i-1,j)S^y(i-1,j)-\alpha(i+1,j)S^y(i+1,j)]\end{aligned} \tag{3.5}$$

where,

$$\alpha = \begin{cases} 1 & \text{(for slope measurements inside the array)}\\ 0 & \text{(for slope measurements outside the array)}\end{cases} \tag{3.6}$$

and

$$g_{i,j} = \begin{cases} 2 & if\,(i=1,\, and\, j=1\, or\, N) \quad or\,(i=N,\, and\, j=1\, or\, N)\, \text{(at the corners)} \\ 3 & for \quad i=1\, or N;\, j=2 \rightarrow N-1\, \text{(top or bottom Edge)} \\ 3 & for \quad j=1\, or N;\, i=2 \rightarrow N-1\, \text{(left or right Edge)} \\ 4 & \text{(at points barring edge, and corner)} \end{cases} \tag{3.7}$$

If we have more number of slope data, we can estimate the phase at each grid point more accurately. In Pathak-Boruah phase reconstruction algorithm [74], the slope values at the diagonally located grid points in addition to the grid points in the horizontal and vertical directions, are also considered. Thus two additional slope measurements are included in the phase expression for each grid point, namely, the front diagonal (denoted by S_d^+) and the back diagonal (denoted as S_d^-) slopes, defined as

$$S_d^+(i,j) = \frac{S^x(i,j)+S^y(i,j)}{\sqrt{2}} \tag{3.8}$$

$$S_d^-(i,j) = \frac{S^x(i,j)-S^y(i,j)}{\sqrt{2}} \tag{3.9}$$

The relation between slope values and the phase at a given grid point (i,j) in the Pathak-Boruah algorithm is illustrated in Fig. 3.4 (c). Therefore we can write

$$\frac{S_d^+(i,j)+S_d^+(i+1,j+1)}{\sqrt{2}} = \frac{\phi(i+1,j+1)-\phi(i,j)}{d} \tag{3.10}$$

$$\frac{S_d^+(i,j)+S_d^+(i-1,j-1)}{\sqrt{2}} = \frac{\phi(i,j)-\phi(i-1,j-1)}{d} \tag{3.11}$$

$$\frac{S_d^-(i,j)+S_d^-(i-1,j+1)}{\sqrt{2}} = \frac{\phi(i-1,j+1)-\phi(i,j)}{d} \tag{3.12}$$

$$\frac{S_d^-(i,j)+S_d^-(i+1,j-1)}{\sqrt{2}} = \frac{\phi(i,j)-\phi(i+1,j-1)}{d} \tag{3.13}$$

Using the expressions of S_d^+ and S_d^- from Eqs. 3.8 and 3.9 in Eqs. 3.10, 3.11 and 3.12, 3.13, we have

$$\frac{S^x(i,j)+S^y(i,j)+S^x(i+1,j+1)+S^y(i+1,j+1)}{2}=\frac{\phi(i+1,j+1)-\phi(i,j)}{d} \tag{3.14}$$

$$\frac{S^x(i,j)+S^y(i,j)+S^x(i-1,j-1)+S^y(i-1,j-1)}{2}=\frac{\phi(i,j)-\phi(i-1,j-1)}{d} \tag{3.15}$$

$$\frac{S^x(i,j)-S^y(i,j)+S^x(i-1,j+1)-S^y(i-1,j+1)}{2}=\frac{\phi(i-1,j+1)-\phi(i,j)}{d} \tag{3.16}$$

$$\frac{S^x(i,j)-S^y(i,j)+S^x(i+1,j-1)-S^y(i+1,j-1)}{2}=\frac{\phi(i,j)-\phi(i+1,j-1)}{d} \tag{3.17}$$

Combining the Eqs. 3.14, 3.15, 3.16 and 3.17, we can therefore write

$$\begin{aligned}\phi(i,j)=\frac{1}{8}[&\phi(i,j+1)+\phi(i,j-1)+\phi(i-1,j+1)+\phi(i-1,j-1)+\phi(i+1,j+1)\\&+\phi(i+1,j)+\phi(i-1,j)+\phi(i+1,j-1)]+\frac{d}{16}[S^x(i,j-1)-S^x(i,j+1)\\&+S^y(i-1,j)-S^y(i+1,j)-S^x(i+1,j+1)-S^y(i+1,j+1)\\&+S^x(i-1,j-1)+S^y(i-1,j-1)-S^x(i-1,j+1)\\&+S^y(i-1,j+1)+S^x(i+1,j-1)-S^y(i+1,j-1)]\end{aligned} \tag{3.18}$$

Now the phase expression for the grid point (i,j), in general, can be written as

$$\begin{aligned}\phi(i,j)=&\frac{1}{h_{i,j}}\sum_{(\mu,\nu)=(i-1,j-1)}^{(\mu,\nu)=(i+1,j+1),(\mu,\nu)\neq(i,j)}\alpha(\mu,\nu)\phi(\mu,\nu)\\&+\frac{d}{2h_{i,j}}\sum_{\mu=i-1}^{\mu=i+1}\alpha(\mu,j-1)S^x(\mu,j-1)-\frac{d}{2h_{i,j}}\sum_{\mu=i-1}^{\mu=i+1}\alpha(\mu,j+1)S^x(\mu,j+1)\\&+\frac{d}{2h_{i,j}}\sum_{\nu=j-1}^{\nu=j+1}\alpha(i-1,\nu)S^y(i-1,\nu)-\frac{d}{2h_{i,j}}\sum_{\nu=j-1}^{\nu=j+1}\alpha(i+1,\nu)S^y(i+1,\nu)\end{aligned} \tag{3.19}$$

where

$$\alpha(\mu,\nu)=\begin{cases}1 & \text{(if } (\mu,\nu) \text{ inside the array)}\\ 0 & \text{(if } (\mu,\nu) \text{ outside the array)}\end{cases} \tag{3.20}$$

and

$$g_{i,j}=\begin{cases}3 & if(i=1, and\, j=1\, or\, N) \quad or\,(i=N, and\, j=1\, or\, N)\text{ (at the corners)}\\ 5 & for \quad i=1\, or N;\, j=2\rightarrow N-1\text{ (top or bottom Edge)}\\ 5 & for \quad j=1\, or N;\, i=2\rightarrow N-1\text{ (left or right Edge)}\\ 8 & \text{(at points barring edge, and corner)}\end{cases} \tag{3.21}$$

Therefore the unknown wavefront can be estimated from the local slope data obtained from the detector array using the Eq. 3.5 or Eq. 3.19 via different iterative methods such as Jacobi, Gauss-Seidel, or successive over relaxation method [80], [81]. It is to be noted that two important parameters of a wavefront reconstruction algorithm are the reconstruction accuracy and the processing time. Pathak-Boruah algorithm provides a better wavefront measurement accuracy than the Southwell algorithm without significantly increasing the processing time.

3.3.3 Limitations of the Shack-Hartmann wavefront sensor

The Shack Hartmann wavefront sensor is found to be useful in a wide range of applications, however one must also be aware of some of its important limitations.

The fabrication of the lenslet array involves several steps, including cutting and polishing of glass slabs. In recent times, the relevant technological advancements have minimised the fabrication efforts. However, each sensor still comprises a fixed type of lenslet array and it is not routine to change or modify the lenslet array. Therefore unless optically magnified or demagnified, the incident wavefront will be sampled by a fixed number of zones only.

The spatial resolution of the conventional Shack- Hartmann wavefront sensor is related to the diameter and the number of lenses in the lenslet array. One way to improve the spatial resolution of the sensor would be to reduce the size of the lenslet. The reduction of the size of lenslet on the other hand increases the size of the focal spot in the detector plane. This approach therefore requires a decrease in the focal length of the lenslet which degrades the sensitivity of the sensor.

Other than the resolution, the dynamic range of a Shack-Hartmann wavefront sensor is also associated with the the focal length of the lenslets. There have been efforts made to increase the dynamic range either by using new algorithms or by modifying the lenslet arrangements [82, 83]. In general, both the lenslet focal length and detector subaperture dimension together limit the maximum measurable local wavefront slope value. If the local slope of an incident wavefront exceeds the predetermined limit, the focal spot corresponding to one subaperture may move into the nearby subaperture. A decrease in the lenslet focal length to increase the upper limit of the local slope will lead to decrease in the sensitivity as stated above.

Further the fixed focal length of the lenslet array also decides the sensitivity of the sensor and it can not be easily altered even if the application demands.

In a conventional Shack-Hartmann wavefront sensor, we ideally require a perfectly plane reference wavefront. In the absence of such a perfectly plane wavefront the sensor does not provide any facility for correcting the reference wavefront.

3.4 Working principle of grating array based zonal wavefront sensor

In view of the limitations in the conventional Shack-Hartmann wavefront sensor, in this thesis we use a grating array based zonal wavefront sensor [40]. The grating array based zonal wavefront sensor (GAWS) consists of a two dimensional array of binary diffraction gratings followed by a focusing lens and a detector array. Each binary grating can in fact be considered as a binary hologram discussed in the previous chapter. Hence if a beam is incident on such a grating, it gives rise to a number of diffracted beams, the most prominent being the +1 order diffracted beam. The direction of propagation of the +1 order beam is decided by the spatial frequency of the respective grating element. Thus by properly defining the spatial frequency of the grating elements, for a plane incident wavefront we may get a regular array of focal spots in the detector plane due to focusing of the +1 order beam diffracted by each grating.

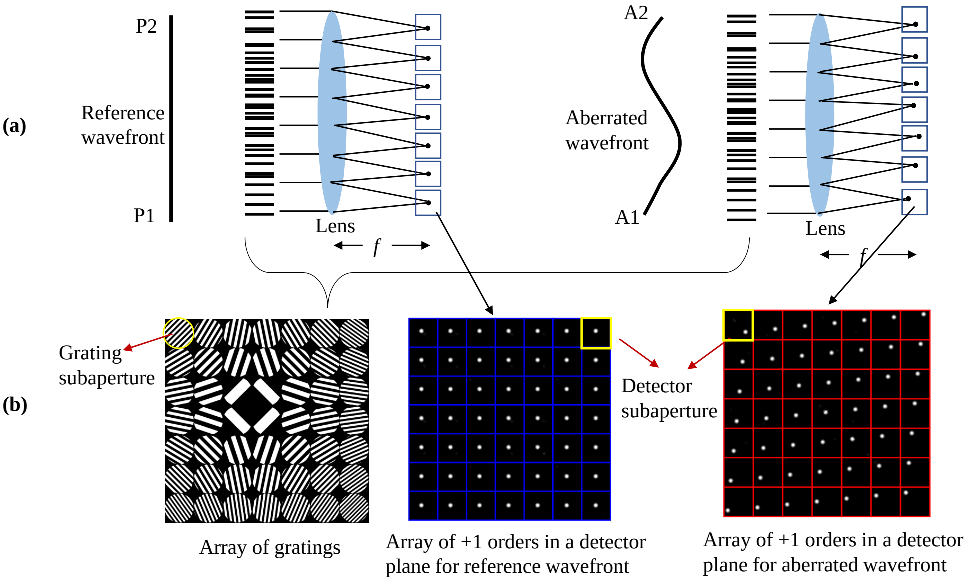

Fig. 3.5 Schematic of (a) a reference beam and an aberrated beam incident on a grating array based zonal wavefront sensor. (b) The 2D view of the 7×7 grating array and the corresponding +1 order focal spots for both reference and aberrated wavefronts.

Let us consider a two dimensional array of diffraction gratings for the GAWS. The spatial frequency (referred to as x and y tilts in the previous chapter) of the top left grating element with index (1,1) is denoted as (m_{0x}, m_{0y}) and the same for any other grating element with index (i, j) is denoted as (m^i_{0x}, m^j_{0y}). Here we apply uniform increments say, Δm_{0x} and Δm_{0y} in the spatial frequencies along x and y- directions between the adjacent grating elements. Therefore the tilts or spatial frequency for any grating element with index (i,j) can defined as

$$m_{0x}^{i} = m_{0x}^{1} + (i-1) \times \Delta m_{0x} \tag{3.22}$$

$$m_{0y}^{j} = m_{0y}^{1} + (j-1) \times \Delta m_{0y} \tag{3.23}$$

The separation between adjacent focal spots depends on the value of Δm_{0x} and Δm_{0y}. In order to form a regular grid of +1 order focal spots we choose $\Delta m_{0x} = \Delta m_{0y}$. However if the two are not equal it will give rise to a 2D array of focal spots where separation between adjacent focal spots in the x and y direction will be different. Each grating in addition to the spatial frequency components (m_{0x}^{i}, m_{0y}^{j}) representing wavefront tilts along x and y will also be described by the pure phase term.

For an aberrated incident wavefront the focal spots get shifted from their reference positions and the shifts in the focal spots can be determined from the data given by the detector array. Thus knowing the focal spot shifts the unknown wavefront can be estimated precisely the same manner as it is done in the case of the conventional Shack-Hartmann wavefront sensor discussed in the previous section. Figure 3.5 (a) shows a plane reference wavefront and an aberrated wavefront incident on a grating array consisting of (7×7) grating elements. The +1 order diffracted beams are focused by the lens onto the detector plane. Figure 3.5 (b) shows the resulting +1 order focal spots. These focal shifts are first employed to estimate the local wavefront slopes which are then used in the wavefront estimation algorithm [55, 74] as described previously to obtain the unknown phase profile.

Wavefront sensing by the GAWS provides a number of important advantages over the conventional Shack-Hartmann wavefront sensor. The most important advantage is that the array of binary gratings or binary holograms can be realized with the help of a liquid crystal spatial light modulator (LCSLM). Thus the grating array and its parameters can be reconfigured in a dynamic manner. It makes it possible that a given incident wavefront is sampled by different number of zones. It also makes it possible to dynamically alter the spatial resolution and dynamic range by changing the number and size of the grating elements. Since the focal spots are generated by a single focusing lens, the same can be replaced by another lens of a different focal length or be simply repositioned to adjust the sensitivity of the sensor. Here the grating array and the detector array are two independent components. Thus one has all the freedom to replace the detector array as well based on the requirement. Since each grating element is actually a binary hologram constructed using the computer generated holography technique, the +1 order beam from each hologram can also carry correction phase term. Thus if the reference wavefront is not perfect or aberrated, the grating array can be configured so that the array of reference focal spots in the detector plane is a regular one.

3.5 Basic components of the GAWS setup

Below we provide a brief description of the basic components of our experimental setup to implement the grating array based zonal wavefront sensor.

3.5.1 Laser

The laser source is one primary component of the setup. In our experiment we use one polarised and one non polarised Helium-Neon (He-Ne) laser (CVI Melles Griot, *part number 25-LHP-991-230*). The laser emits in the red (λ=633$\pm$1 nm) with an output power of 10 mW and works in the TEM_{00} (> 90 %) mode. The beam diameter ($1/e^2$) of the laser is 0.65 mm with a far field divergence of 1.24 mrad.

We also use a polarised green Diode-Pumped Solid State (DPSS) laser (CVI Melles Griot, *part number 85-GCA-020*). The DPSS laser is capable of delivering diffraction limited, TEM_{00} output with excellent power stability. Its emission wavelength is 532 ± 1.0 nm with an output power of 50 mW and has a beam diameter ($1/e^2$) of 1.1 ± 0.2 mm with a far field divergence of less than 1.25 mrad.

3.5.2 Ferroelectric liquid crystal spatial light modulator

The ferroelectric liquid crystal spatial light modulator (FLCSLM) is the other key component of the setup. As stated in the previous chapter, the device comprises a 2D array of cells each containing liquid crystal molecules that are in chiral smectic phase (denoted as smectic C^*). In our setup we use an FLCSLM (SXGA-R3) manufactured by Forth Dimension display. The display has 1280 x 1024 liquid crystal cells or pixels with a pixel pitch of 13.62 μm. It has an active area of 17.43 mm x 13.95 mm. The FLCSLM can display 24 bit color images (8 bits each for red, green, and blue) with a refresh rate of atleast 60 Hz. Thus SXGA-R3 is capable of displaying binary holograms at a rate of 1440 Hz (60 x 24). The exact display timing of each binary hologram can also be availed from the SXGA-R3 driver board in the form of a syc signal.

3.5.3 Photo detector array or camera

In this thesis work, we use two different types of CMOS cameras. We first use a USB 3.0 CMOS camera (Thorlabs, DCC3420M) that has a pixel resolution of 1280×1024 (1.3 megapixels) with a pixel pitch of 5.3 μm. It has a maximum full frame rate of 60 fps delivered via a USB 3.0 communication interface. This camera can be operated in both external triggered mode and free run mode. We also use a high-speed camera link CMOS camera (Basler, A504K). The pixel resolution of the camera is again 1280 $\times$1024 (1.3 megapixels) with a pixel size of 12.0 μm. It has a maximum full frame rate of 500 fps which can go even higher if lesser number of rows are activated. The camera can be triggered via an external synchronization signal or run in an internally controlled free-run mode.

3.5.4 Microcontroller Circuit and synchronization unit

In our experiments during image acquisition, the display in the FLCSLM panel and the camera exposure need to be synchronized. For this we have developed a synchronization unit using a peripheral interface controller (PIC) based circuit board (Microchip, PIC18F2550) which communicates with various other units. The FLCSLM provides a sync signal to the PIC18F2550 microcontroller as an external interrupt, indicating the display timings of a binary hologram sequence sent to the FLCSLM. The user code then instructs the microchip to process the sync signal and generate an appropriate trigger signal for the camera. This trigger signal then ensures that the camera captures the focal spots arising from a specific binary pattern displayed on the FLCSLM.

3.6 The experimental arrangement of a basic GAWS setup

To validate the working of the GAWS scheme, we perform a proof of principle experiment. The schematic diagram of the experimental arrangement is shown in Fig. 3.6. We use a He-Ne red laser as the illumination source whose specifications have already been discussed earlier. Two lenses L_1 and L_2 are used to expand and collimate the laser beam. The collimated beam is incident on the FLCSLM which can display an array of binary diffraction gratings or a single hologram computed in a LabVIEW program in a PC.

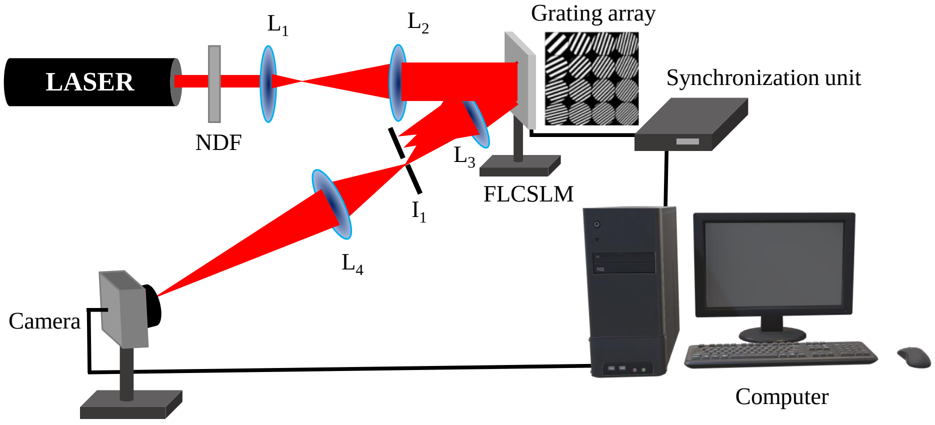

Fig. 3.6 Schematic of the experimental arrangement of a proof of principle grating array based zonal wavefront sensor setup.

The FLCSLM diffracts the incident beam into several orders and they are received by the lens L_3. An iris diaphragm is used to isolate the +1 diffraction order from the other higher orders. The +1 order beams are then focused using the lens L_4 on the Thorlabs USB 3.0 CMOS camera. The operations of the camera and FLCSLM are synchronized using the synchronized unit. The camera records the focal spot or a pattern of focal spots corresponding to a single hologram or an array of gratings. The Labview program in addition to computing the grating array or holograms communicates with the FLCSLM and the CMOS camera. The same program then converts the focal spot data into local slopes and estimates the unknown wavefront. The LabVIEW program also enables programmably changing the number of grating elements in the grating array. Besides the Labview program facilitates incorporating a linear combination of Zernike mode aberrations into the +1 order beam. The property of the +1 order beam gets modified in such a way as if the incident beam is aberrated with the same phase profile as the linear combination of Zernike modes. Therefore we refer such aberrations or phase profile as

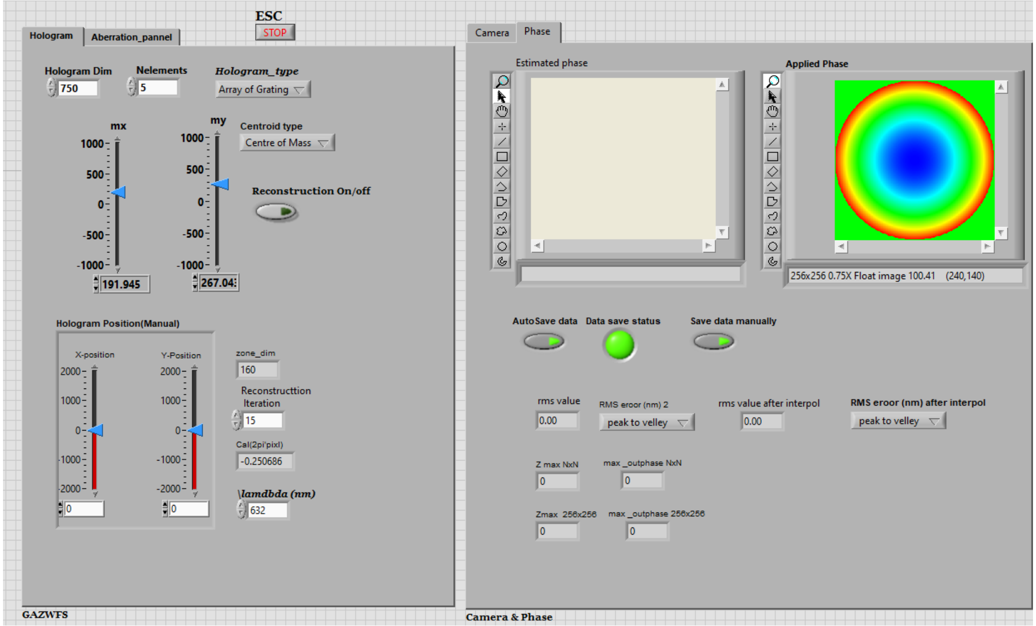

Hologram Dim 750
Nelements 5
Hologram_type Array of Grating
Centroid type Centre of Mass
mx 191.945
my 267.04
X-position 0
Y-Position 0
zone_dim 160
Reconstructtion Iteration 15
Cal(2pi'pixl) -0.250686
\lamdbda (nm) 632
256x256 0.75X Float image 100.41 (240,140)
rms value 0.00
RMS eroor (nm) 2 peak to velley
rms value after interpol 0.00
RMS eroor (nm) after interpol peak to velley
Z max NxN 0
max _outphase NxN 0
Zmax 256x256 0
max _outphase 256x256 0

Fig. 3.7 Screen shot of the front panel of the LabVIEW program for the GAWS.

holographically introduced aberrations or phase profile. Figure 3.7 shows a screen shot of the front panel of the Labview program.

3.6.1 Determination of calibration constant to estimate local slope

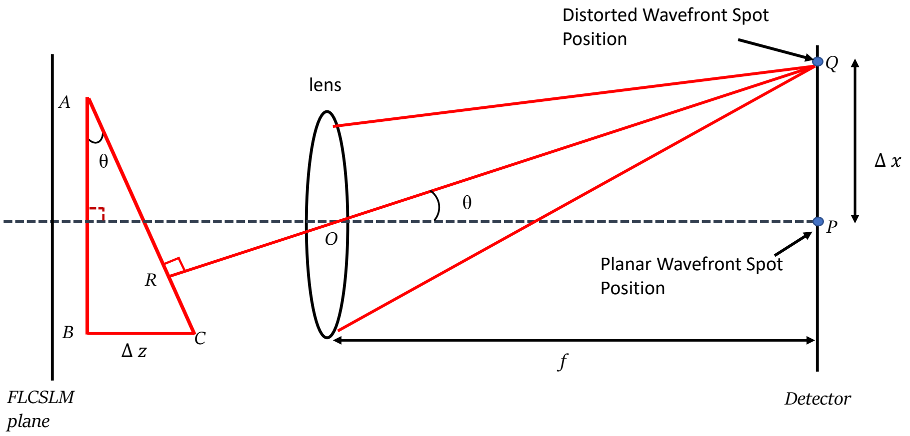

Fig. 3.8 Ray diagram showing the shift of the focal spot in the detector plane as a function of tilt of the wavefront in the FLCSLM plane.

As we have noticed, the camera in the GAWS estimates local slope of the test wavefront from the focal spot shifts. Figure 3.8 illustrates how change in slope in the wavefront leads to shift in focal spot. Let AB is the plane wavefront which is focused by a lens of focal length f at P. The normal to plane AB is along the optical axis. The respective tilted wavefront AC that makes an angle θ with the optical axis is focused at the point Q. Thus PQ is the focal spot shift for a wavefront slope of angle θ. If the camera plane coincides the focal plane of the lens and the wavefront AB or AC coincides with the FLCSLM plane then we can write

$$tan\theta = \frac{BC}{AB} = \frac{PQ}{OP} \tag{3.24}$$

such that

$$tan\theta = \frac{\Delta z}{d_{hol}} = \frac{\Delta x}{f} \tag{3.25}$$

Here d_{hol} is the beam or the hologram diameter, Δz is the path difference between the wavefront AB and AC at the edge of FLCSLM plane and the respective phase difference is $\Delta\phi$. Hence we can write

$$\Delta z = \frac{\lambda}{2\pi} \times \Delta\phi \tag{3.26}$$

Therefore knowing f and Δx the wavefront slope $\tan\theta$ can be obtained. However in the present setup there are more than one lenses between the FLCSLM and the camera plane. Hence the focal length f needs to be replaced by an effective focal length f_e that represents the effect of all the lenses between FLCSLM plane and the camera. Obtaining the exact value of f_e from the lens arrangement is difficult since it requires precise location of all the lenses and their focal lengths. Therefore we introduce a calibration constant (C_s) to estimate the slope whose value we determine holographically. We first display a single binary hologram of diameter d_{hol} using $\Phi = m_{x0}x + m_{y0}y$. The location of the +1 order beam in the camera say $(p_{x0},\ p_{y0})$ is noted. We then display another hologram using $\Phi_1 = (m_{x0} + \delta m_{x0})x + (m_{y0} + \delta m_{y0})y$ and the respective +1 order beam position $(p_{x1},\ p_{y1})$ is noted. The slope of the +1 order beam in the FLCSLM plane corresponding to Φ_1 is

$$\tan\theta = \frac{\lambda\sqrt{\delta m_{x0}^2 + \delta m_{y0}^2}}{d_{hol}} \tag{3.27}$$

We then define the calibration constant as

$$C_s = \frac{\lambda\sqrt{\delta m_{x0}^2 + \delta m_{y0}^2}}{d_{hol}\sqrt{(p_{x1} - p_{x0})^2 + (p_{x1} - p_{x0})^2}} \tag{3.28}$$

which can be expressed in the unit of radian per camera pixel.

Thus slope in X or Y direction can be obtained by multiplying the focal spot shifts in the camera plane in X or Y direction with C_s. For an array of $N \times N$ grating elements the corresponding calibration constant is given as C_s/N.

3.6.2 Correction of the reference beam

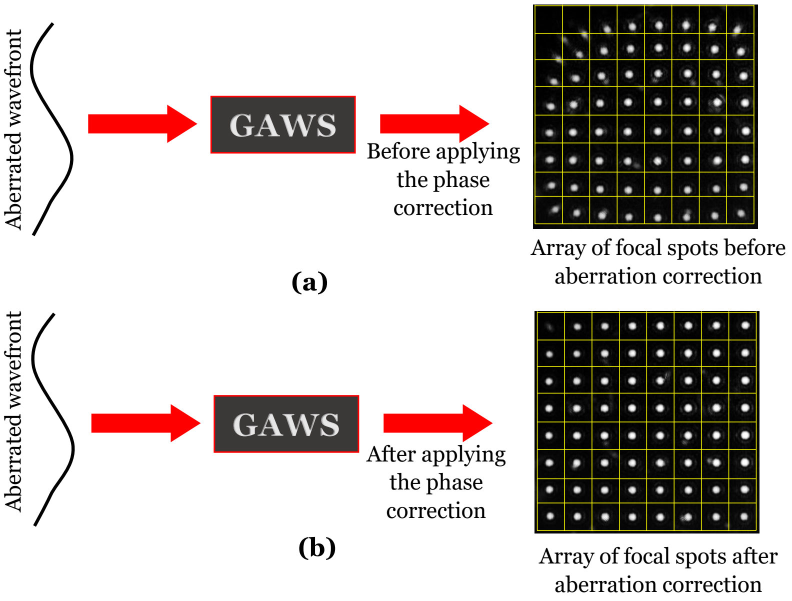

Fig. 3.9 Experimental images of the focal spot patterns (a) before correction of the reference beam and (b) after correction of the reference beam.

In our proposed GAWS setup the beam incident on the FLCSLM is first considered as the reference beam and resulting focal spot pattern of the same is recorded. We can then introduce a phase distorting element into the incident beam such as by transmitting the beam through an unknown glass slab or by reflecting it from a test surface. The incident beam carrying the unknown wavefront is then incident on the FLCSLM and resulting focal spot pattern is recorded. We notice that our reference beam is not perfectly plane which results in a focal spot pattern that deviates from a regular grid as seen in the experimental reference focal spot pattern in Fig. 3.9 (a). This may be due to the residual aberrations present in the incident beam and distortions introduced by the FLCSLM itself. We then incorporate a correcting phase into the incident beam holographically so that the reference focal spot pattern resembles a regular grid. The experimental focal spot pattern after aberration correction of the reference beam is seen in Fig. 3.9 (b).

3.7 Demonstration experiments using the basic GAWS setup

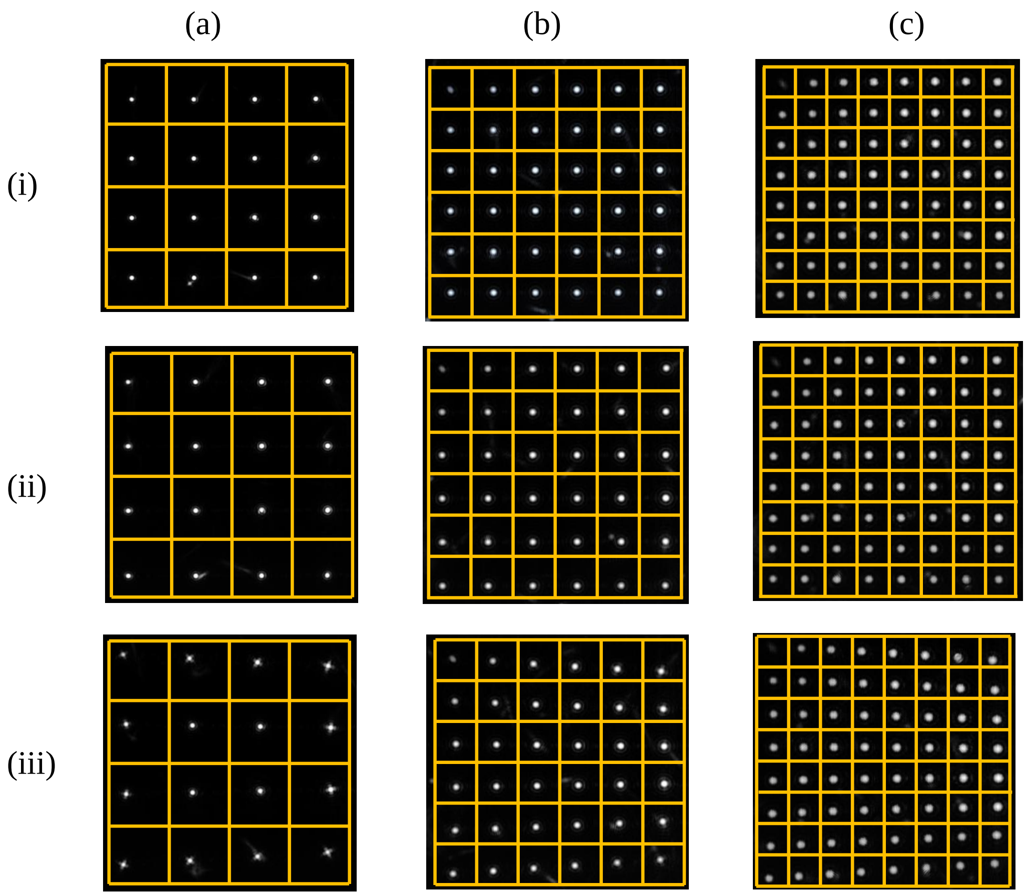

Fig. 3.10 Arrays of +1 order diffraction spots generated by grating array of dimension (a) 4×4, (b) 6×6 and (c) 8×8. Row (i) corresponds to the reference beam while rows (ii) and (iii) correspond to a holographically aberrated beam with defocus and trefoil.

We use the GAWS setup to estimate the wavefront of a holographically aberrated incident beam. Figure 3.10 (i) shows the reference +1 diffraction order focal spot pattern captured by the camera for grating array dimensions (a) 4×4, (b) 6×6 and (c) 8×8. We then incorporate 3 radian RMS (root mean square) amplitude of Zernike modes Z_4 representing defocus and Z_{10} representing trefoil into the incident beam holographically. Due to the aberration in the beam, the focal spot pattern gets displaced from their reference position and it is seen in Figs. 3.10 (ii) and (iii) (a), (b) and (c). The shifts in the focal spots relative to the reference focal spot positions are converted to the local slope values using Eq. 3.28. The slope data is then employed in the phase reconstruction algorithm to obtain the holographacially introduced wavefront.

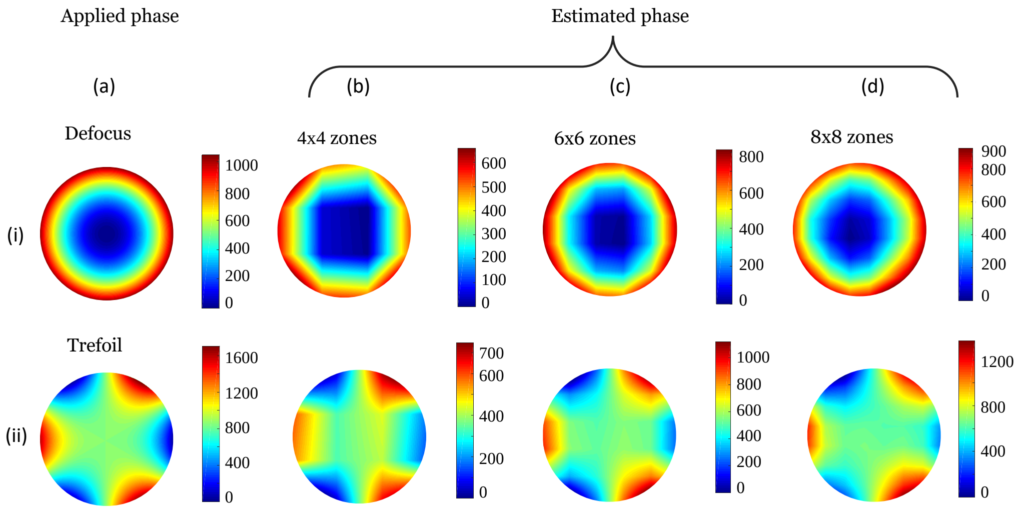

Fig. 3.11 False color images of the applied phase profile equal to 3 radian RMS of (i) (a) Z_4 and (ii) (a) Z_{10}. (b), (c), and (d) show the estimated phase profiles corresponding to (i) Z_4 and (ii) Z_{10} for grating array of dimension 4×4, 6×6 and 8×8, respectively. The colorbar is in nm.

The phase values of the incident wavefront are calculated from the measured local slope values using Eq. 3.19. Figure 3.11 shows false color images representing the applied (holographically introduced) and estimated phase profiles. For each applied phase profile seen in column (a) of Fig. 3.11 the respective estimated phase profiles using grating array dimensions of 4×4, 6×6 and 8×8 are seen in column (b), (c) and (d). The colorbar for each color image is in nanometer units obtained by multiplying the phase in radian with $\frac{633}{2\pi}$.

The line plots of the applied and estimated phase profiles along a line passing through the centre, for the grating array dimensions of 4×4, 6×6 and 8×8 are shown in Figs. 3.12 (i) and (ii). Here the red plot corresponds to the applied phase profiles while the

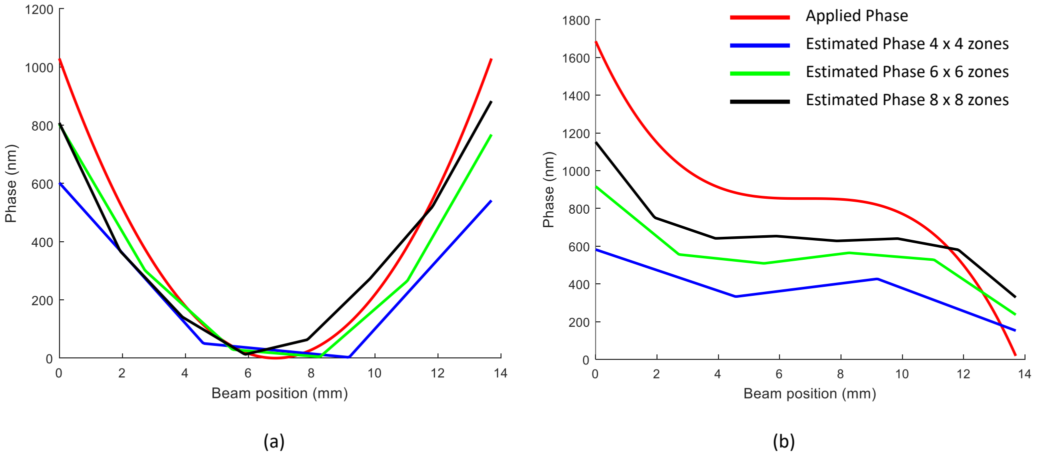

Fig. 3.12 Line plots along a line through the centre of the applied and estimated phase profiles for (i) defocus (Z_4) and (ii) trefoil(Z_{10}). The horizontal axis correspond to the sensor plane expressed in mm.

blue, green and black plots correspond to the estimated phase profiles for the grating array dimensions of 4×4, 6×6 and 8×8, respectively.

In the case of a holographically introduced phase profile, once the wavefront estimation is completed, it is possible to measure the accuracy of the reconstructed wavefront in terms of the difference between actual and estimated phase values. To quantify the difference in phase values, mostly root mean square error (RMSE) is considered. The RMSE in the estimated wavefront can be defined as

$$RMSE = \sqrt{\frac{\sum_{i=1}^{N^2} (\phi_i^a - \phi_i^e)}{N^2}} \tag{3.29}$$

where $\phi^a(x,y)$ and $\phi^e(x,y)$ are the applied and the estimated phase profiles respectively and N^2 is the total number of grid points where phase is estimated.

Here, we use the applied phase profile and the estimated phase profiles for various grating array dimension to calculate the RMSE for each case. Table 3.1 shows that

Table 3.1 RMS errors for different estimated phase profiles

Applied phase profile	Estimated phase profile		
	RMS Error for 4x4 grating array	RMS Error for 6x6 grating array	RMS Error for 8x8 grating array
3 Z_4	134 nm	108 nm	103 nm
3 Z_{10}	157 nm	122 nm	120 nm

RMS error in wavefront estimation for 3 radian RMS of defocus is found to be 134 nm, 108 nm, and 103 nm, when grating array dimensions 4 × 4, for 6 × 6, and for 8 × 8, respectively are used. The same RMS error in the case of trefoil aberration is found to be 157 nm, 122 nm, and 120 nm. It is thus observed that the RMS error values decrease with the increase in the dimension of the grating array. Thus the above proof of principle experiment successfully validates the working principle of the GAWS besides demonstrating other important capabilities such as aberration correction of the reference beam and programmable switching between number of sampling zones (i.e. grating array dimension).

3.8 Conclusion

In this chapter, we have first defined the wavefront and wavefront sensor. We have then described the principle of Shack-Hartmann wavefront sensor followed by a discussion on the wavefront estimation geometries and reconstruction algorithms. We have highlighted some important limitation of the Shack-Hartmann wavefront sensor. We have explained the principle of grating array based zonal wavefront sensor which uses a 2D array of binary diffraction gratings and showed how the sensor can address some of the limitations of the Shack-Hartmann wavefront sensor. We have provided a detailed description of the experimental arrangement of the proposed sensor that uses a ferroelectric liquid crystal spatial light modulator to realise the grating array in a dynamic fashion. We have performed proof of principle experiment to demonstrate the working of the grating array based zonal wavefront sensor and some of its novel features.

CHAPTER 4

In-situ surface profiling and thickness measurement using the GAWS integrated with the pulsed laser deposition system

4.1 Introduction

In the first chapter, it has already been emphasized on the requirement of on line monitoring of the growth and the thickness of the thin film particularly by deploying a diagnostic tool which is independent of the properties of the substrate as well as thin film under consideration. The present chapter demonstrates a novel method for in-situ on line monitoring of thickness and surface profile of thin film using a grating array based zonal wavefront sensor (GAWS) which is independent of the of the properties of the substrate and the thin film. The advantages of GAWS over SHWS has already been mentioned in chapters 1 and 3. The technique is implemented on a pulsed laser deposition (PLD) system. Therefore this chapter begins with the description of the PLD system on which the GAWS is implemented. It then describes the details of the experimental arrangement and important parameters of the setup. We also introduce the scheme that enables simultaneous measurement of thickness and surface profiles during the growth of the film on substrate as a function of time. The chapter ends with the results and discussion on the experimental validation.

4.2 Thin film fabrication using pulsed laser deposition system

Pulsed-laser deposition (PLD) is a physical vapour deposition technique to grow the thin film [84] of any material. PLD was developed after the invention of the pulsed ruby laser in 1960s [85, 86]. In 1965, Smith and Turner [87] successfully carried out thin film deposition onto multiple substrates for the very first time. But only after two decades, in the late 1980s, PLD received significant experimental development and popularity in scientific research. Since then, pulsed laser deposition is considered as versatile technique to deposit high-quality thin films [88]. It is capable of depositing high quality thin films of any dielectric material [89, 90], highly reflecting metallic thin films [91], conducting thin film [88], etc. Figure 4.1 shows the schematic of a pulsed laser deposition system. In this technique, a high-power pulsed laser is focused onto a target of the specific material whose thin film is to be deposited. When the intensity of the laser beam exceeds certain threshold, the material from the target in the focal region is ejected out in the form of atoms, ions, along with the liberated electrons and thus furnishes the plasma plume of the material of the target [89, 92, 93]. The plasma plume expands adiabatically, cools down, and deposites on the substrate placed slightly away from the target as shown in Fig. 4.1.

In the PLD technique, a small target is enough to grow large number of thin films thus offering an advantage over sputtering techniques where larger targets are required. The most important feature of PLD is its capability to transfer stoichiometry of the target material on deposited films and it is comparatively easier to fabricate the multi-layered films of different materials [91].

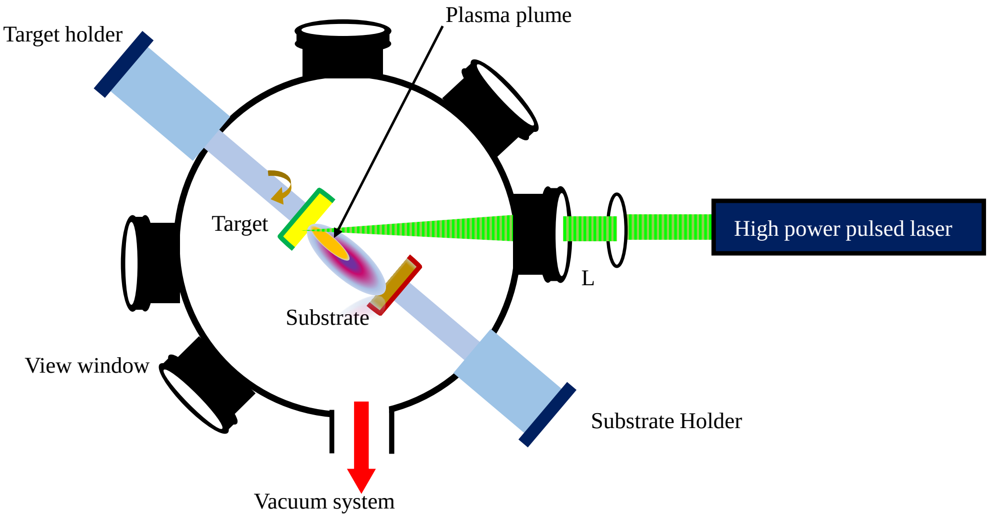

Fig. 4.1 Schematic of pulsed laser deposition system

4.3 Experimental arrangement for the pulsed laser deposition unit

A labelled photograph of the actual PLD unit used in the present thesis is shown in Fig. 4.2. It consists of an 18” diameter ultra-high vacuum deposition chamber made up of stainless steel (SS) (Make: Excel Instruments Mumbai, India). The SS chamber is equipped with a multitarget holder, substrate holder, and several viewports to focus the laser beam onto the target using a focusing lens as well as for mounting the various diagnostics. A pressure gauge is attached to the chamber through one of the ports to measure the background gas pressure inside the chamber. The ablation chamber is attached to a turbomolecular pump (*Pfeiffer, Hi Pace 700*) via a 100 CF gate valve through bottom 100 CF port and backed by a rotary pump (*GE Motors, F 144*) so as to evacuate the chamber.

The target holder stage of the PLD chamber is comprised of a microprocessor controlled carrousel capable of holding six targets simultaneously. It can be programmed

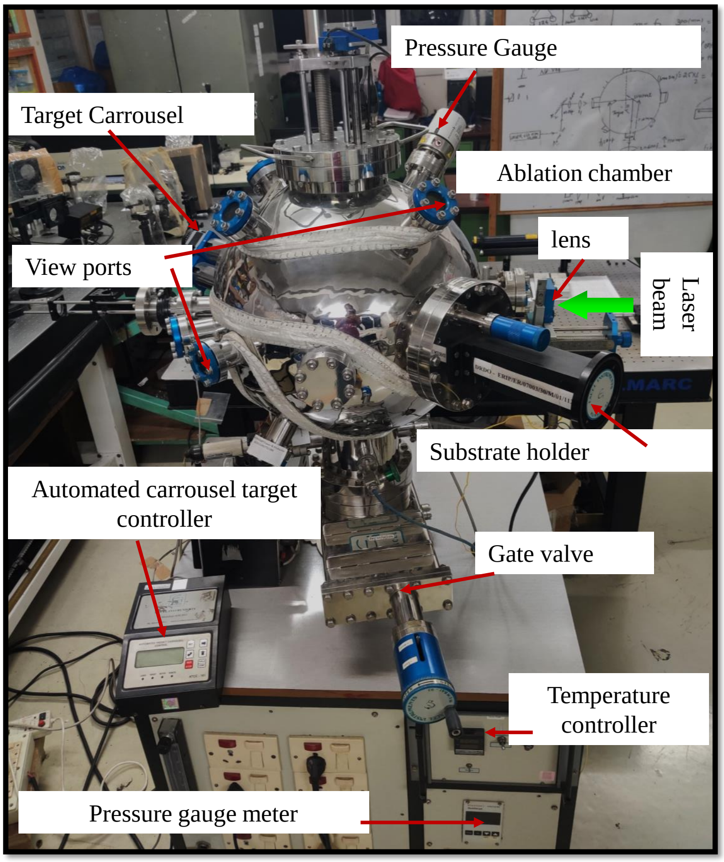

Fig. 4.2 A labeled photograph of the PLD unit.

to rotate the target about its own axis and also to rotate/raster about axis of the plate holding all the six targets. The carrousel is inserted inside the deposition chamber through one of the 150 CF port of the chamber as shown in Fig. 4.2. The substrate holder is positioned opposite to the target holder stage through another 150 CF port in such a way so that the laser induced plasma plume directly impinges onto it. The substrate holder is adjustable so as to tune the distance between the target and substrate. In the present experimental set up, the separation between the target and the substrate is maintained at 5 cm. The substrate holder is attached to a heater to control the temperature in a programable manner. The vacuum chamber is evacuated to a base pressure of around 10^{-6} mbar for several hours prior to the deposition. A compact full-range pressure gauge (*Pfeiffer, D 35614*) is attached through one of the ports as marked in Fig 4.2, to monitor the pressure inside the ablation chamber continuously during the deposition of the thin film. For deposition, the second harmonic of a Q-switched Nd-YAG laser (*Model No. INDI-HG*: wavelength - 532 nm, repetition rate - 10 Hz, pulse width $\sim$ 8 ns) is focused onto the target inside the ablation chamber using a plano-convex lens of focal length of 35 cm. The lens is mounted outside the chamber as shown in Fig. 4.2 and laser beam is made to incident through the corresponding view port marked as green arrow in the figure.

4.4 Surface profile measurement of thin film using the GAWS

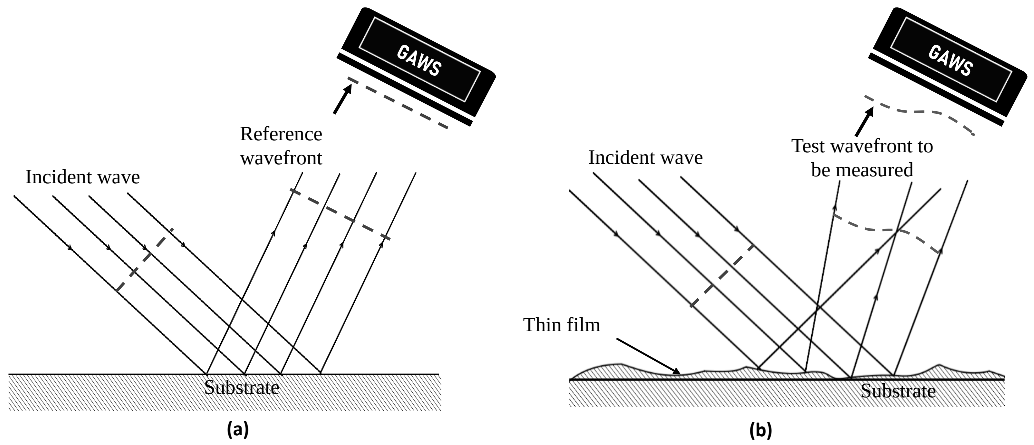

Fig. 4.3 Illustration of change in the wavefront shape of a beam reflected by a thin film surface.

In the previous chapter we have realised a grating array-based zonal wavefront sensor and demonstrated its working principle to measure arbitrary phase profiles of light beams. In case if the light beam is reflected from a thin film then its phase profile carries the information about the surface of the thin film. However to use such a wavefront as the test wavefront one also requires a reference wavefront. The ideal reference wavefront in such a case will be the wavefront of the same beam reflected by the bare substrate on which thin film is to be grown.

Figure 4.3 illustrates the basic principle of the surface profile measurement scheme of a thin film using the GAWS. Before deposition, a plane wave is incident on the substrate and reflected as the reference wavefront for the GAWS as shown in Fig. 4.3 (a). As the deposition begins, thin film grows on the substrate and the incident wave is now reflected by the thin film. Therefore, the shape of the reflected wavefront is now decided by the thickness profile of the deposited thin film. This reflected wavefront from the surface of the deposited thin film now acts as the test wavefront for the GAWS for which the reference wavefront is the reflected wave from the bare substrate. The GAWS estimates the test wavefront from the focal spots shifts relative to the reference wavefront using the phase reconstruction algorithm [56]. As discussed already, the GAWS works by locating the focal spot positions. So long as the focal spot intensity distribution has the minimum signal to noise ratio, locating the focal spot is to a large extent unaffected by the intensity fluctuations. Hence this scheme does not rely on any of the material properties of the thin film and the substrate so long as these are reflective.

4.5 Integration of the GAWS with the Pulsed Laser deposition unit

Figure 4.4 shows the experimental arrangement to integrate the grating array based zonal wavefront sensor with the pulsed laser deposition system. The working principle of the GAWS has already been described in chapter 3. The integrated system comprised of three segments, namely the probe laser beam delivery segment, the PLD setup followed by a lens to receive the beam reflected by the thin film, and the sensor segment of the GAWS. The beam delivery segment comprises a He - Ne laser (*Melles Griot model no. 05-LHP-991 power 10 mw*) whose output is first raised to the height of the PLD view port using a periscopic system. The laser beam is then expanded and collimated with the help of a microscope objective and lens L_1. The collimated laser beam is incident

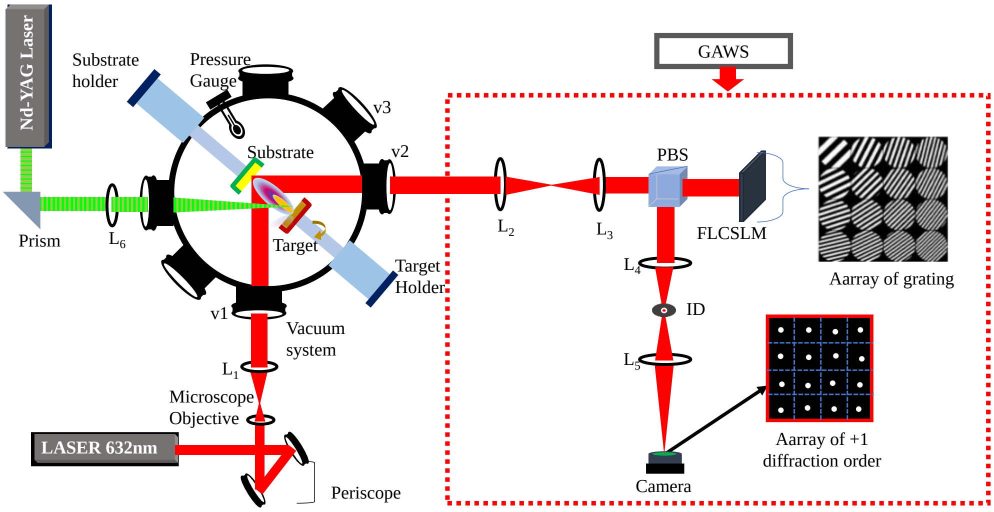

Fig. 4.4 Schematic of the GAWS integrated with the PLD system

onto the substrate inside the PLD chamber through the view port $v1$. The reflected beam from the substrate comes out through another view port $v2$, in a direction 90^o to the incident beam, and directed towards the FLCSLM. The PLD system and the sensor segment are connected optically via the lenses L_2 and L_3. The lenses L_2 and L_3 form a 4f relay to make the substrate and the FLCSLM optically conjugate to one another. Binary holograms or diffraction gratings are computed in a PC and are written onto the FLCSLM panel. The incident laser beam is made p polarised so that the reflected beam from the substrate is transmitted by the polarising beam spitter (PBS) to be incident on the FLCSLM. The diffracted light from the grating array is s polarised and hence is directed towards the detector plane by reflection from PBS. Lenses L_4 and L_5 via an iris diaphragm (ID) focus the diffracted beams on to the camera (Thorlabs USB 3.0). As stated already, for the GAWS, the reflected beam from the substrate only, acts as the reference beam while that of reflected from the film during deposition acts as the test beam of unknown wavefront.

In order to realise simultaneous in-situ real time measurement of both, thickness and surface profile successfully we need to overcome the issues of vibrational noise and the non uniform growth of the thin film. These are detailed in the following subsections.

4.5.1 Accounting for vibrational noise due to PLD system

Any relative vibrations of the integrated subsystem leads to unwanted beam fluctuations in the detector plane which gets reflected as inaccuracy or noise in the measured wavefront. The PLD chamber, as described in the section 4.3 is attached to the turbo molecular pump backed by rotary pump and hence during the operation, it is prone to introduce a large vibrations (relative to GAWS) for substrate and thin film deposited on it. This background vibrational noise is to be estimated and remedial corrections are to be incorporated for the accurate measurement of wavefront and hence the surface profiling of the thin film. As an example, Fig. 4.5 (i) shows the estimated wavefront when only the reference beam is incident, before switching the pump on at two different interval of time, (a) at $t = 0$ and $t = 30$ minutes, while Fig. 4.5 (ii) shows those of after switching the pump on. These clearly display a large slump in the wavefront estimation accuracy as the pump is swtiched on. Fortunately, majority of such vibrations effect the entire beam falling on all the sampling zones in a similar manner. Figure 4.6 (a) shows the initial focal spot pattern while Fig. 4.6 (b) shows the focal spot pattern after some time. It is noticed that the entire focal spot pattern gets shifted in a particular direction by nearly a fixed amount. This indicates that the effect of the relative vibrations due to vacuum pump is uniform in the entire beam over all the zones. To reduce the vibrations one can switch off the pumps once the chamber pressure attains a value of $\sim 10^{-6}$ mbar and then perform the deposition and online monitoring by GAWS. But due to the degassing, the pressure will build up in the chamber resulting in contamination of the film as well as target during the deposition. Therefore, in order to obtain good quality thin films, the chamber should be evacuated continuously during deposition of the pure metallic thin films e.g. Cu in the present case. Therefore, we come up with a novel scheme to mitigate the effect of vibrations.

Let us consider that the GAWS is having $N \times N$ number of sampling zones. X_{ref} and Y_{ref} are the x and y coordinates of the reference focal spot array recorded at $t = 0$.

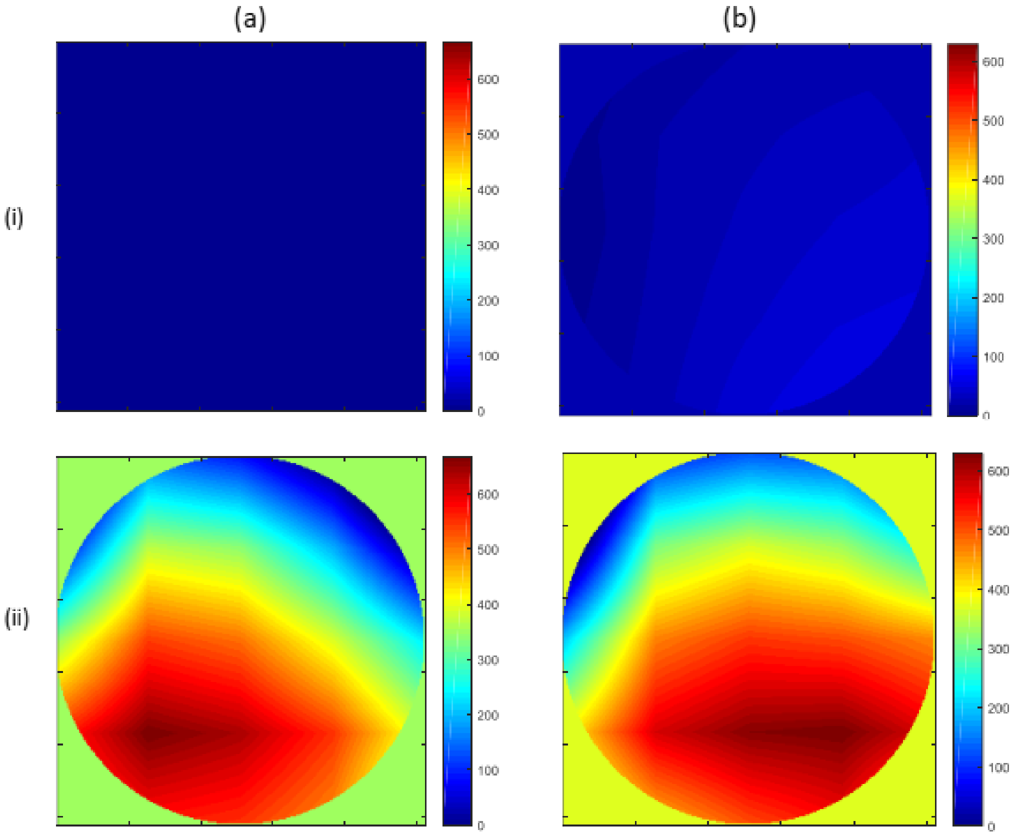

Fig. 4.5 Estimated wavefronts at (i) (a) $t = 0$ and (b) $t = 30$ minutes before the pump is on and (ii) after switching on the pump (a) $t = 0$ and (b) $t = 30$ minutes. Incident wavefront is the beam reflected by the substrate. The color bar is in nm.

Writing

$$X_{ref} = \begin{pmatrix} x_{11} & x_{12} & x_{13} & \dots x_{1N} \\ x_{21} & x_{22} & x_{23} & \dots x_{2N} \\ x_{31} & x_{32} & x_{33} & \dots x_{3N} \\ \vdots & \vdots & \vdots & \vdots \\ x_{N1} & x_{N2} & x_{N3} & \dots x_{NN} \end{pmatrix} \tag{4.1}$$

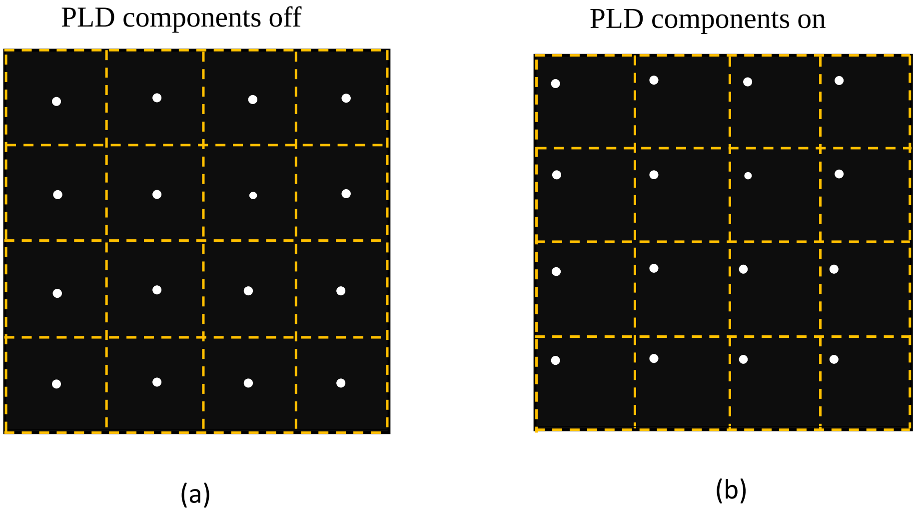

Fig. 4.6 Representative diagram of the focal spot pattern (a) before and (b) after the pump is switched on.

and

$$Y_{ref} = \begin{pmatrix} y_{11} & y_{12} & y_{13} & \dots y_{1N} \\ y_{21} & y_{22} & y_{23} & \dots y_{2N} \\ y_{31} & y_{32} & y_{33} & \dots y_{3N} \\ \vdots & \vdots & \vdots & \vdots \\ y_{N1} & y_{N2} & y_{N3} & \dots y_{NN} \end{pmatrix} \tag{4.2}$$

we then calculate the mean values of x and y coordinates as

$$\overline{x_{ref}} = \frac{\sum_{i,j=1}^{N} x_{i,j}}{N^2} \quad \text{and} \quad \overline{y_{ref}} = \frac{\sum_{i,j=1}^{N} y_{i,j}}{N^2} \tag{4.3}$$

As the pump is switched on the vibration of the setup increases. Let the displaced coordinates of the focal spot pattern at $t = t_o$ be

$$X'_{disp} = \begin{pmatrix} x'_{11} & x'_{12} & x'_{13} & \dots x'_{1N} \\ x'_{21} & x'_{22} & x'_{23} & \dots x'_{2N} \\ x'_{31} & x'_{32} & x'_{33} & \dots x'_{3N} \\ \vdots & \vdots & \vdots & \vdots \\ x'_{N1} & x'_{N2} & x'_{N3} & \dots x'_{NN} \end{pmatrix} \tag{4.4}$$

and

$$Y'_{disp} = \begin{pmatrix} y'_{11} & y'_{12} & y'_{13} & \dots y'_{1N} \\ y'_{21} & y'_{22} & y'_{23} & \dots y'_{2N} \\ y'_{31} & y'_{32} & y'_{33} & \dots y'_{3N} \\ \vdots & \vdots & \vdots & \vdots \\ y'_{N1} & y'_{N2} & y'_{N3} & \dots y'_{NN} \end{pmatrix} \tag{4.5}$$

The mean of respective x and y coordinates are calculated as

$$\overline{x_{disp}} = \frac{\sum_{i,j=1}^{N} x'_{i,j}}{N^2} \quad \text{and} \quad \overline{y_{disp}} = \frac{\sum_{i,j=1}^{N} y'_{i,j}}{N^2} \tag{4.6}$$

We then obtain the shift of the mean x and y coordinates relative to that of at $t = 0$ as

$$\Delta x = \overline{x_{disp}} - \overline{x_{ref}} \quad \text{and} \quad \Delta y = \overline{y_{disp}} - \overline{y_{ref}} \tag{4.7}$$

The x and y coordinates of the focal spot pattern at $t = t_o$ are modified as

$$X_{disp} = \begin{pmatrix} x'_{11} - \Delta x & x'_{12} - \Delta x & x'_{13} - \Delta x & \ldots x'_{1N} - \Delta x \\ x'_{21} - \Delta x & x'_{22} - \Delta x & x'_{23} - \Delta x & \ldots x'_{2N} - \Delta x \\ x'_{31} - \Delta x & x'_{32} - \Delta x & x'_{33} - \Delta x & \ldots x'_{3N} - \Delta x \\ \vdots & \vdots & \vdots & \vdots \\ x'_{N1} - \Delta x & x'_{N2} - \Delta x & x'_{N3} - \Delta x & \ldots x'_{NN} - \Delta x \end{pmatrix} \tag{4.8}$$

and

$$Y_{disp} = \begin{pmatrix} y'_{11} - \Delta y & y'_{12} - \Delta y & y'_{13} - \Delta y & \ldots y'_{1N} - \Delta y \\ y'_{21} - \Delta y & y'_{22} - \Delta y & y'_{23} - \Delta y & \ldots y'_{2N} - \Delta y \\ y'_{31} - \Delta y & y'_{32} - \Delta y & y'_{33} - \Delta y & \ldots y'_{3N} - \Delta y \\ \vdots & \vdots & \vdots & \vdots \\ y'_{N1} - \Delta y & y'_{N2} - \Delta y & y'_{N3} - \Delta y & \ldots y'_{NN} - \Delta y \end{pmatrix} \tag{4.9}$$

Therefore the focal spot shifts along x and y at $t = t_o$ become

$$X_{shift} = X_{ref} - X_{disp} \quad \text{and} \quad Y_{shift} = Y_{ref} - Y_{disp} \tag{4.10}$$

We employ the modified focal shifts as given by Eq. 4.10 in the phase reconstruction algorithm to get a wavefront measurement that is free from this vibration noise.

To verify the working of the proposed scheme we holographically introduce 1 radian RMS of defocus aberration into the incident beam. We then use our GAWS setup to estimate the wavefront at two instants of time, first at $t = 0$ when the pump is off and later at $t = 120$ min after the pump is switched on. Figures 4.7 (a) and (b) show the estimated phase profiles at time $t = 0$ and $t = 120$ min, respectively. The RMS error in the estimated phase which is 18 nm at $t = 0$ increases to 104 nm at $t = 120$ min. We then employ our scheme represented by Eq. 4.10 and estimate the wavefront at $t = 120$ min again which is shown in Fig. 4.7 (c). We observe that the RMS error now decreases to 20 nm which is very close to the error at $t = 0$.

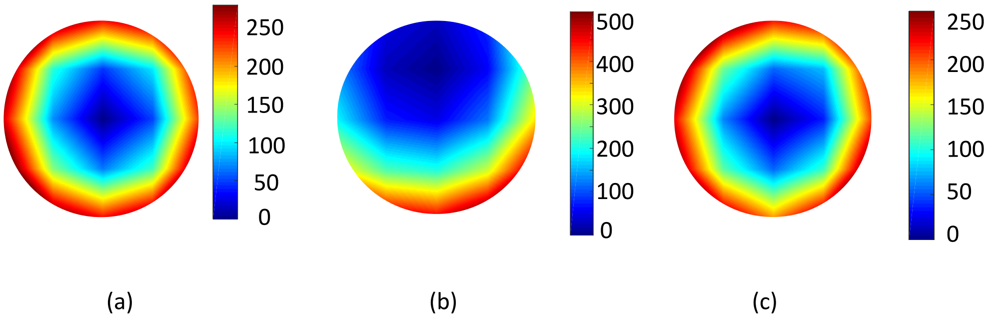

Fig. 4.7 (a) Applied phase profile, (b) estimated phase profile after 2 hours without applying the modified algorithm, (c) estimated phase profile after 2 hours obtained using the modified algorithm.

4.5.2 Determination of phase difference in the substrate plane (or thin film) from the measured phase difference in the sensor plane

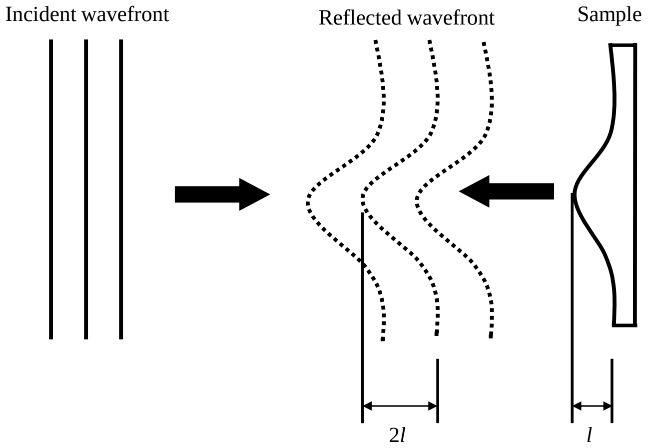

Fig. 4.8 Change in the phase difference on reflection due to non-uniform deposition of the thin films.

Let us consider that a plane wave is incident on a non uniformly deposited thin film where at the central part of the substrate the film has a maximum height equal to l

relative to the peripheral region as shown in Fig. 4.8. As a result, the reflected wavefront will not be planar and will undergo a peak path difference of $2l$. with respect to that of peripheral region. Therefore, the reflected wavefront after estimation is needed to be divided by a factor of 2 to get the phase difference in the substrate plane.

Besides as already mentioned in our setup, the substrate (in the PLD) and the FLC-SLM planes are made optically conjugate using the lenses L_2 and L_3. The beam size on the FLCSLM is 9.5 mm which on the substrate is 25 mm. Therefore, transverse magnification of the beam in this optical arrangement is 2.63. The transverse magnification is related to longitudinal magnification by the following relation,

Longitudinal magnifcation (M_L) = Transeverse magnification $(M_T)^2$

As we have $M_T = 2.63$, hence $M_L = 6.925$. Since the wavefront sensor measures the phase profile as incident on the FLCSLM plane, hence the actual phase profile of the beam in the substrate plane or sample plane is given as

$$\Phi_{Sample} = \frac{1}{2} \times M_L \times \Phi_{SLM} \tag{4.11}$$

where the factor $\frac{1}{2}$ on the RHS side is to count for the doubling of the phase difference due to reflection.

4.5.3 Scheme to measure the thickness and surface profile simultaneously

In our integrated system, we need to measure the thickness of the deposited thin film too apart from the surface profile by analysing the reflected wavefront. In the PLD system, normally the initial growth of the thin film in the central region is much faster compared to that of the peripheral (wing) region, thus giving a large gradient between the two (non uniform deposition). But with the passage of time, the growth towards the wings is picked up and therefore reducing the gradient and making the growth of thin film relatively less non uniform.

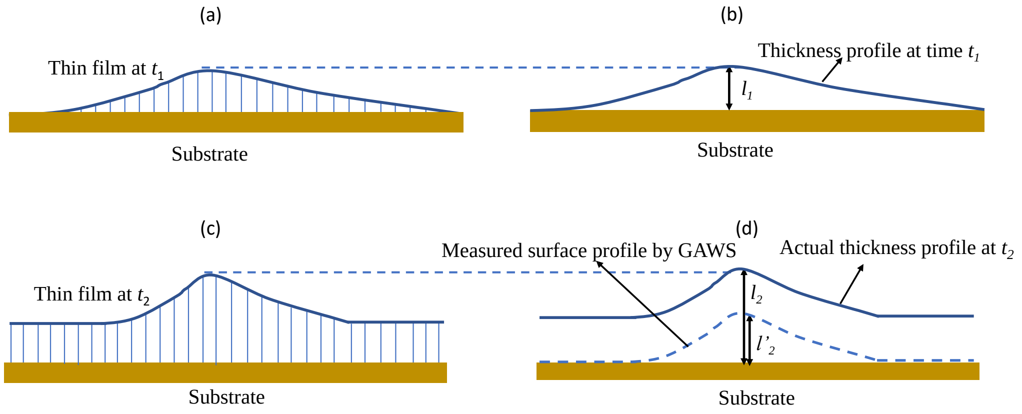

Fig. 4.9 (a) Thin films deposited at time $t = t_1$ and the (b) respective estimated surface profiles when there is negligible deposition in the peripheral area. (c) film deposition at $t = t_2$ and (d) corresponding the actual thickness profile and measured surface profile (broken line), when deposition taking place in the peripheral area.

The phase reconstruction algorithm of a zonal wavefront sensor is designed to provide phase of the reconstructed wavefront based on the zone wise local slope values. Thus it only provides the relative phase changes from one grid point to another or the surface profile. In our algorithm the minimum phase is always kept as zero. Therefore, if the reflecting surface is flat irrespective of its thickness, the phase estimation algorithm reconstructs a wavefront with zero phase values. If the thin film is deposited only in the central part, as during the initial period, the wavefront sensor will estimate both the surface and thickness profile accurately. But at later stages of deposition even though the surface profile estimation may be correct, it may not correspond to the correct thickness profile of thin film. This happens especially towards the later stage of the deposition as the peripheral deposition tends to flatten the thin film surface. Implication of this feature of the zonal phase reconstruction algorithm is further illustrated in Fig. 4.9 considering thin film deposition at two instants of time $t = t_1$ and $t = t_2$ where $(t_2 > t_1)$. At $t = t_1$, the growth is taking place only in the central part of the substrate whereas there is hardly any deposition towards the peripheral area of the substrate as shown in Fig. 4.9 (a). The phase reconstruction algorithm therefore provides correct height (l_1) of the thin film with respect to the substrate, since the minimum of the reconstructed phase profile occurring near the boundary matches with actual growth of the thin film at the peripheral region as shown in Fig. 4.9 (b). However if we consider the second case at $t = t_2$, where film also grows in the peripheral area as shown in Fig. 4.9 (c), the reconstruction algorithm although provides the correct surface profile but it does not represent the correct thickness profile. As seen in Fig. 4.9 (d) the surface height l_2' obtained from the reconstructed phase profile is smaller than the actual height l_2 of the thin film. However, this problem can be overcome by careful analysis of the phase profile recorded at regular interval of time during the deposition process as described below.

In our integrated system, the GAWS measures the surface profiles at an interval of 5 minutes. As discussed already, the film does not grow uniformly all over the substrate, at each instant of measurement. Considering the measurement at t=5 minutes, the estimated surface profile itself will also be the thickness profile. However at later instants as deposition starts taking place in the peripheral region the surface profile begins to deviate from the actual thickness profile. We assume that between two successive surface profile measurements there exists atleast one location on the substrate where deposition during the corresponding interval is nil or almost negligible. Since we have kept this interval as 5 minutes and measurement is taken over a large area of the substrate, this requirement seems realistic. Let us assume that during t=5 minutes to t=10 minutes, there is a certain location where no deposition has taken place. If the same location did not record any deposition during t=0 minutes to t=5 minutes, as well, then the estimated surface profile at t=10 minutes again will be the respective thickness profile. However if that location had some deposition previously, then in the surface profile estimated at t=10 minutes, the same location will have less surface height relative to that of estimated at t=5 minutes. Difference between the two then provides the thickness value to be added uniformly to the surface profile at t=10 minutes in order to transform it to respective thickness profile. If this process is repeated at every successive intervals than each surface profile can be transformed into respective thickness profiles.

Accordingly the steps to be followed to obtain both the surface and thickness profiles simultaneously can be formulated in the following manner. Let $\Phi_r(t_i)$ be the reconstructed phase or surface profile at $t = t_i$ with $t = t_0$ as the instant when the deposition is about to begin. $\Phi_t(t_i)$ is the respective thickness profile at $t = t_i$.

1. Define $\Phi_t(t_0)$=0.

2. At $t = t_i$ estimate $\Phi_r(t_i)$ using the reflected beam from the substrate at $t = t_0$ as the reference. Scale $\Phi_r(t_i)$ to make its minimum equal to zero.

3. Obtain $\Delta\Phi = \Phi_r(t_i) - \Phi_r(t_{i-1})$. If $\min(\Delta\Phi) < 0$ define $\Phi_t(t_i) = \Phi_r(t_i) - \min(\Delta\Phi)$, else keep $\Phi_t(t_i) = \Phi_r(t_i)$

4. Perform steps 2 and 3 for $i = 1$ to N, where N is the number of times the measurement is performed at regular intervals.

5. $\Phi_t(t_i)$ provides the thickness profile at $t = t_i$ and $\Phi_t(t_N)$ provides the thickness profile after the completion of the deposition.

The above algorithm provides an accurate estimation of the thickness profile under the approximation that in any interval between t_{i-1} and t_i, negligible deposition takes place at the grid point where the minimum of $\Phi_r(t_i) - \Phi_r(t_{i-1})$ occurs. Hence for better result using the algorithm the surface profile measurement interval is to be kept small and the beam should cover the entire deposition area.

4.6 Demonstration experiment to monitor the surface and thickness profile of the film during deposition

In this section, the measurement of the surface and thickness profiles as a function of time by the grating array based zonal wavefront sensor of film deposited on the PLD system is described. The GAWS is implemented during the deposition of Cu thin film under high vacuum environment at 500^oC substrate temperature via the PLD unit. The complete system is detailed in section 4.5 and depicted in Fig. 4.2.

4.6.1 Deposition of Cu thin film on the stainless steel (SS) substrate

Cu film is deposited on a well polished SS substrate of 50 mm diameter and 5 mm thickness. Prior to deposition substrate is cleaned by usual protocols; first it is sonicated in acetone for 30 minutes then it is rinsed with acetone and dried out naturally. The cleaned substrate is mounted on to the substrate holder stage with the help of two clips provided for this purpose. A pure Cu target of dimension $2.6\,cm \times 2.5\,cm \times 1\,mm$ is used as the target material. It is initially coarse polished by 800 dpi abrasive silicon carbide (SiC) paper for 90 minutes to remove the deep scratches and oxides layers on its surface. Then it is polished with 1000 dpi paper for nearly 60 minutes till the fine scratches are disappeared visually. The final cleaning process is performed the same way as that of substrate cleaning. After obtaining the metallic shining on the surface of the target, it is stuck to one of the target mounts using silver paste. The system is evacuated for several hours before initiating the deposition as detailed in section 4.3.

The film is deposited for a duration of 125 minutes under a high vacuum $\sim 10^{-5}\,mbar$. The substrate temperature through out the experiment is maintained at $500^{o}C$, and the laser energy is kept $52mJ$. The film is annealed at $500^{o}C$ for a duration of 120 minutes after the deposition and then allowed to cool down naturally under the vacuum.

4.6.2 Various GAWS parameters used in the experiment

We have used a GAWS comprising 5×5 grating elements or binary holograms. Each binary hologram is described by 140×140 FLCSLM pixels so that the net sensor area is described by 700×700 pixels. The binary holograms along with the tilts also contain a correction phase term to holographically correct the residual aberrations in the incident beam. The estimated phase profile over 5×5 grid points, that corresponds to a circular area of diameter $\sim$ 20 mm in the substrate plane, is expanded to 512×512 pixels using bilinear interpolation. Calibration constant (C_s) (as described in chapter 3, section 3.6.1) for the experiment has been calculated to be 0.24 radian per camera pixel.

4.6.3 Results and discussion

As stated already the surface profile measurement of the thin film is performed at an regular interval of 5 minutes for 125 minutes. For each measurement, the focal spot array coordinates are corrected for mechanical vibrations and noise using Eq. 4.10. Each surface profile is then converted to respective thickness profile by adopting the scheme stated in section 4.5.3. All the surface and thickness profiles are expressed in the substrate plane in nm units . Figures 4.10 (a→f) show 2D plots of the thickness profiles at t = 20, 40, 60, 80, 100, and 125 minutes, respectively.

Table 4.1 In-situ thickness measurement of thin film during the deposition of thin film using the GAWS

Time (min)	Thickness of the thin film ± 20 nm measured by GAWS	Time (min)	Thickness of the thin film ± 20 nm measured by GAWS
5	175	70	1520
10	197	75	1584
15	248	80	1636
20	292	85	1643
25	389	90	1725
30	392	95	1798
35	460	100	1858
40	727	105	1879
45	869	110	1903
50	1004	115	1921
55	1090	120	1974
60	1316	125	1990
65	1335	- -	- -

Table 4.1 on the other hand lists the thickness value at the centre of the substrate after every 5 minutes for the entire duration of deposition (equal to 125 minutes). Figure 4.11 (a) shows the thickness at the centre of the substrate with respect to time without employing the correction scheme for surface to thickness profile (section 4.5.3). Decrease in surface height from t=100 minutes onwards can be noticed, indicating that the surface height is not same as film thickness. Figure 4.11 (b) shows the film thickness at the same

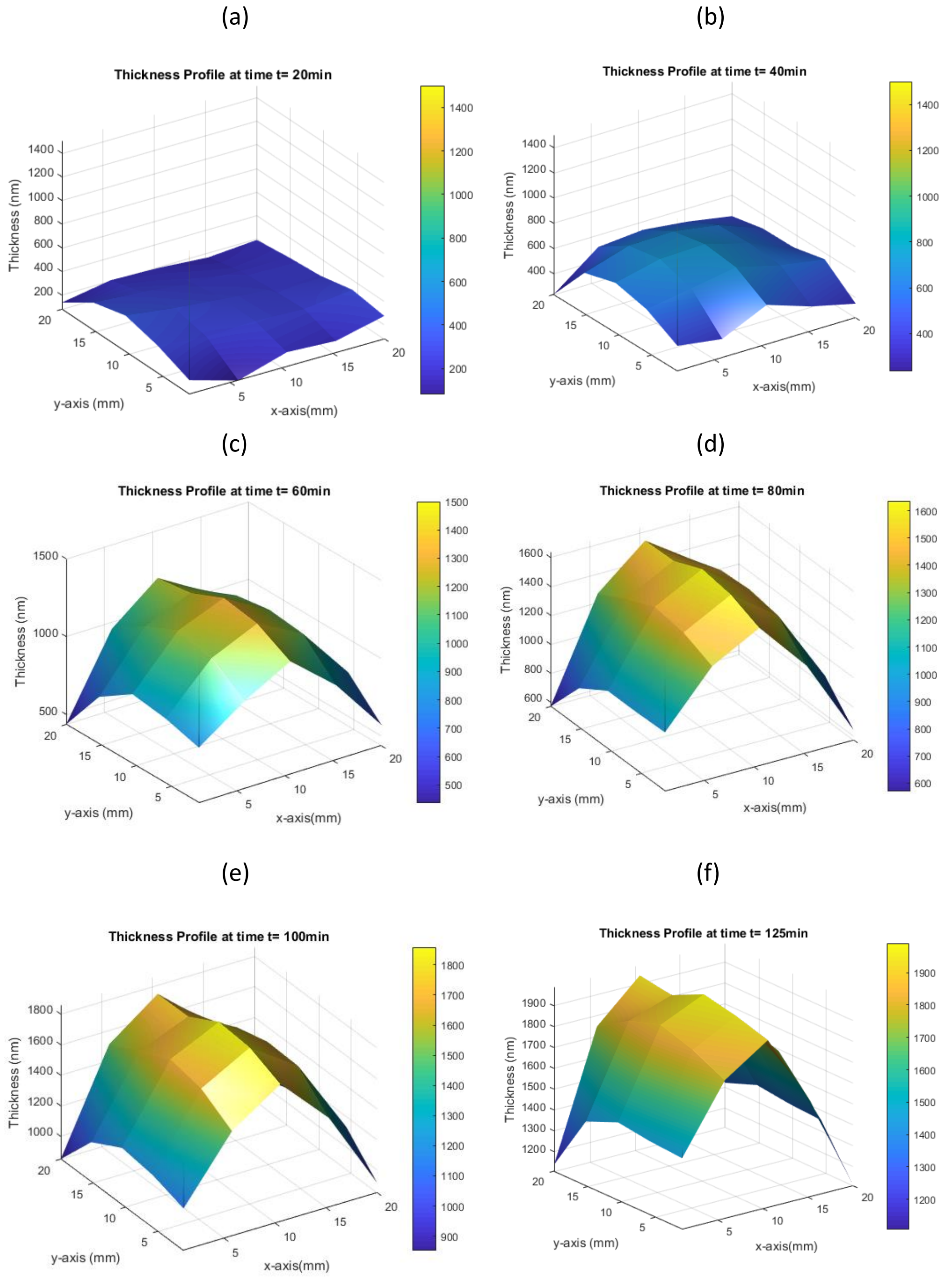

Fig. 4.10 Thickness profiles in nm as estimated by the GAWS at (a) time t= 20 min, (b) time t = 40 min, (c) time t= 60 min, (d) time t= 80 min, (e) time t= 100 min and (f) time t= 125 min.

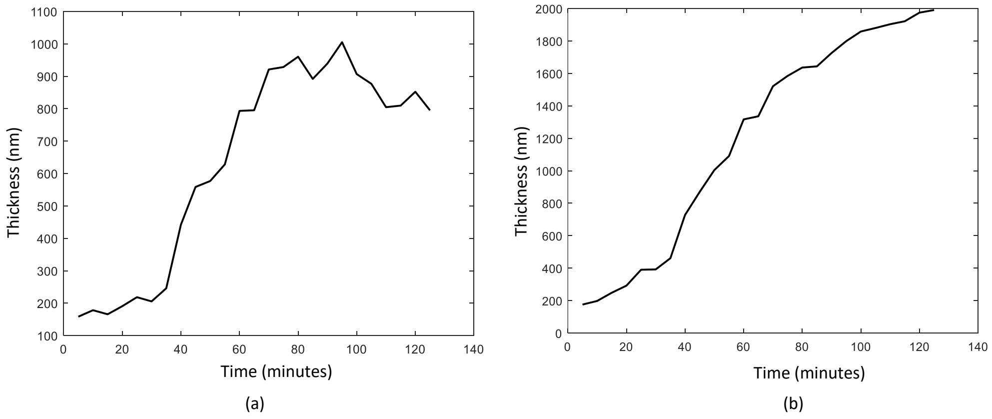

Fig. 4.11 Plots of the thickness vs time at the centre of the substrate (a) without employing the proposed thickness measurement scheme (b) after employing the proposed scheme to measure the thickness.

location, obtained after implementing the surface profile to thickness profile conversion scheme as described in section 4.5.3. Thus, if the estimated surface profiles are not converted into thickness profiles, then the conventional algorithm can not estimate the thickness of the film accurately. The thin film after it is taken out of the PLD system

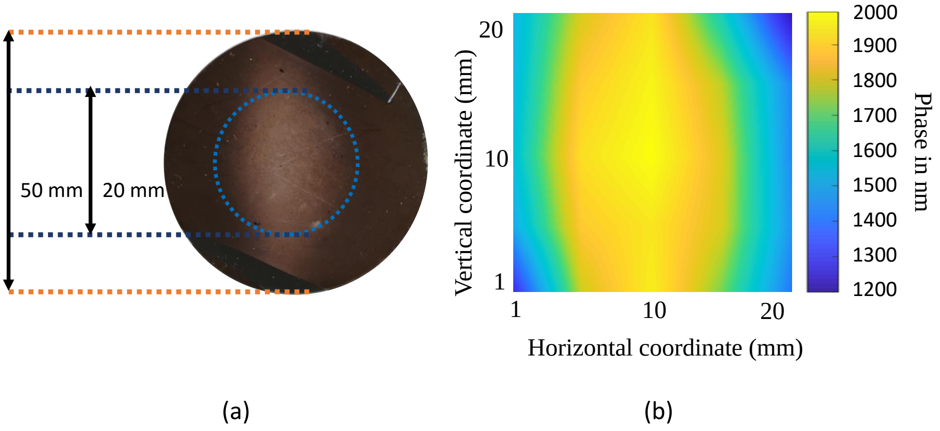

Fig. 4.12 (a) Color image of the final Cu thin film deposited. Measurement is performed over the dashed circular area. (b) False color image of the thickness profile of the final film as given by the GAWS.

is photographed using a colored camera and is shown in Fig. 4.12 (a). The false color image of the respective thickness profile as given by our scheme is shown in Fig. 4.12 (b). A careful look at the two figures clearly reveal the visual similarity confirming the validity of the present measurement.

Post deposition film thickness measurement by stylus profilometer

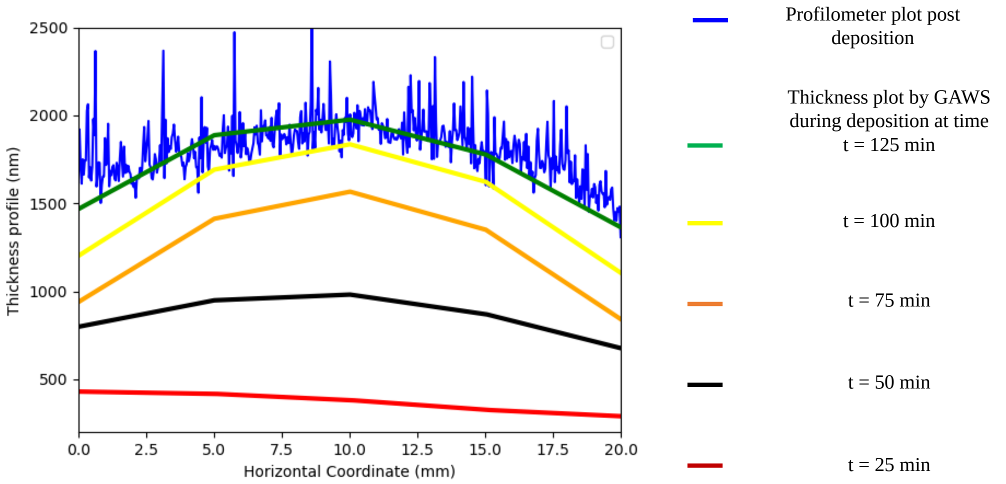

Fig. 4.13 Comparison of thickness plots of the thin film measured by GAWS and stylus profilometry, in the central region along the horizontal direction after completion of deposition. The thickness profile during the deposition at time $t = 25, 50, 75, 100, 125$ minutes are also shown.

After completion of deposition and cooling, film is taken out of the PLD chamber and thickness of the film is measured by a stylus profilometer (Dektak 150 manufactured by Veeco) separately in order to compare the measurement by the GAWS setup. Stylus profilometry is a contact mode technique where the stylus moves vertically and laterally to scan the surface of the sample and measures the surface height profile as a function of position.

The profilometer is very sensitive to the height variation in the sample. In order to measure the thickness of the film from the surface of the substrate, a mask is to be placed on the substrate during the deposition so as to build a step between the film and the bare substrate (i.e. devoid of deposition). This type of steps are created naturally in the present case by the clips holding the substrate, acting as mask thereby prohibiting deposition in the masked region. Figure 4.13 shows line plot of thickness as given by the profilometer (along a horizontal line through the centre of the film shown in Fig. 4.12 (a) and the respective line plot of the thickness at t=125 minutes as obtained by the GAWS measurement. It is observed that the two thickness plots agree reasonably well. The average thickness in the central region is found to be 1925 nm as measured by the stylus profilometer. The same figures also shows the thickness plots along the same line from the GAWS at different instants of time t = 25 min, 50 min, 75 min, and 100 min during deposition.

4.7 Conclusion

In this chapter, successful implementation of GAWS to monitor the growth of the Cu thin film during the deposition via PLD is demonstrated. Initially, a brief description of various components of the pulse laser deposition unit employed in the present work has been provided. We have then integrated the grating array based wavefront sensor with the PLD system for in-situ measurement of surface and thickness profiles simultaneously during deposition. We have discussed the various design consideration of the integrated system and the challenges that we had to overcome to implement the proof of principle experiment. The chapter ends with the illustration of the experimental results validating the technology of in-situ surface profile and thickness measurement simultaneously of thin film during the deposition by GAWS. Finally, the results are compared with the offline measurement via a commercial stylus profilometer and both the results are in reasonable agreement.

CHAPTER 5

Development of zonal wavefront sensors with enhanced dynamic range and enhanced sensitivity

---

5.1 Introduction

In the previous chapter, the implementation of a novel grating array based zonal wavefront sensor to measure the surface profile and thickness of thin film during deposition has been demonstrated. Such a scheme will be useful for the majority of the thin films having some surface curvature or gradient rather than perfect flatness. However, for thin film of extremely high flatness or large curvatures, the above scheme is to be modified suitably. In this chapter, we introduce another two schemes to measure the surface profile with enhanced sensitivity and dynamic range. We also present experimental results to demonstrate the performance of the two proposed schemes.

5.2 Sensitivity and dynamic range of a zonal wavefront sensor

Sensitivity and dynamic range are two most important parameters of a zonal wavefront sensor. Sensitivity describes the smallest local wavefront slope in the sensor plane that can be measured by the wavefront sensor. On the other hand, dynamic range is the maximum local slope detectable using the wavefront sensor. Figure 5.1 shows focusing of a local wavefront by a single lenslet of the wavefront sensor. For the local wavefront slope having an angle θ with respect to the plane perpendicular to the optical axis, the focal spot shifts by an amount $\Delta x = f \tan\theta$ with respect to the reference position P. Here, f is the focal length of the lenslet and the detector array is assumed to be placed at the focal plane of the lenslet. As we can see that the minimum wavefront slope measurable

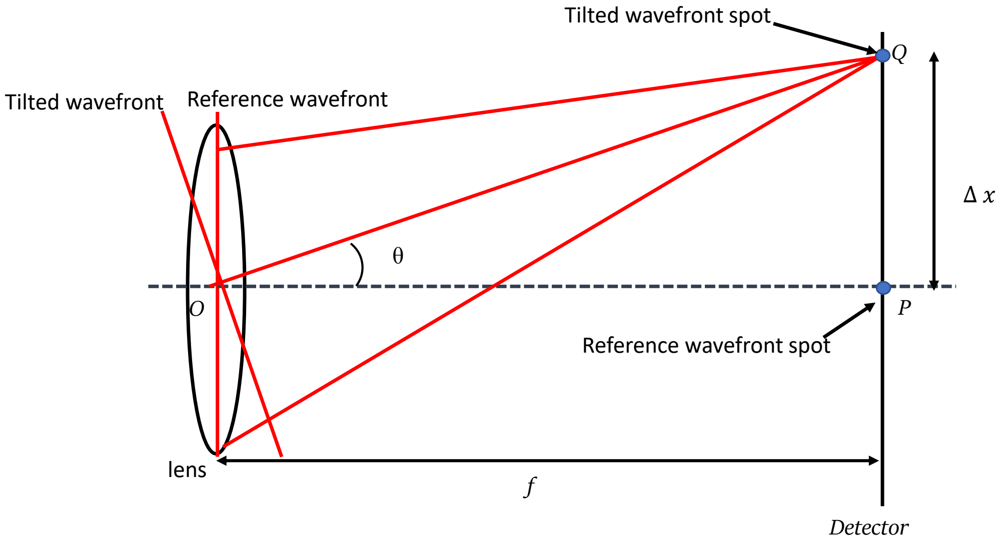

Fig. 5.1 The focal spot displacement in the detector plane for a given wavefront incident on the lens.

by the sensor is determined by the minimum detectable shift of the focal spot by the detector and hence it is the pixel pitch of the detector array that effectively decides the sensitivity. Therefore, denoting the sensitivity (per pixel) as θ_{min} and under small angle approximation,

$$\theta_{min} = \frac{\text{pixel pitch}}{f} \tag{5.1}$$

The unit of θ_{min} is radian per pixel. In a similar manner, the maximum local slope in the sensor plane is decided by the dimension or number of pixels in the detector subaperture for the given lenslet. Hence, if d_{max} is the dimension of the subaperture then the dynamic range of the sensor from Fig. 5.1 is given by

$$\theta_{max} = \frac{d_{max}}{2f} \tag{5.2}$$

where θ_{max} is in the unit of radian.

Sensitivity of the wavefront sensor will play an essential role in surface profile and thickness measurements particularly in applications requiring uniform thickness or flat surfaces. Thickness uniformity is important in a number of applications involving various types of thin films such as solar cell [94, 95], plane mirror band pass filters [96] etc. Since uniform growth of thin film in any deposition system is not guaranteed hence a sensitive thickness profile monitoring system during deposition can be very useful. On the other hand, there are a number of applications involving sinusoidal or non sinusoidal periodic thin films structures. For instance, quasi periodic thin film structure can improve antireflection properties [97], and can be useful in energy storage application [98]. Sinusoidal thickness variation is on the other hand also relevant for the fabrication of thin film waveguide [99]. Such periodic thin film structure will certainly be associated with extremely high slope of the surface. Therefore, for all such applications the sensitivity and the dynamic range of the proposed scheme need to be improved.

From the Fig. 5.1, it is seen that the sensitivity of a Shack-Hartmann type wavefront sensor can be increased in principle by increasing the focal length of the lenslet. Similarly, the dynamic range of a Shack-Hartmann type wavefront sensor can be increased by decreasing the focal length of the lenslet. Unfortunately, the lenslet array has a fixed focal length and hence one has to be contained with the given sensitivity and dynamic range of the sensor. Nevertheless, several attempts have been made to increase the sensitivity of a zonal wavefront sensor, for instance by using algorithms to measure subpixel focal spot shifts [100], noise reduction in the focal spot data [101], placing a detector in a defocused plane and employing a modified estimation algorithm [102], etc. Attempts have also been made to increase the dynamic range of the zonal wavefront sensor by blocking and unblocking the individual lenslets [103, 104], by sequential projection of small portions of the wavefront at a time [105], apodisation of the fabricated lenslets array [106] and using astigmatic microlenses [82]. However, most of such improvements are not applicable for the in-situ measurement of surface profile and thickness of thin film during the deposition as is possible in our present system in chapter 4. In our proposed scheme, it is possible to change the focal length of the focusing lens that follows the grating array, easily. For instance we can use a lens of larger focal length to enhance the sensitivity of the sensor [107]. However, increase in focal length will lead to increase in the size of all the focal spots which in turn will limit the dynamic range of the sensor. Using a scanning type Hartmann sensor [108] it is possible to utilize the entire detector array for each focal spot. However, one has to pay a price in terms of the sensing frame rate. In the following sections, we propose two novel schemes, one to enhance the sensitivity of our proposed wavefront sensing schemes without compromising on the sensing speed and the other to enhance the dynamic range of the sensor significantly for highly curved thin film surfaces.

5.3 Sensitivity Enhancement in a zonal wavefront sensor

In order to improve the sensitivity of our zonal wavefront sensor, we modify the sensing scheme utilizing the capability of the FLCSLM display. In the previous two chapters, we implemented grating array based zonal wavefront sensor where the entire focal spot array corresponding to all the sampling zones were recorded simultaneously. However, in the proposed scheme to enhance the sensitivity, we use sequential display of binary patterns to activate one sampling zone at a time. Thereby, we are able to describe the focal spot of each sampling zone by using the entire camera plane and without significantly compromising on the sensing speed. The working principle of the proposed scheme is detailed below.

5.3.1 Working Principle of sensitivity enhanced zonal wavefront sensor (SEZWS)

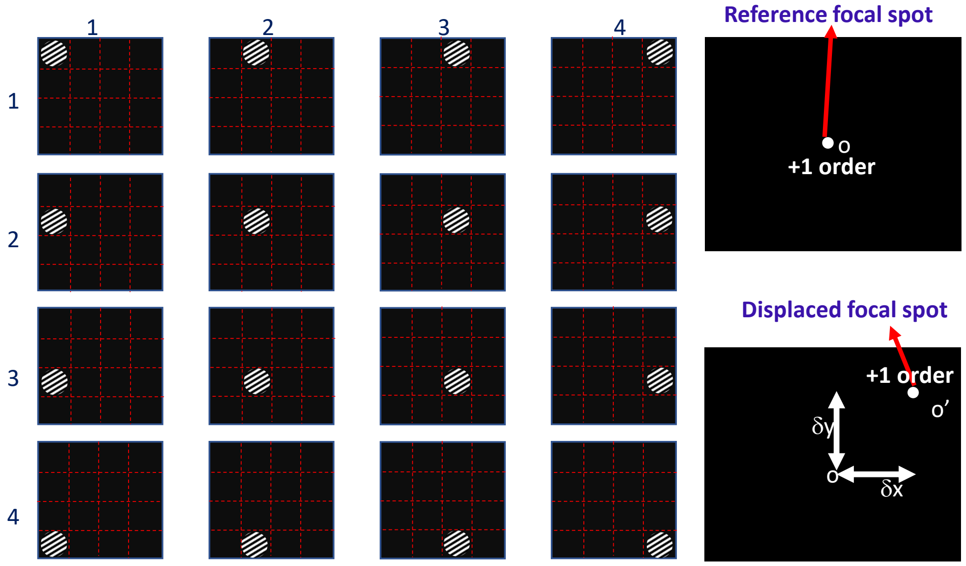

Fig. 5.2 4 × 4 binary patterns to be displayed sequentially on the FLCSLM panel for zone wise scanning of the incident wavefront. As seen in the right panel, the +1 order focus spot for the reference wavefront is located at the centre of the detector plane and the same gets displaced from its reference position for an aberrated wavefront.

In order to explain the working of the proposed sensitivity enhancement scheme, we divide the FLCSLM plane, acting as the sensor plane, into $N \times N$ sampling zones. A binary hologram is constructed in one sampling zone while keeping the rest of the FLCSLM pixels as zero. If a beam is incident on such an FLCSLM panel +1 order diffracted beam will be generated by the binary hologram of the given zone. The tilt values of the binary hologram can be selected in such a way that the +1 order focal spot falls at the centre of the camera plane for the reference beam incident on the FLCSLM. Such a binary pattern comprising of a binary hologram in one sampling zone only can constitute a single bit plane of a 24 bit color image. We can construct similar binary pattern with the binary hologram defined in another zone. If this binary hologram uses the same set of tilt values as the earlier one then in this case also +1 order beam will fall at the centre of the camera plane for the incident reference beam. Figure 5.2 shows 4×4 such binary patterns with the FLCSLM plane divided into equal number of sampling zones. Since each binary pattern is represented by a single bit plane of the 24 bit image, hence to represent $N \times N$ such binary patterns it will require $\frac{N^2}{24}$ number of color images. As the FLCSLM can display 60 numbers of 24 bit images in one second it will display the binary pattern at a rate of 1440 Hz. Therefore, if the camera captures the +1 order focal spot from each zone at a frame rate of at least 1440 Hz then one can record all the +1 order focal spots immediately after the display of the $N \times N$ binary patterns. As seen in Fig. 5.2 each reference focal spot is located at the centre of the camera plane while the focal spots corresponding to test wavefront can be located anywhere in the camera plane. Therefore, even if the +1 order focal spot is relatively large it can be still located within the camera plane without any possibility of crosstalk with nearby zones. Thus, it is now possible to use a longer distance between the camera and the focusing lens following the FLCSLM plane. The longer distance between the lens and the camera enhances the sensitivity of the sensor. In order to keep the sensing speed at 60 Hz, the number of zones is kept as 24. Since the incident beam is expected to have a circular cross section hence if we describe 24 binary holograms in as many sampling zones as shown in the Fig. 5.3 (i), we will be able to sample almost the entire beam cross section using just one color image.

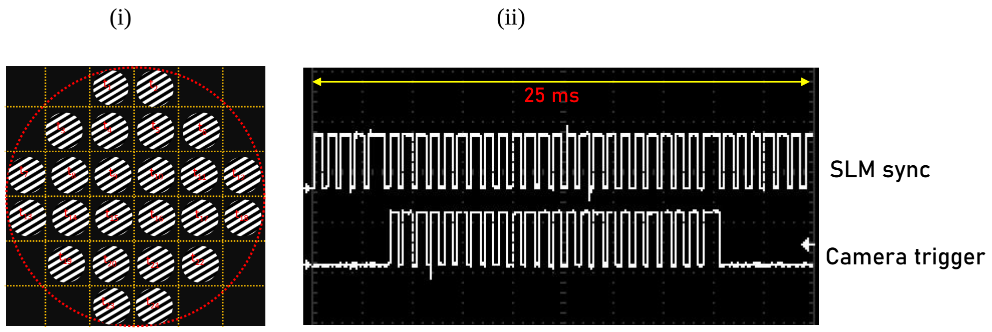

Fig. 5.3 (i) Cumulative 24 binary holograms to be displayed sequentially via a single 24 bit color image, (ii) Binary pattern display timing denoted as SLM sync provided by the FLCSLM and the camera trigger for the capture of 24 sequentially displayed binary patterns as provided by the microprocessor based synchronization unit.

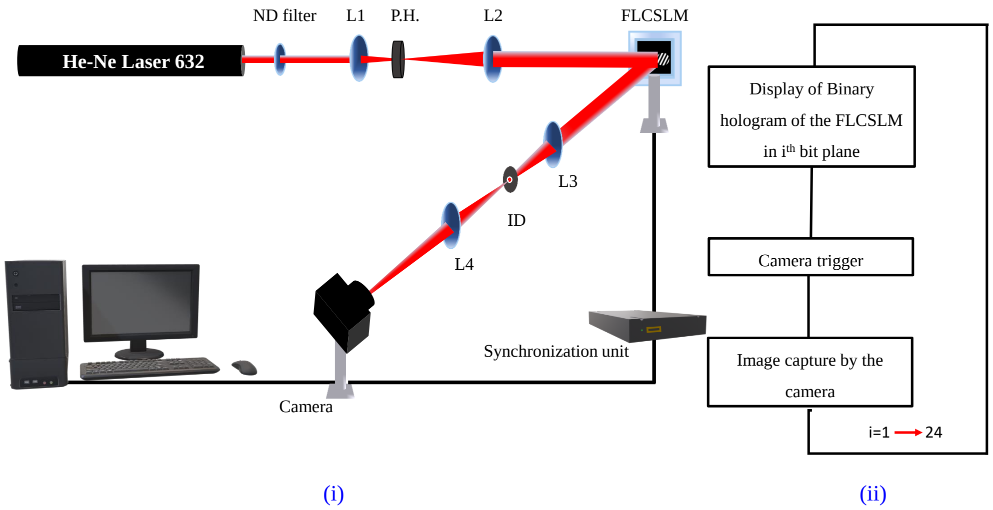

Fig. 5.4 Schematic of (i) experimental setup for SEZWS, (ii) the sequence of steps for synchronised display of binary holograms followed by acquisition by the camera.

5.3.2 Experimental arrangement for SEZWS

The experimental set up to demonstrate the proof of principle experiment is shown in Fig. 5.4 (i). Other than the zonewise sequential display of binary holograms, the setup is very much similar to the basic GAWS setup shown in chapter 3. Here, we use a He-Ne laser emitting at 633 nm as the source and use a pin hole PH as the spatial filter to cut down the higher order of spatial frequencies. A 24 bit color image constituted by 24 number binary patterns with each pattern comprising of single binary hologram in a given sampling zone is created by the PC which is then sent to the FLCSLM display. We use a Baser A504K camera and reduce its active sensor area to 340 × 340 pixels so that the acquisition rate is about 1.5 kHz. The raw synchronization signal from the FLCSLM is converted to a trigger signal to capture 24 image frames corresponding to each of the 24 sampling zones. Snap shot of the oscilloscope screen displaying the FLCSLM sync signal and the camera trigger is shown in Fig. 5.3 (ii). The process of the sequential display of each binary pattern followed by the capture of the corresponding +1 order focal spot for all the 24 bit planes is illustrated in Fig. 5.4 (ii). The record of the focal spot images corresponding to the test wavefront relative to the reference wavefront is used to calculate the focal spot shifts which is then applied in the phase reconstruction algorithm for the estimation of the test wavefront. The distance between the lens L4 and the camera (referred to as image distance) can be adjusted suitably to increase or decrease the sensitivity. We operate the present system using two different distances of 121 mm and 1300 mm. The sensitivity of the present system for 121 mm and 1300 mm image distances are found to be 52 μ radian/camera pixel and 3 μ radian/camera pixel, respectively. Thus the sensitivity of the sensor is enhanced more than 17 times using the image distance of 1300 mm relative to the configuration of image distance equal to 121 mm. We call the configuration with image distance equal to 121 mm as the low sensitivity configuration while the configuration with image distance equal to 1300 mm as the high sensitivity configuration.

5.3.3 Results and discussion on experiments with the SEZWS

The tilt in each of the 24 binary holograms as shown in Fig. 5.3 (i) is adjusted in such a manner that each focal spot corresponding to the reference coincides with the centre of the camera plane. However, often the reference beam may have some residual aberrations or it may get aberrated due to the FLCSLM itself. Consequently, the focal

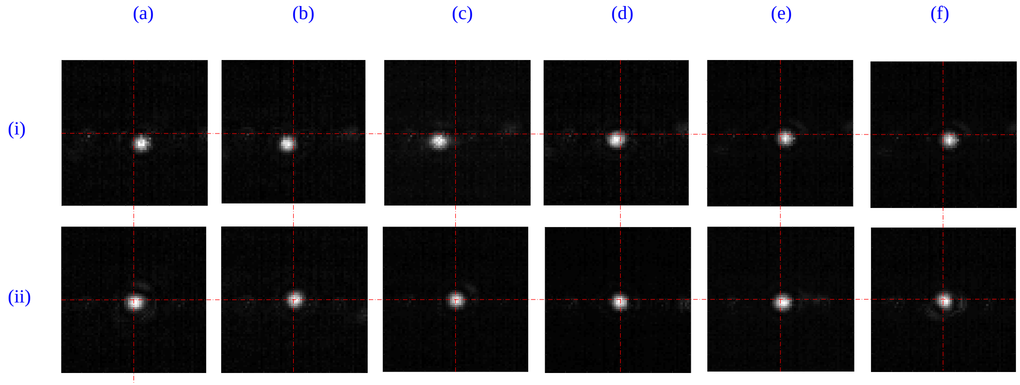

Fig. 5.5 (1 $\longrightarrow f$) Cropped images (68×68 pixels) of the focal spots captured by the camera for the zones in the third row (i) without the correction phase (ii) with correction phase.

spots of the reference beam as shown in Figs. 5.5 (i) ($a \rightarrow f$) are not perfectly centred. However, in addition to the tilt, each binary hologram can also be incorporated with a correction phase to holographically remove the residual aberrations from the reference beam. Figures 5.5 (ii) ($a \rightarrow f$) show the reference focal spots after the binary hologram in each zone is incorporated with correction phase. Figures 5.6 (i) and (ii) show the images

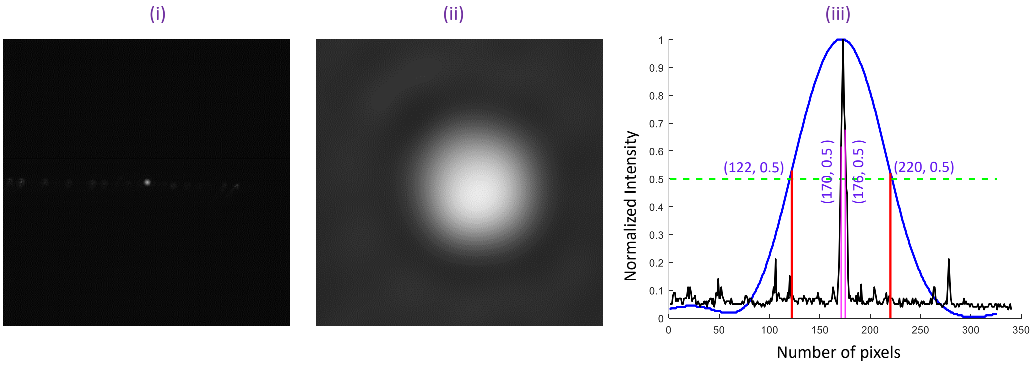

Fig. 5.6 Images of the focal spots as captured by the camera in the (i) low sensitivity and (ii) high sensitivity arrangements. (iii) normalized intensity plots of the two focal spots along a line through the centre of the focal spots; Blue line corresponds to high sensitivity and black line corresponds to low sensitivity.

of a focal spot in the low sensitivity and high sensitivity configuration respectively. A line plot through the centre of each focal spot, Fig. 5.6 (iii), shows that the FWHM in the high sensitivity arrangement is about 17 times larger than that of the low sensitivity arrangement. In order to demonstrate wavefront measurement with high sensitivity in contrast to the low sensitivity measurement, we holographically aberrate the incident beam with different Zernike modes. We first aberrate the incident beam with 0.1 radian of Z_4 and 0.1 radian of Z_9. We also holographically aberrate the incident beam using the linear combination of $-0.14Z_4 + .08Z_{11}$. The test wavefront for each case is estimated both in the high sensitivity and low sensitivity configurations. Figures 5.7 (a) shows the incident phase profile while (b) and (c) show the estimated phase profiles using the low sensitivity and the hight sensitivity configurations, respectively. We can see that the incident phase profile is more accurately estimated in the high sensitivity configuration. This relative improvement can be better visualized when we look at the difference between the applied and estimated phase profiles as seen in Figs 5.7 (d) and (e). We

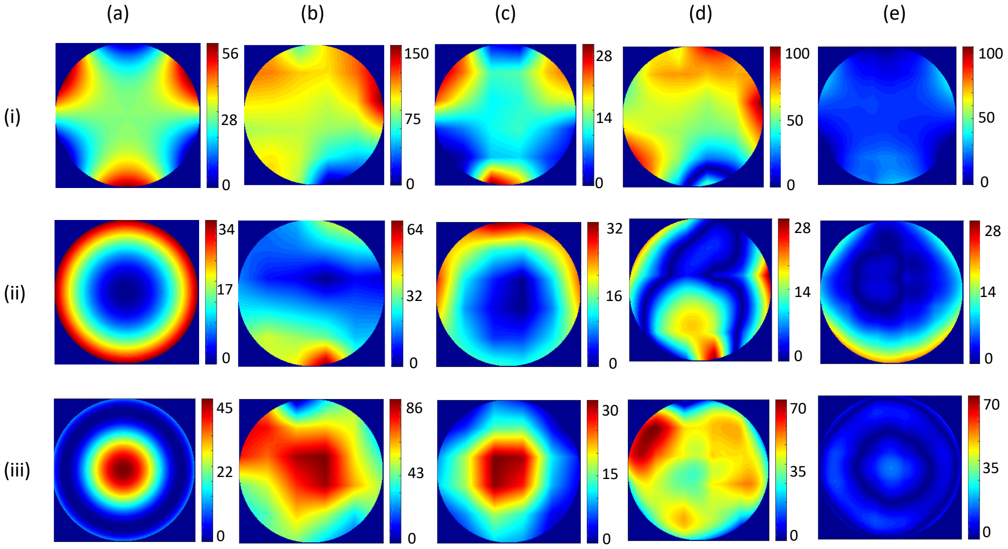

Fig. 5.7 False color images of the (a) incident phase profile, (b) estimated phase profile in the low sensitivity configuration, (c) estimated phase profile in the high sensitivity configuration, (d) absolute difference between the applied phase and estimated phase profile in the low sensitivity configuration, (e) absolute difference between the applied phase and estimated phase profile in the high sensitivity configuration, when the incident phase profile is (i) $0.1Z_4$, (ii) $0.1Z_9$, and (iii)$-0.14Z_4 + .08Z_{11}$. Figures (a), (b) and (c) are self normalised while (d) and (e) share a single color bar expressed in nm.

θ_{min} (μ rad/pixel)	Incident aberration	P_tV(Incident) (nm)	P_tV(Est) (nm)	RMS Error (nm)
52	$0.1Z_4$	34.83	64.13	9.78
3	$0.1Z_4$	34.83	31.58	7.18
52	$0.1Z_9$	56.83	149	54.17
3	$0.1Z_9$	56.83	28.19	15.83
52	$-0.1Z_4+0.08Z_{11}$	47.22	85.60	39.53
3	$-0.1Z_4+0.08Z_{11}$	47.22	31.66	6.46

Table 5.1 Comparison of low sensitivity and high sensitivity modes of the proposed sensor measuring a given incident aberration. PtV represents for peak to valley value of the incident phase profile (i.e. incident) and estimated phase profile (i.e. Est). RMS error is the root mean square error between the incident phase profile and the estimated phase profile.

further utilize the results of the above experiments to obtain the peak valley (PtV) parameter of the incident and estimated phase profiles and to calculate the RMS error between the incidence phase profile and the estimated phase profile. The PtV values and RMS error for the three sets of applied aberrations in both low sensitivity and high sensitivity configuration are presented in Table 5.1. The table clearly demonstrates that the high sensitivity configuration of the zonal wavefront sensor is able to estimate the peak to valley parameter and the entire phase profile much more accurately as compared to the low sensitivity configuration. Therefore, the proposed scheme will be able to measure the thickness profile of thin films with much higher sensitivity. When integrated with a thin film deposition system, the same will enable sensitive on line monitoring of the film growth to realize highly uniform thickness profile.

5.4 Enhancement of dynamic range in a zonal wavefront sensor

In the previous section, a novel scheme to enhance the sensitivity of a zonal wavefront sensor is demonstrated. Since the camera plane contains only one focal spot (arriving from a given zone) at a given time, hence it appears that the same arrangement can also be used for enhance dynamic range by using a shorter focal length. However, this will not be possible straight away because the focal plane of the lens in the previous arrangement also contains other beams in addition to the +1 order beam, especially the zero order beam. If we use shorter image distance or lens of shorter focal length after the FLCSLM, the size of the detector plane should be small enough to exclude the zero order beam, while the +1 order beam in the case of the reference wavefront should be located at the centre of the detector plane. Therefore, significant enhancement in the dynamic range can not be achieved. Instead we propose yet another novel scheme to enhance the dynamic range by utilizing the property of the FLCSLM display. Below we provide a brief description of the proposed scheme.

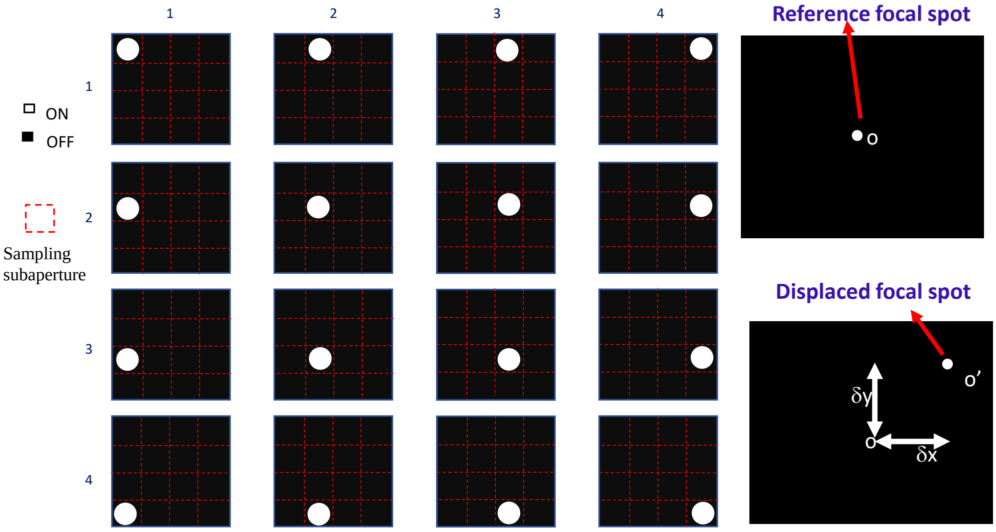

Fig. 5.8 Diagram for each of the 4 × 4 sampling zones in the on state which are displayed sequentially on the FLCSLM panel. As seen in the right panel, the reference focal spot is located at the centre of detector while for the aberrated wavefront it gets displaced from the reference position.

In this scheme also, the FLCSLM plane is divided into $N \times N$ sampling zones. We keep the pixel values of all the zones other than a specific zone as zero so that the light reflected from these zones can not reach the detector. On the other hand the pixel values of the specific zone are kept as 1 so that the detector receives light reflected form the specific zone only. Hence, only one sampling zone is in the on state while the other zones are in the off state. The binary pattern describing such a zone of pixel value 1 and rest of the zones with pixel values 0 can constitute a single bit plane of a 24 bit color image to be sent to the FLCSLM panel. A total of N^2 number of such binary patterns can be created and sequentially displayed on the FLCSLM such that in successive patterns the on state zone scans the entire FLCSLM plane. Figure 5.8 shows 4×4 such binary patterns where we incorporate a circular outline to each on state zone. Display of each binary pattern is followed by the capture of the corresponding focal spot. Since the focal spot is created by light reflected from the on state zone acting like a plane mirror with a circular aperture hence the focal plane will contain only one focal spot that is the zero order focal spot. For the incident reference beam, the zero order focal spot can be aligned to coincide with the centre of the detector plane, as seen in Fig. 5.8. If the incident beam has phase distortion depending on the local slope in the zone, the corresponding zero order beam will be displaced from the reference position. Taking advantage of the property that the focal plane primarily contains only the zero order beam, the image distance can be rendered as small as possible. Record of the focal spots corresponding to the reference wavefront and the test wavefront can then be used to compute the focal spot shifts for each zone to be employed in the phase reconstruction algorithm.

5.4.1 Experimental arrangement for enhancement of dynamic range in zonal wavefront sensor

To demonstrate the principle of enhancement of dynamic range in zonal wavefront sensor, an experimental arrangement with its schematic shown in Fig. 5.9 is considered. Light from the DPSS laser is expanded and collimated before it is incident on the FLCSLM panel. To test the maximum value of the local slope of the wavefront incident on the FLCSLM, we use a galvo scan mirror (Thorlabs *Model No. GVS001 TSH25355, single-axis systems with a dimension of 8.0 mm* × 10.0 mm) in a conjugate plane with respect to the FLCSLM as shown in Fig. 5.9. The wavefront just after the scan mirror

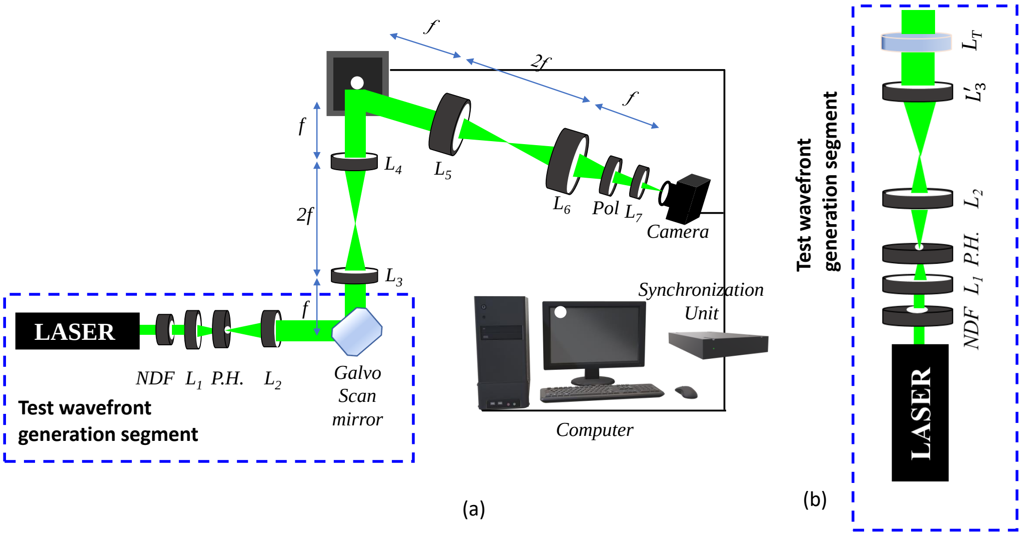

(a) (b)

Fig. 5.9 Schematic of experimental setup to demonstrate the enhancement of the dynamic range of the zonal wavefront sensor, (a) using a galvo scan mirror (b) using a test lens L_T.

is made conjugate with the sensor plane using the lens combination L_3 and L_4. The incident beam is made p-polarized so that with the help of a cross polarizer (pol) placed in front of the detector, we can ensure that light from the zone in the on state only reaches the detector. We again use Basler A504k as the detector array and operate it with full pixel resolution. The combination of lenses L_5 and L_6 are used in a 4f configuration to image the FLCSLM plane at the entrance pupil of a short focal length lens L_7. The focal length of lens L_7 is 40 mm so that it can be positioned almost next to the camera. The display of the binary pattern on the FLCSLM and the image capturing by the camera are synchronised using our synchronisation unit. The present arrangement should provide a maximum dynamic range of $\pm 8.5^o$. As the galvo mirror rotates the local slope of the wavefront on the FLCSLM changes which can be estimated using this sensor. In order to measure the wavefront of a beam transmitted by a lens, we replace the test wavefront generation segment in Fig. 5.9 by another segment shown in Fig. 5.9 (b). Again the arrangement of L_3 and L_4 ensures that the wavefront just after the test lens L_T is made optically conjugate with FLCSLM.

5.4.2 Results and discussion

In our experiments we use 8×8 number of sampling zones described by 1024×1024 pixels of the FLCSLM panel. In the first experiment, we rotate the galvo scan mirror horizontally from $0^o \rightarrow 8.5^o$, first in the clock wise direction and then in the anticlockwise direction. Reference focal spots are recorded when the mirror is in the zero degree position. Displaced focal spots of the test wavefront are recorded for each orientation of the mirror at the interval of 0.5^o. Figures 5.10 ($a \longrightarrow e$) show the images of the recorded focal spots corresponding to a zone having row and column indices 4 and 3, respectively as the mirror rotates $0^o \rightarrow 4^o$ with an interval of 1^o. Figure 5.10 (i) corresponds to the clockwise rotation while Fig. 5.10 (ii) corresponds to the anti-clockwise rotation of the mirror. For each orientation of the galvo scan mirror the wavefront on the FLCSLM plane is estimated using the phase reconstruction algorithm. Similarly, the mirror is rotated vertically through the same range of angles as that of the horizontal rotation. Figures 5.11 (i) and (ii) show the recorded focal spot of the same representative zone as in

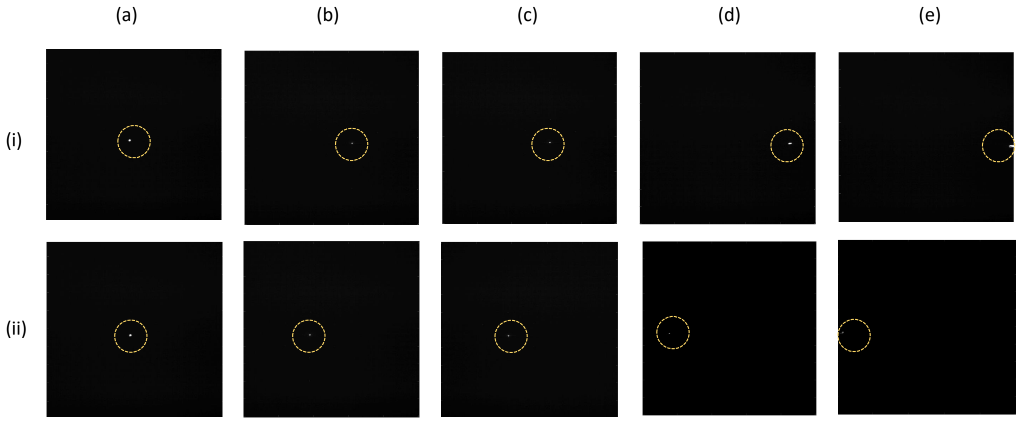

Fig. 5.10 ($a \longrightarrow e$) show the cropped images of the recorded focal spots corresponding to the zone having row and column indices 4 and 3 respectively as the mirror rotates $0^o \rightarrow 4^o$ at an interval of 1^o in the (i) clockwise direction, and (ii) anti-clockwise direction. The mirror rotates in the horizontal plane. Since the focal spot size is very small hence to help its identification we encircle the focal spots with dotted circles.

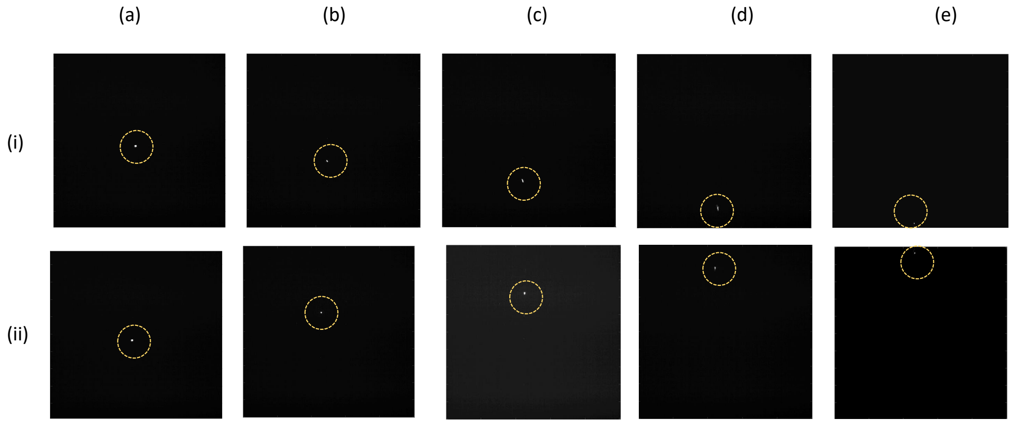

Fig. 5.11 ($a \longrightarrow e$) the cropped images of the recorded focal spots corresponding to the zone having row and column indices 4 and 3 respectively as the mirror rotates $0^o \rightarrow 4^o$ at an interval of 1^o in the (i) clockwise direction, and (ii) anti-clockwise direction. The mirror rotates in the vertical plane. Since the focal spot size is very small hence to enhance the visibility the focal spots are encircled with dotted circles.

the previous case as the mirror rotate from $0^o \rightarrow 4^o$ in the clockwise and anti-clockwise direction with an interval of 1^o.

Table 5.2 Movement of galvo scan mirror in horizontal plane

Applied slope (deg.)	-8.5	-8.0	-7.5	-7.0	-6.5	-6	-5.5	-5.0	...
Estimated slope (deg.)	-8.5	-8.0	-7.7	-7.0	-6.6	-6.1	-5.6	-5.1	...
Applied slope (deg.)	-4.5	-4.0	-3.5	-3.0	-2.5	-2.0	-1.5	-1.0	-0.5
Estimated slope (deg.)	-4.57	-4.0	-3.47	-3.0	-2.47	-2.0	-1.5	-1.0	-.5
Applied slope (deg.)	0.5	1.0	1.5	2.0	2.5	3.0	3.5	4.0	4.5
Estimated slope (deg.)	.44	1.0	1.41	2.0	2.37	2.9	3.39	4.1	4.4
Applied slope (deg.)	5.0	5.5	6.0	6.5	7.0	7.5	8.0	8.5	...
Estimated slope (deg.)	4.8	5.4	6.0	6.3	6.8	7.5	7.9	8.4	...

The estimated wavefronts for each orientation of the scan mirror as it rotates horizontally and vertically are used to determine the corresponding wavefront slopes. Tables 5.2 and 5.3 list the slope angles as applied to the mirror in the horizontal and vertical directions, respectively and the corresponding slope angles as measured by the wavefront

Table 5.3 Movement of galvo scan mirror in vertical plane

Applied slope (deg.)	-8.5	-8.0	-7.5	-7.0	-6.5	-6	-5.5	-5.0	...
Estimated slope (deg.)	-8.5	-7.9	-7.6	-6.8	-6.4	-5.9	-5.4	-5.0	...
Applied slope (deg.)	-4.5	-4.0	-3.5	-3.0	-2.5	-2.0	-1.5	-1.0	-0.5
Estimated slope (deg.)	-4.5	-4.0	-3.2	-2.9	-2.24	-2.0	-1.6	-0.98	-.49
Applied slope (deg.)	0.5	1.0	1.5	2.0	2.5	3.0	3.5	4.0	4.5
Estimated slope (deg.)	0.5	1.0	1.6	1.97	2.24	3.0	3.25	4.0	4.5
Applied slope (deg.)	5.0	5.5	6.0	6.5	7.0	7.5	8.0	8.5	...
Estimated slope (deg.)	4.9	5.5	6	6.5	6.8	7.6	8.0	8.5	...

sensor. We observe that our setup is able to measure incident wavefront slopes in the range $\pm 8.5^o$ both in the horizontal and vertical directions.

We then change the configuration of the experimental arrangement by switching the test wavefront generation segment to Fig. 5.9 (b). In the place of lens L_T we first use a planoconvex lens of focal length 50 mm and then a concave lens of focal length -50 mm. Figure 5.12 (i) (a) is the reference focal spot of the representative zone (row index

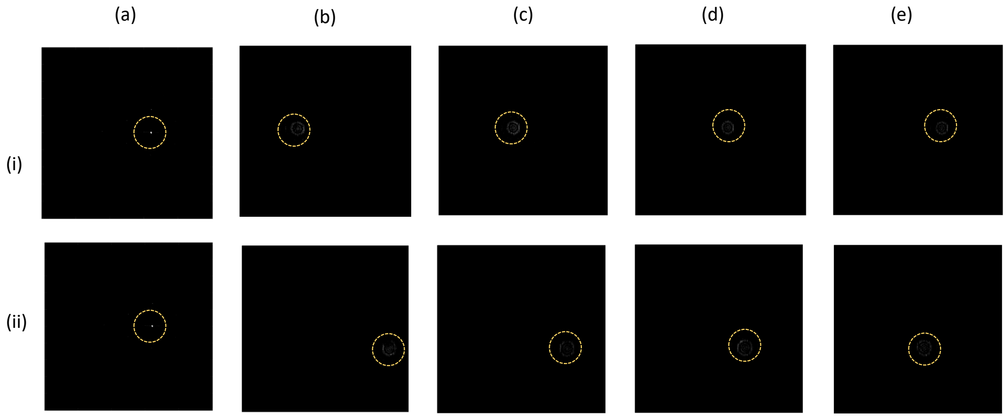

Fig. 5.12 (i) (a) the reference focal spot of the representative zone having row index 4 and column index 3 for the planoconvex lens and (ii) (a) the reference focal spot of the same representative zone for the concave lens. (i) ($b \to e$) the focal spots for the zones with row index 4 and column index varying from 3 to 6 for the test wavefront corresponding to planoconvex lens. (ii) ($b \to e$) the focal spots for the zones with row index 4 and column index varying from 3 to 6 for the test wavefront corresponding to concave lens. The focal spot is encircled for the clarity.

and column index 4 and 3, respectively) used for the planoconvex lens while Fig. 5.12 (ii) (a) is the reference focal spot of the same representative zone for the concave lens. Figures 5.12 (i) ($b \rightarrow e$) show the focal spots of the zones in the fourth row between the third column and the sixth column of the test wavefront corresponding to planoconvex lens while Figs. 5.12 (ii) $b(\rightarrow e)$ are those of for the concave lens.

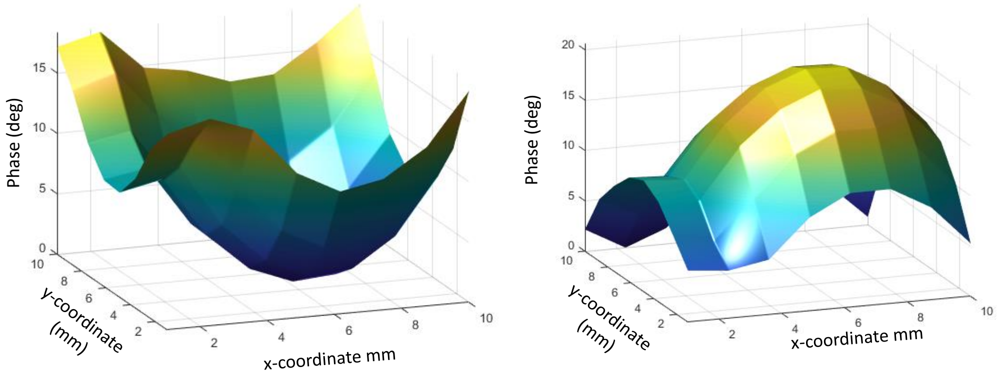

Fig. 5.13 Surface plot of estimated phase profiles corresponding to the (a) planoconvex (b) concave lenses.

Figures 5.13 (a) and (b) show the surface plots of the estimated wavefronts as incident on the FLCSLM plane corresponding to the planoconvex lens and the concave lens, respectively. As the beam passing through the planoconvex lens or the concave lens has a diameter of around 10 mm hence in both cases the maximum local slope on the FLCSLM plane will be greater than 5.5^o. The estimated wavefronts as seen in Fig. 5.13 confirm that our setup is able to measure the positive as well as negative wavefronts curvatures corresponding to the two lenses with reasonable accuracy. We have used the zonal phase information in the estimated wavefronts to obtain the angle that the tangent to the wavefront at a given grid point makes with the vertical axis. This angle is then used to estimate the radius of curvature of the spherical wavefront as incident on the sensor plane, which should also be equal to the focal length of L_T. The estimated focal lengths for the two test lenses are found to be 50.32 mm and -50.03 mm, which correspond to the planoconvex lens and the concave lens, respectively. Thus the estimated wavefronts have the correct radius curvatures almost equal to the focal lengths of the respective test lenses.

Conclusion

In this chapter, a modification in zonal wavefront sensor to enhance the sensitivity and dynamic range of wavefront measurements is presented. We have utilized the capability of the FLCSLM to implement the novel sensitivity enhancement scheme without compromising on the sensing speed. Our setup with enhanced sensitivity has demonstrated measurement of wavefront slope as small as $(\pm 1.72 \times 10^{-4})^o$ while the setup with enhanced dynamic range has demonstrated measurement of slope upto $\pm 8.5^o$. Both the proposed sensitivity and dynamic range enhancement schemes can be implemented for in-situ measurements in thin film deposition units with some minor modification of the experimental arrangements. With these modifications the integrated system will have the capability of monitoring surface growth with enhanced sensitivity to enable growth of uniform surface close to the good flatness and to fabricate high quality periodic and non periodic curve surfaces. Moreover, with some more interfacing with the deposition system, this data can be feedback so as to apply the correction during the deposition to control the growth of the thin film.

CHAPTER 6

Conclusion and Future Prospects

6.1 Conclusion

Thin films are important in several industrial as well as scientific applications. They are the foundation of a number of present-day technologies and devices such as semiconductor, optical and opto-electronic, storage energy devices and so on. The quality and the properties of the thin films are often influenced by the growth process. Therefore, to ensure a quality check on the thin film, the growth of the film is required to be monitored in-situ during the deposition itself. Thickness and surface profile of the thin film can be monitored at regular intervals of time to confirm the desired growth of the film. One thus requires an in-situ surface profile and thickness monitoring technique that can be employed during the growth of the film. However, a survey of the available literature reveals that most of the in-situ measurement techniques require prior information on the properties of the substrate and the material being deposited. In this thesis, we have proposed a novel grating array based wavefront sensor (GAWS) for in-situ and online monitoring of both surface and thickness profile simultaneously during the deposition process. The proposed technique does not require prior information of the substrate and target material; it just demands that the substrate and the film should have sufficient reflectivity within the detection limit of the camera. The measurement is instantaneous and is applicable for any type of deposition system equipped with suitable view ports for launching the collimated laser beam on to the substrate/thin film and to take out the corresponding reflected beam so as to direct it on to the sensor placed outside the deposition system. We have developed the proposed wavefront sensor using a ferroelectric liquid crystal spatial light modulator and a CMOS camera as the key components. After testing wavefront measurement capability of the sensor, it is integrated to a pulsed laser deposition (PLD) system. The PLD system provides a flexible yet efficient way to deposit high quality thin film on any material. The PLD unit is fitted with a number of view ports which can be used for easy integration of the present wavefront sensor setup. The phase profile reconstruction algorithm of the integrated system is suitably modified to obtain the thickness profile of the deposited thin film. With the proposed scheme, the measurements of surface and thickness profiles of Cu thin film during deposition are performed in situ. Measurements have been done at regular intervals of time starting at $t = 0$ (bare substrate, as a reference) till the completion of the growth process, at $t = 125$ minutes, keeping the interval of time as five minutes. After deposition, the thickness profile of the deposited thin film is measured along a line across it via a commercial stylus profilometer and the two results are found to be in agreement thus validating the GAWS scheme proposed in the thesis. We have also proposed further modification in the wavefront sensing scheme to enhance the sensitivity and dynamic range of the wavefront sensor. We verify the accuracy of the scheme to enhance sensitivity by measuring known amount of holographically introduced aberrations. The scheme to enhance the dynamic range is tested on the transmitted wavefronts through convex and concave lenses. The radii of curvature of the transmitted spherical wavefronts as measured by the proposed zonal wavefront sensing scheme correspond to focal lengths that agree well with the commercial data provided by the lens manufacturer. Our setup with enhanced sensitivity has demonstrated measurement of wavefront slope as small as $(\pm 1.72 \times 10^{-4})^o$ while the setup with enhanced dynamic range has demonstrated measurement of slope up to $\pm 8.5^o$. With the increased sensitivity, the GAWS can be integrated to the thin film deposition system to monitor the surface profile of the thin film during the deposition in a much more sensitive manner where the film can be deposited much more uniformly. On the other hand, the increased dynamic range capability of the integrated system will make it possible to monitor the periodic and non-periodic or non-uniform curved thin film surfaces containing large local slopes.

6.2 Future Prospects

Some of the future scope of the thesis work is highlighted below:

1. In this thesis, we have measured the surface profile during deposition at an interval of 5 minutes. However, the laser pulses used in the present PLD system is operated at a repetition rate of 10 Hz. Since the measurement by our sensor is instantaneous therefore it will be possible to monitor the surface growth on shot to shot basis with the laser pulses by synchronising the detection camera with the laser trigger. The shot to shot monitoring of the film can be utilized to unveil the growth dynamics of the film which in turn will throw light on the other physical properties of the film.

2. Although the new GAWS sensing scheme at present is demonstrated on the PLD system but it can also be implemented on any other deposition system having suitable view ports.

3. The flexibility offered by the PLD system can be utilized to deposit periodic structured thin film. Since in the integrated system, the deposition is monitored by our sensor at regular interval of time, the quality of such deposited structure can be monitored in a superior manner by the GAWS as compared to those of already available techniques, particularly the in situ non-contact modes.

4. In this thesis, the working of two novel schemes to enhance the sensitivity and the dynamic range of the wavefront sensor is also demonstrated. With some minor alteration in the detection path, the same schemes can be implemented in the

integrated system or any other device, requiring the monitoring of the surface profiling of uniform surface or large uneven surfaces.

5. The number of sampling zones of our wavefront sensor can be easily increased by several times by reducing the size of each zone. One can also increase the number of effective zones without decreasing the size of the zone by digitally shifting the grating pattern utilizing sequential display property of the FLCSLM.

References

[1] David Snoke. *Solid state physics: Essential concepts*. Cambridge University Press, 2020. 1

[2] AR West. 'solid state chemistry'john willey & sons, 2003. 1, 2

[3] HA Macleod. *Thin-film optical coating design*. Marcel Dekker, New York, 1995. 1

[4] Sriram Sundararajan and Bharat Bhushan. Development of a continuous microscratch technique in an atomic force microscope and its application to study scratch resistance of ultrathin hard amorphous carbon coatings. *Journal of Materials Research*, 16(2):437–445, 2001. 1

[5] Charles A Paulson, James J Price, Karl W Koch, Chang-Gyu Kim, Jeong-Hong Oh, Lin Lin, Ananth N Subramanian, Binwei Zhang, Jaymin Amin, Alexandre Mayolet, et al. Industrial-grade anti-reflection coatings with extreme scratch resistance. *Optics Letters*, 44(24):5977–5980, 2019. 1

[6] Jitka Mohelnikova. Materials for reflective coatings of window glass applications. *Construction and Building Materials*, 23(5):1993–1998, 2009. 1

[7] Georg Hass, Maurich H Francombe, and Richard W Hoffman. *Physics of thin films: Advances in research and development*. Elsevier, 2013. 1

[8] Robert A Street, TN Ng, David E Schwartz, Gregory L Whiting, JP Lu, RD Bringans, and Janos Veres. From printed transistors to printed smart systems. *Proceedings of the IEEE*, 103(4):607–618, 2015. 1

[9] Jessica L Felhofer, Lucas Blanes, and Carlos D Garcia. Recent developments in instrumentation for capillary electrophoresis and microchip-capillary electrophoresis. *Electrophoresis*, 31(15):2469–2486, 2010. 1

[10] Daesu Lee, Sang Mo Yang, Tae Heon Kim, Byung Chul Jeon, Yong Su Kim, Jong-Gul Yoon, Ho Nyung Lee, Seung Hyup Baek, Chang Beom Eom, and Tae Won Noh. Multilevel data storage memory using deterministic polarization control. *Advanced Materials*, 24(3):402–406, 2012. 1

[11] Mark H Kryder. Magnetic thin films for data storage. *Thin solid films*, 216(1):174–180, 1992. 1

[12] Chuan Wang, Jialu Zhang, Koungmin Ryu, Alexander Badmaev, Lewis Gomez De Arco, and Chongwu Zhou. Wafer-scale fabrication of separated carbon nanotube thin-film transistors for display applications. *Nano Letters*, 9(12):4285–4291, 2009. 1

[13] Kasturi L Chopra. Thin film phenomena. 1969. 1, 2

[14] Huahua Yang, Pai Peng, Qianqian Sun, Qiang Zhang, Na Ren, Fengpeng Han, and Diao She. Developed carbon nanotubes/gutta percha nanocomposite films with high stretchability and photo-thermal conversion efficiency. *Journal of Materials Research and Technology*, 9(4):8884–8895, 2020. 1

[15] John E Mahan. *Physical vapor deposition of thin films*. 2000. 2

[16] Dainius Perednis and Ludwig J Gauckler. Thin film deposition using spray pyrolysis. *Journal of electroceramics*, 14(2):103–111, 2005. 2

[17] Hideki Matsumura. Formation of silicon-based thin films prepared by catalytic chemical vapor deposition (cat-cvd) method. *Japanese Journal of Applied Physics*, 37(6R):3175, 1998. 2

[18] CJ Brinker, AJ Hurd, GC Frye, KJ Ward, and CS Ashley. Sol-gel thin film formation. *Journal of Non-Crystalline Solids*, 121(1-3):294–302, 1990. 2

[19] Caprice Gray, Jianna Wang, Gregg Duthaler, Andrew Ritenour, and Paul S Drzaic. Screen printed organic thin film transistors (otfts) on a flexible substrate. In *Organic Field Effect Transistors*, volume 4466, pages 89–94. International Society for Optics and Photonics, 2001. 2

[20] Ming-Bo Lin. *Introduction to VLSI systems: a logic, circuit, and system perspective*. CRC press, 2011. 2

[21] EM Oks, AV Tyunkov, Yu G Yushkov, and DB Zolotukhin. Ceramic coating deposition by electron beam evaporation. *Surface and Coatings Technology*, 325:1–6, 2017. 2

[22] Brian R Pamplin. *Molecular beam epitaxy*. Elsevier, 2017. 2

[23] Indrajeet Kumar and Alika Khare. Multi-and few-layer graphene on insulating substrate via pulsed laser deposition technique. *Applied surface science*, 317:1004–1009, 2014. 2

[24] Kiyotaka Wasa, Makoto Kitabatake, and Hideaki Adachi. *Thin film materials technology: sputtering of control compound materials*. Springer Science & Business Media, 2004. 2

[25] Edgar Alfonso, Jairo Olaya, and Gloria Cubillos. Thin film growth through sputtering technique and its applications. *Crystallization-Science and technology*, 23:11–12, 2012. 2

[26] S Fernandez and FB Naranjo. Optimization of aluminum-doped zinc oxide films deposited at low temperature by radio-frequency sputtering on flexible substrates for solar cell applications. *Solar Energy Materials and Solar Cells*, 94(2):157–163, 2010. 2

[27] A Barhoumi, G Leroy, B Duponchel, J Gest, L Yang, N Waldhoff, and S Guermazi. Aluminum doped zno thin films deposited by direct current sputtering: structural and optical properties. *Superlattices and Microstructures*, 82:483–498, 2015. 2

[28] Chao Lu and Alvin Warren Czanderna. *Applications of piezoelectric quartz crystal microbalances*. Elsevier, 2012. 3

[29] J Hornsteiner, E Born, G Fischerauer, and E Riha. Surface acoustic wave sensors for high-temperature applications. In *Proceedings of the 1998 IEEE International Frequency Control Symposium (Cat. No. 98CH36165)*, pages 615–620. IEEE, 1998. 3

[30] Adnan Mujahid, Adeel Afzal, and Franz L Dickert. An overview of high frequency acoustic sensors—qcms, saws and fbars—chemical and biochemical applications. *Sensors*, 19(20):4395, 2019. 3

[31] Jun Pei, F Levent Degertekin, BV Honein, Butrus T Khuri-Yakub, and Krishna C Saraswat. In situ thin film thickness measurement using ultrasonics waves. In

1994 Proceedings of IEEE Ultrasonics Symposium, volume 2, pages 1237–1240. IEEE, 1994. 3

[32] Steven A Henck, Walter M Duncan, Lee M Lowenstein, and Stephanie Watts Butler. In situ spectral ellipsometry for real-time thickness measurement: Etching multilayer stacks. *Journal of Vacuum Science & Technology A: Vacuum, Surfaces, and Films*, 11(4):1179–1185, 1993. 3

[33] Harland Tompkins and Eugene A Irene. *Handbook of ellipsometry*. William Andrew, 2005. 3

[34] M Sarfaty, C Baum, R Breun, N Hershkowitz, JL Shohet, K Nagpal, TL Vincent, and PP Khargonekar. Real-time measurement of thin film thickness during plasma processing. *Plasmas and polymers*, 2(4):229–244, 1997. 4

[35] Maciej Kraszewski and Robert Bogdanowicz. Laser reflectance interferometry system with a 405 nm laser diode for in situ measurements of cvd diamond thickness. *Metrology and Measurement Systems*, 20(4), 2013. 4

[36] Herbert H Sawin, William T Conner, Timothy J Dalton, and Emanuel M Sachs. Apparatus and method for real-time measurement of thin film layer thickness and changes thereof, September 12 1995. US Patent 5,450,205. 4

[37] Christopher D Zuiker, Dieter M Gruen, and Alan R Krauss. In situ laser reflectance interferometry measurement of diamond film growth. *Journal of applied physics*, 79(7):3541–3547, 1996. 4

[38] Yu-Chia Tsao, Woo-Hu Tsai, Wen-Ching Shih, and Mu-Shiang Wu. An in-situ real-time optical fiber sensor based on surface plasmon resonance for monitoring the growth of tio2 thin films. *Sensors*, 13(7):9513–9521, 2013. 4

[39] Farzia Karim, Tanujjal Bora, Mayur B Chaudhari, Khaled Habib, Waleed S Mohammed, and Joydeep Dutta. Optical fiber-based sensor for in situ monitoring of cadmium sulfide thin-film growth. *Optics letters*, 38(24):5385–5388, 2013. 4

[40] Bosanta R Boruah. Zonal wavefront sensing using an array of gratings. *Optics letters*, 35(2):202–204, 2010. 5, 35

[41] Robert K Tyson. *Principles of adaptive optics*. CRC press, 2015. 6

[42] Bo Xin, Chuck Claver, Ming Liang, Srinivasan Chandrasekharan, George Angeli, and Ian Shipsey. Curvature wavefront sensing for the large synoptic survey telescope. *Applied Optics*, 54(30):9045–9054, 2015. 6

[43] Junzhong Liang, Bernhard Grimm, Stefan Goelz, and Josef F Bille. Objective measurement of wave aberrations of the human eye with the use of a hartmann–shack wave-front sensor. *JOSA A*, 11(7):1949–1957, 1994. 6

[44] X Li, LP Zhao, ZP Fang, A Asundi, and XM Yin. Surface measurement with shack-hartmann wavefront sensing technology. In *Ninth International Symposium on Laser Metrology*, volume 7155, page 715515. International Society for Optics and Photonics, 2008. 6

[45] A Nutsch, L Pfitzner, T Grandin, X Levecq, and S Bucourt. Determination of flatness on patterned wafer surfaces using wavefront sensing methods. In *Ninth International Symposium on Laser Metrology*, volume 7155, page 71550Z. International Society for Optics and Photonics, 2008. 6

[46] Andreas Zepp. Characterization of the holographic wavefront sensor for free-space optical communications. In *Remote Sensing of Clouds and the Atmosphere XVIII; and Optics in Atmospheric Propagation and Adaptive Systems XVI*, volume 8890, page 88901F. International Society for Optics and Photonics, 2013. 6

[47] Feng Feng, Ian H White, and Timothy D Wilkinson. Aberration correction for free space optical communications using rectangular zernike modal wavefront sensing. *Journal of lightwave technology*, 32(6):1239–1245, 2014.

[48] Santanu Konwar and Bosanta R Boruah. Leveraging the orthogonality of zernike modes for robust free-space optical communication. *Communications Physics*, 3(1):1–9, 2020. 6

[49] Jérome Primot. Theoretical description of shack–hartmann wave-front sensor. *Optics Communications*, 222(1-6):81–92, 2003. 6

[50] Mark AA Neil, Martin J Booth, and Tony Wilson. New modal wave-front sensor: a theoretical analysis. *JOSA A*, 17(6):1098–1107, 2000. 6, 26

[51] M Carbillet, A Ferrari, C Aime, HI Campbell, and AH Greenaway. Wavefront sensing: from historical roots to the state-of-the-art. *European Astronomical Society Publications Series*, 22:165–185, 2006. 6

[52] Martin J Booth. Direct measurement of zernike aberration modes with a modal wavefront sensor. In *Advanced Wavefront Control: Methods, Devices, and Applications*, volume 5162, pages 79–90. SPIE, 2003. 6

[53] Santanu Konwar and Bosanta R Boruah. Improved linear response in a modal wavefront sensor. *JOSA A*, 36(5):741–750, 2019. 6

[54] Ben C Platt and Roland Shack. History and principles of shack-hartmann wavefront sensing, 2001. 6

[55] William H Southwell. Wave-front estimation from wave-front slope measurements. *JOSA*, 70(8):998–1006, 1980. 6, 28, 29, 37

[56] Biswajit Pathak. Improved wavefront estimation accuracy in a programmable grating array based wavefront sensor. *Journal of Optics*, 23(4):045604, 2021. 6, 54

[57] Bosanta R Boruah. Dynamic manipulation of a laser beam using a liquid crystal spatial light modulator. *American Journal of Physics*, 77(4):331–336, 2009. 7, 16

[58] Biswajit Pathak and Bosanta R Boruah. Zonal wavefront sensing with enhanced spatial resolution. *Optics letters*, 41(23):5600–5603, 2016. 8

[59] Parameswaran Hariharan and Katherine Creath. Interferometry. *The Optics Encyclopedia: Basic Foundations and Practical Applications*, 2007. 12

[60] Wai-Hon Lee. Binary synthetic holograms. *Applied optics*, 13(7):1677–1682, 1974. 15

[61] MAA Neil, T Wilson, and R Juskaitis. A wavefront generator for complex pupil function synthesis and point spread function engineering. *Journal of Microscopy*, 197(3):219–223, 2000. 16

[62] Robert J Noll. Zernike polynomials and atmospheric turbulence. *JOsA*, 66(3):207–211, 1976. 18

[63] Uzi Efron. *Spatial light modulator technology: materials, devices, and applications*, volume 47. CRC press, 1994. 20

[64] Joseph W Goodman. Introduction to fourier optics (reissue), chap. 4-1, 1988. 20

[65] Heinz J Deuling. Deformation of nematic liquid crystals in an electric field. *Molecular Crystals and Liquid Crystals*, 19(2):123–131, 1972. 20

[66] David Coates. Development and applications of cholesteric liquid crystals. *Liquid Crystals*, 42(5-6):653–665, 2015. 20

[67] Robert B Meyer. Ferroelectric liquid crystals; a review. *Molecular Crystals and Liquid Crystals*, 40(1):33–48, 1977. 20

[68] AD Cohen, MC Parker, and RJ Mears. Applications of flc slm dynamic holograms to wdm network components. *Ferroelectrics*, 214(1):101–108, 1998. 20

[69] Jim Schwiegerling and Daniel R Neal. Historical development of the shack-hartmann wavefront sensor. *Robert Shannon and Roland Shack: Legends in Applied Optics, edited by JE Harvey and RB Hooker—SPIE, Bellingham, WA*, pages 132–139, 2005. 26

[70] Iuliia Shatokhina, Victoria Hutterer, and Ronny Ramlau. Review on methods for wavefront reconstruction from pyramid wavefront sensor data. *Journal of Astronomical Telescopes, Instruments, and Systems*, 6(1):010901, 2020. 26

[71] Simone Esposito and Armando Riccardi. Pyramid wavefront sensor behavior in partial correction adaptive optic systems. *Astronomy & Astrophysics*, 369(2):L9–L12, 2001. 26

[72] Carl Paterson and JC Dainty. Hybrid curvature and gradient wave-front sensor. *Optics letters*, 25(23):1687–1689, 2000. 26

[73] Francois Roddier, Claude Roddier, and Nicolas Roddier. Curvature sensing: a new wavefront sensing method. In *Statistical Optics*, volume 976, pages 203–209. SPIE, 1988. 26

[74] Biswajit Pathak and Bosanta R Boruah. Improved wavefront reconstruction algorithm for shack–hartmann type wavefront sensors. *Journal of Optics*, 16(5):055403, 2014. 28, 29, 32, 37

[75] Svenja Ettl, Jürgen Kaminski, Markus C Knauer, and Gerd Häusler. Shape reconstruction from gradient data. *Applied Optics*, 47(12):2091–2097, 2008. 29

[76] Iacopo Mochi and Kenneth A Goldberg. Modal wavefront reconstruction from its gradient. *Applied Optics*, 54(12):3780–3785, 2015. 29

[77] Richard H Hudgin. Wave-front reconstruction for compensated imaging. *JOSA*, 67(3):375–378, 1977. 29

[78] David L Fried. Least-square fitting a wave-front distortion estimate to an array of phase-difference measurements. *JOSA*, 67(3):370–375, 1977. 29

[79] Weiyao Zou and Jannick P Rolland. Quantifications of error propagation in slope-based wavefront estimations. *JOSA A*, 23(10):2629–2638, 2006. 30

[80] Yousef Saad and Henk A Van Der Vorst. Iterative solution of linear systems in the 20th century. *Numerical Analysis: Historical Developments in the 20th Century*, pages 175–207, 2001. 34

[81] Haiyang Quan, Xi Hou, Fan Wu, and Weihong Song. Absolute measurement of optical flats based on basic iterative methods. *Optics express*, 23(12):16305–16319, 2015. 34

[82] Norbert Lindlein, Johannes Pfund, and Johannes Schwider. Expansion of the dynamic range of a shack-hartmann sensor by using astigmatic microlenses. *Optical Engineering*, 39(8):2220–2225, 2000. 35, 76

[83] Lei Yu, Mingliang Xia, Hongsheng Xie, Li Xuan, and Ji Ma. Novel methods to improve the measurement accuracy and the dynamic range of shack–hartmann wavefront sensor. *Journal of Modern Optics*, 61(9):703–715, 2014. 35

[84] DB Geohegan, DB Chrisey, and GK Hubler. Pulsed laser deposition of thin films. *Chrisey and GK Hubler (eds), Wiely, New York*, pages 59–69, 1994. 50

[85] Douglas H Lowndes, DB Geohegan, AA Puretzky, DP Norton, and CM Rouleau. Synthesis of novel thin-film materials by pulsed laser deposition. *Science*, 273(5277):898–903, 1996. 50

[86] Michael Lorenz and MS Ramachandra Rao. 25 years of pulsed laser deposition. *Journal of Physics D: Applied Physics*, 47(3):030301, 2013. 50

[87] Howard M Smith and AF Turner. Vacuum deposited thin films using a ruby laser. *Applied Optics*, 4(1):147–148, 1965. 50

[88] D Dijkkamp, T Venkatesan, XD Wu, SA Shaheen, N Jisrawi, YH Min-Lee, WL McLean, and Mark Croft. Preparation of y-ba-cu oxide superconductor thin films using pulsed laser evaporation from high t c bulk material. *Applied Physics Letters*, 51(8):619–621, 1987. 50

[89] Gaurav Shukla and Alika Khare. Spectroscopic studies of laser ablated zno plasma and correlation with pulsed laser deposited zno thin film properties. *Laser and Particle Beams*, 28(1):149–155, 2010. 50

[90] Satchi Kumari and Alika Khare. Optical and structural characterization of pulsed laser deposited ruby thin films for temperature sensing application. *Applied surface science*, 265:180–186, 2013. 50

[91] ATT Mostako, Alika Khare, CVS Rao, Sudhirsinh Vala, TK Basu, Prakash M Raole, and Rajinikant Makwana. Post-irradiation effect of deuterium ion beam onto rh/w/cu multilayer thin film. *Journal of nuclear materials*, 446(1-3):63–67, 2014. 50

[92] Eugene G Gamaly, Andrei V Rode, Barry Luther-Davies, et al. Ultrafast laser ablation and film deposition. *Pulsed laser deposition of thin films*, pages 99–130, 2007. 50

[93] Samuel S Mao, Xianglei Mao, Ralph Greif, and Richard E Russo. Initiation of an early-stage plasma during picosecond laser ablation of solids. *Applied Physics Letters*, 77(16):2464–2466, 2000. 50

[94] KL Chopra, PD Paulson, and V Dutta. Thin-film solar cells: an overview. *Progress in Photovoltaics: Research and applications*, 12(2-3):69–92, 2004. 75

[95] K Akimoto, S Ishizuka, M Yanagita, Y Nawa, Goutam K Paul, and T Sakurai. Thin film deposition of cu2o and application for solar cells. *Solar energy*, 80(6):715–722, 2006. 75

[96] Ivan Moreno, J Jesus Araiza, and Maximino Avendano-Alejo. Thin-film spatial filters. *Optics letters*, 30(8):914–916, 2005. 75

[97] Amin Abbasiyan, Mina Noori, and Hamed Baghban. Investigation of quasi-periodic structures to increase the efficiency of thin-film silicon solar cells: a comparative study. *Solar Energy Materials and Solar Cells*, 202:110129, 2019. 75

[98] Wenbin Gao, Manwen Yao, and Xi Yao. Achieving ultrahigh breakdown strength and energy storage performance through periodic interface modification in srtio3 thin film. *ACS applied materials & interfaces*, 10(34):28745–28753, 2018. 75

[99] Cristine Calil Kores, Michael Fokine, and Fredrik Laurell. Uv-written grating couplers on thin-film lithium niobate ridge waveguides. *Optics Express*, 28(19):27839–27849, 2020. 75

[100] Martin Rais, Jean-Michel Morel, Carole Thiebaut, Jean-Marc Delvit, and Gabriele Facciolo. Improving wavefront sensing with a shack–hartmann device. *Applied optics*, 55(28):7836–7846, 2016. 76

[101] AG Basden, TJ Morris, D Gratadour, and E Gendron. Sensitivity improvements for shack–hartmann wavefront sensors using total variation minimization. *Monthly Notices of the Royal Astronomical Society*, 449(4):3537–3542, 2015. 76

[102] Changwei Li, Bangming Li, and Sijiong Zhang. Phase retrieval using a modified shack–hartmann wavefront sensor with defocus. *Applied optics*, 53(4):618–624, 2014. 76

[103] Geun-Young Yoon, Seth Pantanelli, and Lana J Nagy. Large-dynamic-range shack-hartmann wavefront sensor for highly aberrated eyes. *Journal of Biomedical Optics*, 11(3):030502, 2006. 76

[104] Chia-Yu Ai. Apparatus and method for measuring a wavefront using a screen with apertures adjacent to a multi-lens array, April 15 2003. US Patent 6,548,797. 76

[105] Wei Su, Yan Zhou, and Qing Chun Zhao. Sequential wavefront sensor, November 4 2008. US Patent 7,445,335. 76

[106] Daniel R Neal and Justin D Mansell. Apodized micro-lenses for hartmann wavefront sensing and method for fabricating desired profiles, March 8 2005. US Patent 6,864,043. 76

[107] Vinna Lin, Hsiang-Chun Wei, and Guo-Dung J Su. Shack-hartmann wavefront sensor with high sensitivity by using long focal length microlens array. In *Unconventional Imaging, Wavefront Sensing, and Adaptive Coded Aperture Imaging and Non-Imaging Sensor Systems*, volume 8165, page 81650V. International Society for Optics and Photonics, 2011. 76

[108] Vincent Laude, Ségolène Olivier, Carine Dirson, and Jean-Pierre Huignard. Hartmann wave-front scanner. *Optics letters*, 24(24):1796–1798, 1999. 76

List of publications/patents and other scientific activities

Patent

1. **Nagendra Kumar**, Alika Khare and Bosanta R. Boruah, “A wavefront measuring system and method with ameliorated dynamic range”, Indian Patent Application No.: 202131015140, 31 March 2021.

Publications

1. Karuna Sindhu Malik, **Nagendra Kumar**, Akanshu Chauhan, Nedup Sherpa and Bosanta R. Boruah, “Understanding dynamic beam shaping using liquid crystal spatial light modulator,” Asian Journal of Physics, Vol. 28 Nos 10-12, 2019, 1197-1204.
2. **Nagendra Kumar**, Alika Khare and Bosanta R. Boruah, “An ex-situ surface profile measurement scheme using a zonal wavefront sensor with simultaneous presence of reference and test wavefronts,” Proc. of SPIE, Vol 11287, 1128719 (2 March 2020).
3. **Nagendra Kumar**, Alika Khare and Bosanta R. Boruah, “Enhanced dynamic range of the grating array based zonal wavefront sensor using a zone wise scanning method,” Proc. of SPIE, Vol 11287, 112870E (2 March 2020).
4. **Nagendra Kumar** and Bosanta R. Boruah, “Effect of pixel size and pixel fill factor of a pixelated device on the holographically shaped beam", Asian Journal of Physics Vol. 29, Nos 10-12 (2020) 673-680.

5.

6. **Nagendra Kumar** , Alika Khare, Bosanta R. Boruah, “ Enhancement of wavefront measurement sensitivity in a zonal wavefront sensor without curtailing the sensing speed” J. Opt. 24 (2022) 014003.

7. **Nagendra Kumar**, Biswajit Pathak, Rahul Kesarwani, Sumit Goswami, Alika Khare and Bosanta R. Boruah, “Implementation of grating array based wavefront sensor to monitor surface and thickness profile in real time during deposition of the thin film", under review (optics letters).

8. Karuna Sindhu Malik, **Nagendra Kumar**and Bosanta R. Boruah “Dynamic modulation of spatial intensity profile of a laser beam using a binary hologram", under review (optics communications)

9. **Nagendra Kumar**, Alika Khare and Bosanta R. Boruah, “Zonal wavefront sensing with an ultra-high dynamic range", Manuscript under preparation.

Conference Presentations

1. **Nagendra Kumar**, Alika Khare and Bosanta R. Boruah, “Enhanced dynamic range of the Grating array based zonal wavefront sensor using a zone wise scanning method” Photonics West 2020 1-6 February, 2020, Sanfrasico California USA.

2. **Nagendra Kumar**, Alika Khare and Bosanta R. Boruah, “An ex-situ surface profile measurement scheme using a zonal wavefront sensor with simultaneous presence of reference and test wavefronts” Photonics West 2020 1-6 February, 2020, Sanfrasico California USA.

3. **Nagendra Kumar**, Alika Khare and Bosanta R. Boruah, “Grating array based zonal wavefront sensor for surface profile measurements” Siegman International School on Lasers organized by Technical University of Denmark at Spirit of Hven Backfallsbyn, Sweden, July 28 - August 4 , 2018.

4. **Nagendra Kumar**, Alika Khare and Bosanta R. Boruah, “Improvement in phase estimation accuracy at the peripheral grid points of a zonal wavefront sensor” Photonics 2018 12-15 December, 2018, IIT Delhi.

5. **Nagendra Kumar**, Alika Khare and Bosanta R. Boruah, “Dynamic Phase manipulation and wavefront estimation of a laser beam using computer generated

holography technique" Research Conclave'18 (An amalgamation of Academia, Industry and Startup), 8-11 March 2018.

6. **Nagendra Kumar**, Alika Khare and Bosanta R. Boruah,"A comparison between optical and non-optical methods for in-situ Surface profiling and thickness measurement of thin film" International conference on Advances in Optics and Photonics (XLI conference of Optical Society of India), November 23- 26, 2017.
7. **Nagendra Kumar**, Alika Khare and Bosanta R. Boruah,"Liquid Crystal Spatial Light Modulator Based wavefront sensing and its Application" Research Conclave'17 (An amalgamation of Academia, Industry and Startup), 16-19 March 2017.

School/ Workshop attended

1. Participated in TEQIP – III sponsored Five days workshop cum Training on "training and practice on MATLAB for engineering solution (TPMES- 20), November 26-30", Dept. of Mechanical Engineering, National Institute of Technology Jalandhar, India
2. Participated in the workshop entitled "Advance Excel" at Research Conclave'18 organized by Students' Academic Board, March 8-11, 2019, Indian Institute of Technology Guwahati, India.
3. Participated in the workshop entitled "Matlab Workshop" at Research Conclave'18 organized by Students' Academic Board, March 8-11, 2019, Indian Institute of Technology Guwahati, India.
4. Participated in the workshop entitled "Intra IIT Latex Workshop", jointly organized by Research Scholar Forum Mathematics, and Student Academic Board, IIT Guwahati at IIT Guwahati on February 18, 2017.
5. Participated in the workshop entitled "IEEE Workshop on Advanced MATLAB Applications to Robotics and Signal Processing" October 7-8, 2017 at Indian Institute of Technology Guwahati, India.
6. Participated in the Latex Workshop" on September 9, 2017 organized by Research Scholar Forum, EEE IIT Guwahati, India.

7. Participated in the workshop entitled “One Day Workshop on Vacuum Technology and its Application in Optical Science” jointly organized by SPIE IIT Guwahati Student Chapter and Pfeiffer Vacuum Pvt.Ltd., on August 19, 2017.
8. Participated in the workshop entitled “One Day Workshop on Introduction to MATLAB” organized by SPIE IIT Guwahati Student Chapter on August 10, 2019.
9. Attended a summer School on lasers entitled “Seigmann International school on lasers” organized by Technical University of Denmark at Spirit of Hven Backfallsbyn, Sweden, July 28 to August 4 , 2018.
10. Participated SPIE leadership workshop Sanfransico , California USA, February 2020.
11. Attended a summer School entitled “ Adaptive Optics European Summer School” June 7-10, 2021 virtual summer school, UK.
12. Participated “International Conference on Sophisticated Instruments in Modern Research" at Indian Institute of Technology Guwahati June 30 - July 1, 2017.
13. Participated IEEE Workshop on Advanced MATLAB Applications to Robotics and Signal Processing October 7- 8, 2017 at Indian Institute of Technology Guwahati, India.
14. Participated Matlab Workshop in Research Conclave’18 organized by Students’ Academic Board, Indian Institute of Technology Guwahati, India.
15. Participated Advance Excel Workshop at Research Conclave’18 organized by Students’ Academic Board, Indian Institute of Technology Guwahati, India.

Achievements

1. Received a scholarship to attend the Adaptive Optics European Summer School virtual mode, 7 -10 June, 2021, UK.
2. Received “SPIE Student Officer Travel Grant” (USD 2400) to attend “SPIE Photonics West -2020” at San Francisco, California, USA from 1-6 February, 2020, organized by SPIE.

3. Received a grant of USD 700 to attend the Siegmann International school on lasers, organized by Technical University of Denmark at Spirit of Hven Backfallsbyn, Sweden, July 28 – August 4 , 2018.
4. Received departmental best poster for the paper entitled “Liquid Crystal Spatial Light Modulator Based wavefront sensing and its Application", in Research Conclave 2017.

* * *